

Dissertation
submitted to the
Combined Faculties for the Natural Sciences and for Mathematics
of the Ruperto-Carola University of Heidelberg, Germany
for the degree of
Doctor of Natural Sciences

Put forward by

Diplom-Phys.: **Kerstin Geißler**
Born in: **Freiberg (Sachs.)**
Oral examination: **May, 6. 2009**

The environment of near-by stars: low-mass companions and discs

Referee:

**Prof. Dr. Thomas Henning
Dr. Coryn Bailer-Jones**

Zusammenfassung: Um die Genauigkeit theoretischer Modellen zu überprüfen, wurden vier Braune Zwerge, Mitglieder von Mehrsternsystemen, mit VISIR in drei Schmalbandfiltern im mittlerem Infrarotem beobachtet. Beim Vergleich der gemessenen mit den theoretischen berechneten Flüsse offenbarte sich eine gute Übereinstimmung zwischen beiden. Nur im Falle von HD 130948BC waren Unstimmigkeiten zwischen zwei Messungen bei $11.5\ \mu\text{m}$ auffällig, welche darauf hindeuteten, dass das Objekt variable sein könnte. Die darauf durchgeführten Nachfolgebeobachtungen zeigten aber, dass HD 130948BC nicht variable ist.

Abgesehen davon bietet das mittlere Infrarote auch die Möglichkeit nach massearmen Begleiter (Braunen Zwergen und Planeten) im Orbit um helle, nahe Sterne zu suchen. Der günstigere Kontrast zwischen Hauptstern und Begleiter und das verbesserte Verhalten der Punktverbreiterungsfunktion bei längeren Wellenlängen, eröffnen die Möglichkeit Begleiter in Entfernungen von nur $1''$ bis $3''$ zu entdecken. Darum haben wir ein Sample von dreizehn Sternen mit den Instrumenten T-ReCS und VISIR beobachtet, wobei Sensitivitäten von bis zu $3\ \text{mJy}$ im Abstand von $2''$ erreicht worden.

Unter Verwendung des polarimetrischen Beobachtungsmodus von VLT/NACO wurden zwölf Sterne mit nah-infrarot Excess beobachtet. Der Beobachtungsmodus ermöglicht das von der Scheibe reflektierte und polarisiert Licht auch in der näheren Umgebung des Sterns zu entdecken. Im Zuge dieser Arbeit wurden die polarisierten Intensitätsverteilungen und die Polarisationsmuster der Beobachtungsobjekte untersucht und charakterisiert.

Abstract: In order to compare the mid-ir flux of brown dwarfs (BD's) to the predictions of current atmospheric models, we observed four BD's in multiple systems with the VLT/VISIR in three narrow band filters. In general the measurements were in good agreement with the predictions. Only for HD 130948BC discrepancies between two observations at $11.5\ \mu\text{m}$ are notable, suggesting that the object might be variable. Thus we re-observed the BD, monitoring it over three half nights, proving that the object is not variable.

But the mid-infrared also offers possibilities to search for brown dwarf or planetary companions to near-by, bright stars. The favourable flux contrast and the overall better PSF shape at longer wavelengths, enables us to detect companions at separations of only $1''$ to $3''$. Thus for thirteen stars we conducted observations with T-ReCS and VISIR, reaching sensitivities of $3\ \text{mJy}$ ($3\ \sigma$) at $2''$.

Using the polarimetric differential imaging (PDI) mode of VLT/NACO we observed twelve near-infrared excess stars. Thereby the PDI technique allows us to trace the scattered (i.e. polarised) light from the circumstellar disc very close to the central star. Here we analyse the polarised intensity distribution and characterise the polarised vector pattern, exhibited by the targets.

Contents

1	Introduction	1
1.1	Basics on Brown Dwarfs	1
1.2	Circumstellar Discs	3
1.3	The Mid-Infrared Wavelength Regime	5
2	Mid-Infrared Imaging of Brown Dwarfs	7
2.1	Brown Dwarfs in the Mid-Infrared	7
2.1.1	L- and M- Band Observations	7
2.1.2	Results from the Spitzer Space Telescope	8
2.2	Mid-Infrared Imaging of Brown Dwarfs in Binary Systems	10
2.2.1	The case of ϵ Indi B	10
2.2.2	Target Properties and Observations	12
2.2.3	Data Reduction	14
2.2.3.1	Aperture Photometry	14
2.2.3.2	Detection Limits	16
2.2.4	Results	17
2.2.5	Discussion	18
2.2.5.1	Comparison with Models	18
2.2.5.2	HD 130948 BC: Photometric Variability	21
2.3	Follow-up Observations of HD 130948	22
2.3.1	Observation	22
2.3.2	Data reduction and background filtering	22
2.3.3	Simulations	23
2.3.4	Results	24
2.4	Conclusion	29
3	Searching for Low-Mass Companions in the Mid-Infrared	31
3.1	Motivation	31
3.1.1	Previous Work	31
3.1.2	Limits	32
3.2	Survey	34
3.2.1	Target Sample	34
3.2.2	Observations and Data Reduction	36
3.2.3	Analysis and Results	39
3.3	Conclusion	43

4	Polarimetric Differential Imaging of Circumstellar Discs	45
4.1	Principles of Polarimetric Differential Imaging	45
4.1.1	Polarimetric Differential Imaging	45
4.1.2	Differential Polarimetry with NACO	46
4.2	Project Description	48
4.2.1	Target sample	48
4.2.2	Observations and Reduction	53
4.2.3	Results	56
4.2.4	Individual targets	56
4.2.4.1	Compact objects	56
4.2.4.2	HD 100546	61
4.2.4.3	WLY 2-44	61
4.2.4.4	Elias 2-21	66
4.2.5	Discussion	72
4.3	Conclusion	74
5	Summary and Outlook	75
A	VISIR 'Burst' Mode Detection Limits	77
	Bibliography	89

Chapter 1

Introduction

The existence of substellar mass, star-like objects was first considered by Kumar (1963), describing their essential properties as : no central energy source due to hydrogen fusion, degeneracy and a short luminous lifetime. The first secured discovery's of brown dwarfs - renamed by Tarter & Silk (1974) - were done in the mid 90's (Nakajima et al. (1995), Delfosse et al. (1997)). By today, hundreds of brown dwarfs have been discovered in the field, in young star forming regions, as members of brown dwarf binaries and multiple stellar systems. While the former allow to study the space density and thus the initial mass function (IMF), the relative frequency and the mass-ratio distribution of the later are important to the understanding of binary star formation.

To distinguish brown dwarfs from planets the IAU established a definition, which separates the two classes based on there mass. Objects orbiting stars or stellar remnants with masses less than $13 M_J$ are by definition planets. In principle, a more physical discrimination is based on the mode of formation. Thereby, planets form in a disc around a more massive central objects, while brown dwarfs form as separate, accreting entities, like stars.

Evidence that brown dwarfs share a common formation history with stars comes from the observations of circumstellar discs, accretion and outflows. Brown dwarfs in young star forming regions have been found to harbour circumstellar discs, as indicated by near- and mid-infrared excess fluxes (Muench et al. (2001), Luhman et al. (2005b)). Circumstellar discs have been discovered around brown dwarfs of masses down to the planetary limit (Luhman et al., 2005a). Moreover, there is a large fraction of young brown dwarfs showing the typical emission line spectrum of T Tauri stars (Jayawardhana et al. (2003), Mohanty et al. (2005)). The broad, asymmetric H lines and additional emission lines, like HeI and OI are direct evidence for ongoing accretion in the objects. Finally, outflows from substellar objects have been detected through the emission in the forbidden [SII] and [OI] lines (Barrado y Navascués et al. (2004), Whelan et al. (2005)).

1.1 Basics on Brown Dwarfs

Brown dwarfs (BD's) bridge the gap in mass between low-mass stars and giant planets. Hundreds of them have been discovered in the past decade, mainly in wide-field optical (SDSS, Stoughton et al. (2002)) and near-infrared (e.g., 2MASS - Cutri et al. (2003), DENIS - Epchtein et al. (1997)) surveys. Two main classes of BD's emerged based on their optical and infrared spectral properties, the L-dwarfs (Martin et al. (1997), Kirkpatrick et al. (1999))

and the T-dwarfs (Burgasser et al., 1999). These two new spectral classes can be seen as a natural continuation of the classical spectral type sequence. The L dwarfs cover the effective temperature range from 2200K to 1300K, and their spectra are labelled by the weakening of TiO and VO absorption, which characterise the optical spectra of the M dwarf, as well as by the growing strength of the neutral alkali-metal lines. The on-set of CH₄ absorption in the near-infrared marks the beginning of the T dwarfs, which cover even cooler effective temperatures between 1200K and 750 K. The modeling of atmospheres cooler than $T_{eff} \leq 2000$ K is a challenge, because it must include an appropriate treatment of a plethora of molecular opacity's and dust processes (formation, condensation, size distribution and mixing). The most recent atmosphere models include additional properties such as age (gravity) and metallicity, and seem to reproduce the spectral signatures and the infrared colours of L and T dwarfs reasonably well. Only the L-T transition, occurring around a relatively narrow temperature range of T_{eff} 1300–1400 K, remains problematic (for a discussion of state-of-the-art models see Burrows et al. (2006)).

Theoretical models : The atmospheres of low-mass stars and brown dwarfs are shaped by broad absorption bands. Below 5000 K numerous molecules start to form, among them are metal oxides and hydrides, like TiO, VO, FeH, CaH and MgH, which are the major absorbers in the optical, and carbon monoxide (CO) and water (H₂O), which dominate the infrared. Below 2500 K the situation gets even more complex, since there is evidence for the condensation of metals and silicates into grains (see Chabrier et al. (2005) and references therein). Below 2000 K the dominant form of carbon is carbon monoxide (CO) while the remaining oxide is locked in titanium (TiO) and vanadium monoxides (VO) and water vapour (H₂O). Below 1800 K methane (CH₄) instead of CO is the dominant form of carbon. Theoretical modelling of the atmospheres has to account for these transitions and the effects of the different molecules and grains. Especially, since the condensates or grains affect the atmosphere in different ways. The grain formation depletes the gas-phase in certain regions of the atmosphere and modifies the atmospheric temperature profile, the opacities and thus the emergent spectrum.

So far the theoretical models by the Lyon group have been treating the grain formation process in two extreme regimes. There so-called “dusty” models (Allard et al., 2001) represent the case between $1700 < T < 2500$ K, thus they are applicable to late M- to mid-L- type dwarfs. Here all condensed species are included in the atmosphere and in the radiative transfer model, but dust settling is negligible. At temperatures below 1700K the other case, the “condensed” models, apply (Baraffe et al., 2003). Here all grains either have formed or have sunk below the photosphere. The “cond” models reliably reproduce the spectral energy distribution and the photometry of T dwarfs. Only objects falling into the transition region (L/T transition) can not be reproduced by the two case models. The transition from one to the other model would require to take dynamical processes into account. Existing models include, e.g., cloud segmentation, but still give only a qualitative description of the L-T transition.

However, the final test of all models is the comparison to observation. Best suited for this purpose are binary brown dwarfs or brown dwarfs in multiple systems, since basic properties, like age and metallicity, are more easily inferred from binary brown dwarf systems (Liu & Leggett, 2005) or from the primaries of multiple systems (Leggett et al., 2002b). But from the 700¹ known L and T dwarfs, only about 40 are L or T binary dwarf systems, about 20

¹Dwarf Archive: <http://spider.ipac.caltech.edu/staff/davy/ARCHIVE/index.shtml>

form binaries with late M dwarfs and about 28 are companions to higher mass stars, like Gliese 229 the first unambiguously discovered brown dwarf (Nakajima et al., 1995).

1.2 Circumstellar Discs

In order to study the evolution of circumstellar discs, sun-like stars at a variety of ages have to be observed, assuming that the younger stars represent the evolutionary predecessor of the older. A general classification scheme for the evolutionary sequence of young stellar objects was first defined by Lada (1987) and later extended by Andre et al. (1993). There are supposed to be four phases of stellar evolution:

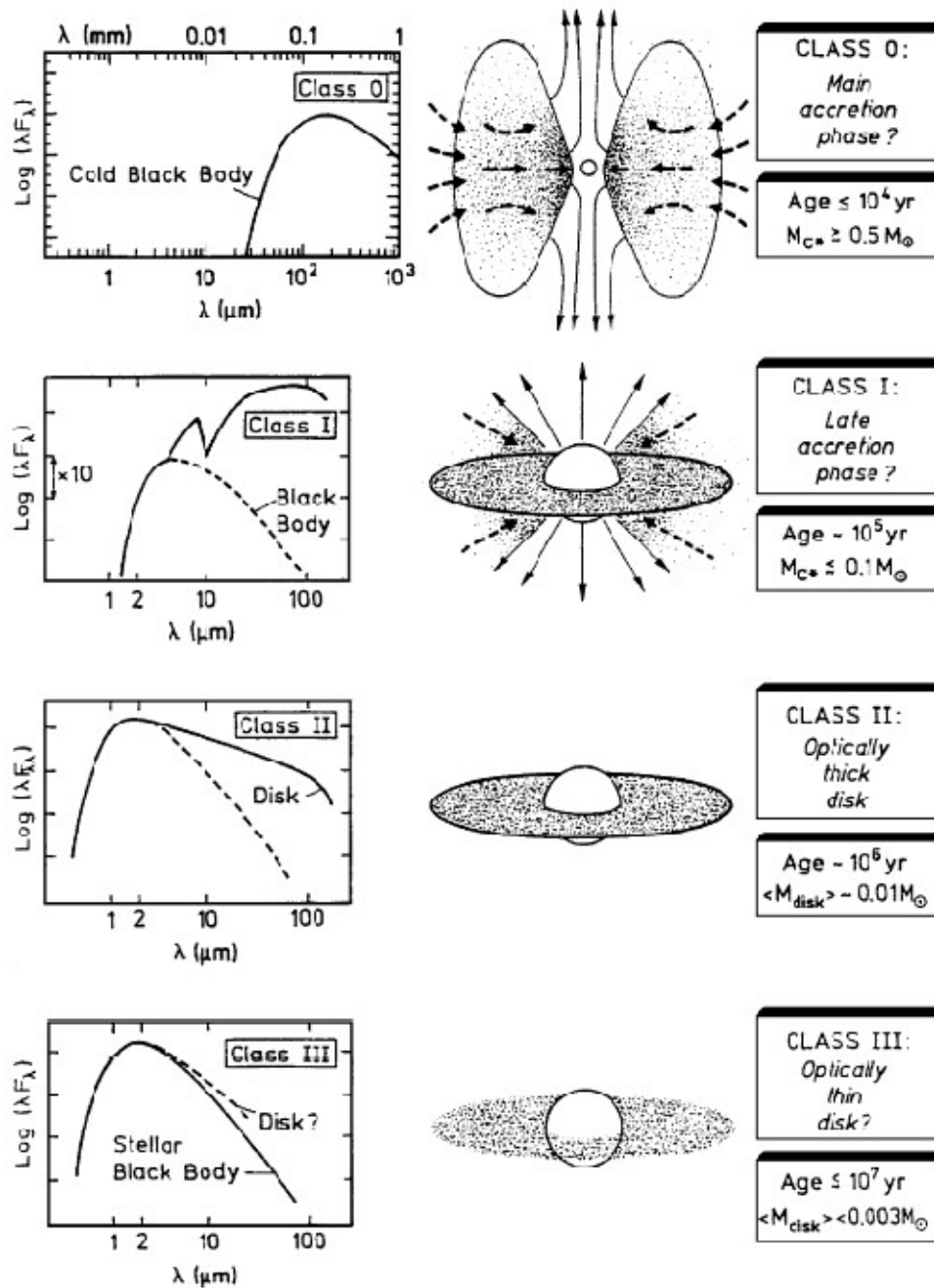
- Class 0 (protostellar core) : This is the earliest observable phase of star formation and is visible only due to continuum radiation around 1mm and the CO spectral lines. The dust shell is so thick that the central source is not visible in mid-infrared. During this phase there is supposed to be strong gas and dust accretion ongoing.
- Class I (evolved protostar) : During this phase the accretion continues accompanied by collimated outflows. The protostar is surrounded by an optically thick accretion disc and thus not visible, but molecular outflows, jets and dust emission can be observed.
- Class II ('classical' T Tauri star, young Herbig Ae/Be star): The accretion is still ongoing, but the shell which surrounded the protostar disappears and the central star becomes visible. The circumstellar environments of T Tauri and Herbig Ae/Be stars are generally thought to represent an early stage of planet formation.
- Class III (debris disc): In this last stage only a thin accretion disc remains. The Spectral Energy Distribution (SED) approaches that of 'normal' stars. The remaining/existing dust is mostly second generation dust, i.e. it is caused by collisions of planetesimals.

Since the temperature of the disc decreases with the distance from the central star, different regions of the disc can be probed by different wavelengths. Near-infrared excesses emission traces the presence of an inner disc ($r < 0.05$ - 0.1 AU), which appears to correlate with spectroscopic signatures of accretion (Hartigan et al., 1995). Studies of near-by star forming regions (e.g., Strom et al. (1989) show that 60-80% of the stars younger than 1 Myr have measurable near-infrared excesses, while $\leq 10\%$ of the stars older than 10 Myr do so. The inferred disc fractions are consistent with mean disc lifetimes on the order of 2-3 Myr and a wide dispersion.

The region of the disc from $r \sim 0.05$ AU to 20 AU, the planet-forming regions, can be studied in the mid-infrared wavelength regime. Observations with the Spitzer Space Telescope show that pre-main sequence stars lacking near-IR excess are also very likely to have no measurable $24\mu\text{m}$ excesses (e.g., Padgett et al. (2006), Silverstone et al. (2006), Cieza et al. (2007)). Optically thick primordial disks appear to be non-existent beyond an age of 10 Myr.

Finally the outer disc ($r \sim 50$ - 100 AU) can be observed in the sub-mm. Just as for the planet-forming region of the disc, recent sub-millimeter results indicate that the disc lifetimes of inner and outer disc coincide. Andrews & Williams (2005) find that less than 10% of the objects lacking inner disk signatures are detected at sub-mm wavelengths. Based on

Figure 1.1: Empirical evolutionary sequence of young stellar objects (YSOs) according to Andre & Montmerle (1994). The ages correspond to a solar like star.



the mass sensitivity of their survey, they conclude that the dust in the inner and the outer disk dissipates nearly simultaneously.

From spatially unresolved observation disc temperatures and density profiles can be inferred, but they rely on spectral energy distributions (SEDs) and assumptions about the disc morphology. High angular resolution measurements of the dust and gas content and distribution within the discs are vital to quantify the profiles and understand the unresolved observations. Spatially and kinematically resolved images may provide measurements of the stellar mass, the disc mass, the disc radius, the inclination of the disc and the substructure within (e.g., Greaves et al. (1998), Krist et al. (2000), Kalas et al. (2004)) Today, about 113^2 circumstellar discs have been resolved, the majority being pre-main sequence discs. Only a few resolved debris disc are known, which often show smooth azimuthal distributions, frequently distributed in ring-like geometries (e.g., Schneider et al. (1999), Kalas et al. (2004), Schneider et al. (2006)).

1.3 The Mid-Infrared Wavelength Regime

Conventionally the infrared wavelength regime is divided in three regions. The near-ir ranging from $0.75 - 5 \mu\text{m}$, the mid-ir from $5 - 25 \mu\text{m}$ and the far-ir from $25 - 350 \mu\text{m}$. Here we will only concentrate on the mid-ir, which provides valuable information about warm dust and gas. Micron sized particles such as silicates, silicon carbide, carbon, coals, aluminum oxides or polycyclic aromatic hydrocarbon (PAH) molecules are major contributors to the thermal dust emission, while the gas emits through a large number of ionic and atomic lines. However, the earth atmosphere absorbs the biggest part of the mid-ir radiation coming from space. The main absorbing molecules are H_2O , CH_4 , CO_2 , CO , O_2 , O_3 . Only in two atmospheric windows, the N- and Q-band, centered around $10.$ and $20. \mu\text{m}$, respectively, the atmosphere is transparent. Nevertheless the transmission is rapidly decreasing with wavelength and specially observations in the Q-band require low water vapor content in the atmosphere. Space based mid-ir instruments do not suffer from these limitations, providing higher sensitivities than ground based instruments can do. However, ground based instruments mounted on large telescopes, such like the VLT or GEMINI, offer superior spatial resolution. For example VISIR at the VLT provides diffraction limited images at $0.3''$ (FWHM) in the N- band. This is an order of magnitude better than what can be reached by the *Spitzer Space Telescope*. Nevertheless, to deal with the bright and rapidly varying background, caused by the ambient atmosphere and the telescope, a special technique, the so-called chopping and nodding, is applied.

Chopping: The technique of chopping refers to a slight movement of the secondary mirror. After a set of on-source exposures a near-by position on the sky, the so-called off-source exposure, is observed frequently by moving the secondary mirror at a frequency of a few Hz. The chopping frequency must be high enough to assure that the on- and off-source observations are alternated at a rate faster than the background fluctuates to achieve a good background cancellation when subtracting the pairs of images. However, by moving the secondary mirror the optical path is slightly changed, so that the telescope is seen differently

²Resolved circumstellar discs : <http://www.circumstellardisks.org/>

by the detector for the two mirror positions. Therefore a residual background remains. It is much less than the telescope and sky brightnesses and varies at a time-scale which is long compared to that of the sky. This residual background is then suppressed by nodding.

Nodding: In this second step the entire telescope is moved to an offset position about twice a minute. At the off-source nodding position the chopping pattern is repeated. Normally the nod is set to be the same amplitude as the chop, but the direction of the nod can either be parallel or perpendicular to the chopping direction. So depending on the chopping and nodding amplitude and direction up to four images can be seen on the detector.

Mid-IR Instruments: In the following two mid-infrared instruments, which have been employed in the course of this work, shall be described in more detail. One is VISIR mounted at the third Unit Telescope (UT3, Melipal) of the Very Large Telescope (VLT) on Cerro Paranal in Chile. The second being T-ReCS at the GEMINI South on Cerro Pachon in Chile, too.

VISIR: The VLT spectrometer and imager for the mid-infrared (VISIR³, Lagage et al. (2004)) provides diffraction limited imaging and spectroscopy in the wavelength range from 8 to 24.5 μm . The VISIR imager and spectrometer are each equipped with a 256×256 pixel detector and for imaging two plate scales are available (0.075" and 0.127"). A large number of narrow band filters covering the whole N- and Q-band are available and spectroscopy can be carried out with spectral resolutions between 150 and 30000.

The spatial resolution of an instrument is ultimately limited either by the diffraction of the telescope or the atmospheric seeing. For VISIR the data is already diffraction limited for optical seeing below 0.6". The second limiting factor for observations in the mid-ir is the background emission. The VLT telescope emits at 283 K, but to avoid internal background contamination the instrument is cooled. The detectors are at 5–6 K and the interior of the cryostat at 33 K. Still the number of photons reaching the detector is huge. Therefore, the exposure time of an individual integration - the Detector Integration Time (DIT) - has to be short, of the order of a few tens of milli-seconds in imaging mode.

T-ReCS: The Thermal-Region Camera Spectrograph (T-ReCS, Roche (2004)) is a mid-infrared imager and long-slit spectrograph built by the University of Florida for Gemini South. The instrument is capable of imaging and spectroscopy in the 8–26 μm range. Broad band N and Q as well as narrow band filters are available for imaging, while spectroscopy can be done with a spectral resolution of around 100 to 1000. For T-ReCS the plate scale is fixed resulting in a pixel size of 0.09" and hence a Field of View (FoV) of 28.8" \times 21.6".

³VISIR homepage <http://www.eso.org/instruments/visir/>

Chapter 2

Mid-Infrared Imaging of Brown Dwarfs

2.1 Brown Dwarfs in the Mid-Infrared

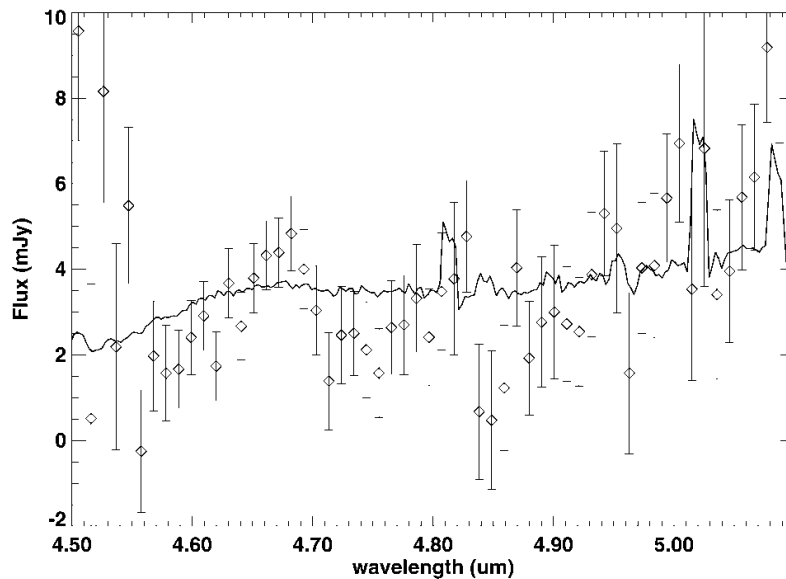
At mid-infrared wavelengths the spectra of very low mass stars and brown dwarfs are much easier to interpret than in the optical or near-infrared. While in the near-infrared the absorption bands of H₂O, CO, CH₄ and NH₃ are mainly overtone and combination bands, in the mid-infrared they arise from fundamental transitions, for which nearly complete line lists exist. Thus the effects of non-equilibrium chemistry on the abundances of CO, CH₄, N₂ and NH₃ and hence on the band strengths of the molecules, which are strongest at mid-infrared wavelengths (Saumon et al. (2003a), Saumon et al. (2003b)) can be studied. Furthermore if populations of small iron and/or silicate particles are present in the atmospheres of very low-mass objects, silicate absorption features may appear near 10 μm .

2.1.1 L- and M- Band Observations

Until the launch of the *Spitzer Space Telescope* observations of brown dwarfs in the infrared were merely confined to the near-ir. Only one brown dwarf, namely DENISPJ0255-4700, had been imaged in the mid-ir using OSCIR at the GEMINI South (Creech-Eakman et al. (2004)). The observations of the L6 dwarf were carried out in the broad N-band filter and in three narrow band filters at 8.8, 10.3 and 11.7 μm , suggesting some discrepancies between the state of the art theoretical models and the observations.

Even the number of observations in the near-infrared bands at 3.8 μm (L) and 4.8 μm (M) is limited. The majority of those are photometric observations (Leggett et al. (2002a) , Golimowski et al. (2004)), which are used to account for the flux emitted at longer wavelength's when calculating bolometric luminosities. The bolometric luminosities are then combined with a theoretical radius to determine effective temperatures for the brown dwarfs. Only a few brown dwarfs have been observed spectroscopically in either L or M band. The L band contains the ν_3 fundamental absorption band of CH₄ at $\sim 3.3 \mu\text{m}$, which has been detected in spectra of mid L- too T-type dwarfs (Oppenheimer et al. (1998), Noll et al. (2000), Cushing et al. (2005)). Furthermore, the fundamental CO absorption band at 4.7 μm has been detected in the M band spectra of the T7p-type dwarf GL229 B as shown in Figure 2.1.1 (Noll et al. (1997), Oppenheimer et al. (1998)).

Figure 2.1: Diamonds and estimated error bars show the spectrum of Gl 229B, which is a co-add of four nights of observations. A scaled spectrum of Gl 229A is shown by the solid curve. The peak in the spectrum at $4.67\ \mu\text{m}$ occurs at the center of the CO 1–0 vibration rotation band in between the P- and R-branches of this diatomic molecule. CO also occurs in Gl 229A (spectral type M1 V), but the P- and R-branches are less prominent because of the higher temperature.



Surprisingly, the CO absorption band was found to be about 1000 times stronger than expected, suggesting that equilibrium CH_4/CO chemistry underestimates the abundance of CO and may not be applicable to the atmospheres of these cool objects.

2.1.2 Results from the Spitzer Space Telescope

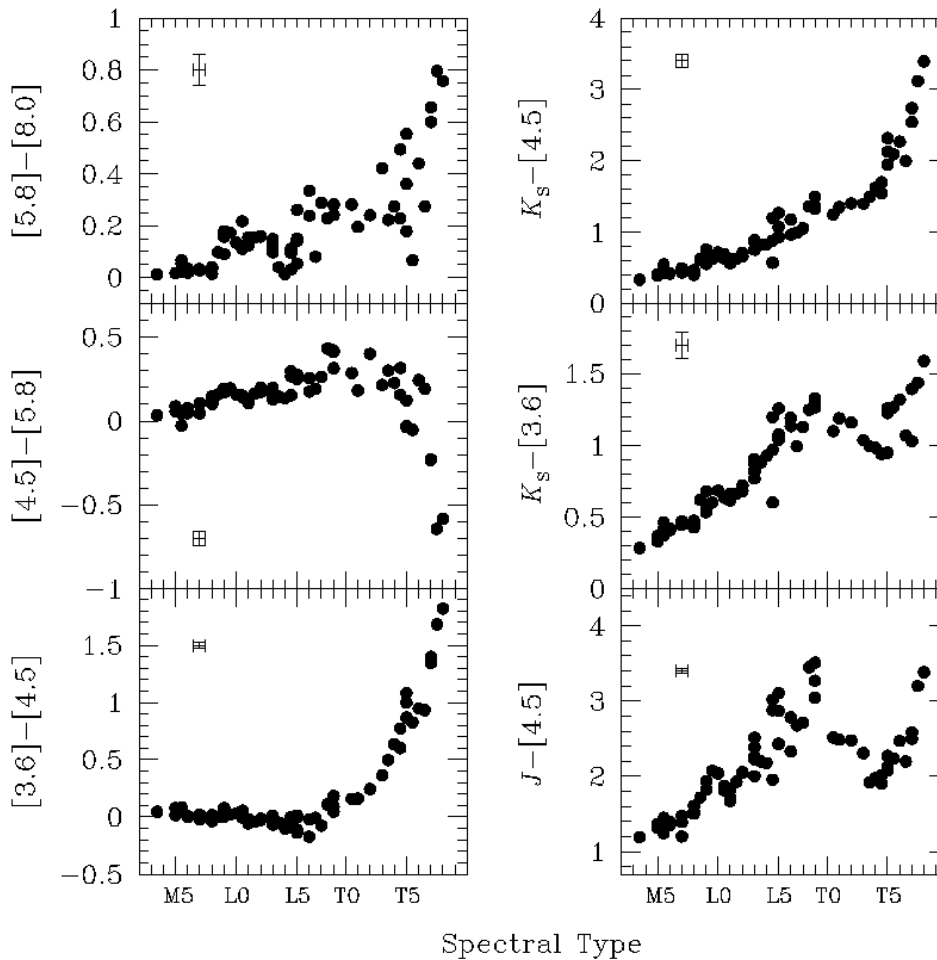
With the launch of the *Spitzer Space Telescope* (Werner et al. (2004)) in August 2003 a new area of mid-infrared observations began. With a diameter of 85 centimeters of the primary mirror, Spitzer is about a factor of 1.5 bigger than its predecessor IRAS. The Spitzer Space Telescope is equipped with three instruments operating in the wavelength range from about $3.3\ \mu\text{m}$ to $160\ \mu\text{m}$.

- The IRAC instrument is a four-channel camera providing simultaneous images at 3.6 , 4.5 , 5.8 , and $8\ \mu\text{m}$ (Fazio et al. (2004)). Two adjacent fields of view are imaged in pairs using dichroic beamsplitters.
- The MIPS photometer provides capabilities for imaging and photometry in broad spectral bands centered nominally at $24.$, $70.$, and $160.\ \mu\text{m}$, and for low-resolution spectroscopy between $55.$ and $95.\ \mu\text{m}$ (Rieke et al. (2004)).

- IRS is a spectrograph providing low and moderate resolution spectroscopic capabilities from 5.2 to $38.0\ \mu\text{m}$ (Roellig et al. (1998)). The instrument is composed of four separate modules, with two modules providing $R \sim 60$ - 120 spectral resolution over 5.2 - $38.0\ \mu\text{m}$ and two modules providing $R \sim 600$ spectral resolution over 9.9 - $37.2\ \mu\text{m}$.

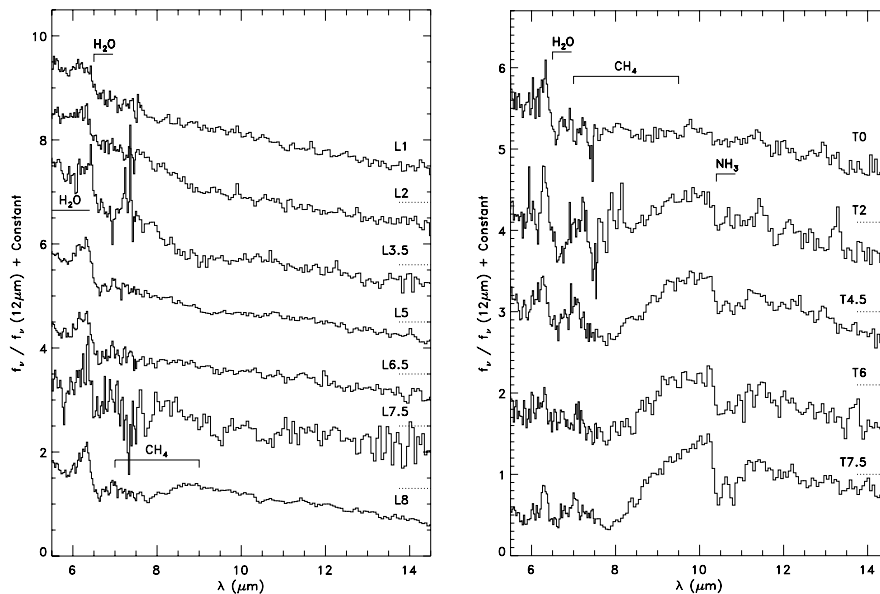
Using the Spitzer Space Telescope two big surveys have been executed to study the mid-infrared properties of very low mass stars and brown dwarf. The first being a survey of 86 M-, L- and T-type low-mass stars and dwarfs using IRAC (Patten et al. (2006)). Observations were conducted in all four band passes to establish color-color, and color-flux relations for the first time in the mid-infrared and in combination with the near-infrared (see Figure 2.2). Patten et al. (2006) reported that the flux observed in the IRAC $4.5\ \mu\text{m}$ band is lower than expected, probably due to the fact that the CO fundamental absorption band at $\sim 4.67\ \mu\text{m}$ is stronger than expected, as already has been seen in the M-band spectra of GL229 B (Noll et al. (1997), Oppenheimer et al. (1998)).

Figure 2.2: Taken from Patten et al. (2006). Shown is a summary of the various trends seen in the colour versus spectral type relations.



The second program made use of the IRS instrument to obtain low-resolution spectroscopy ($R \equiv \lambda/\Delta\lambda \simeq 90$) for a sample of brown dwarfs covering the spectral sequence from the latest M- to the latest T-type dwarfs (Cushing et al. (2006)). The spectra cover a range from 5.5 - 38. μm and show prominent absorption bands of H_2O at 6.27 μm , CH_4 at 7.65 μm and NH_3 at 10.5 μm , which were first identified by Roellig et al. (2004), but are featureless at wavelengths $\gtrsim 15 \mu\text{m}$. The H_2O absorption is existing through out the whole spectral sequence, while the CH_4 and NH_3 absorption bands first appear around the L/T transition.

Figure 2.3: Presented are the 5.5 - 14.5 μm spectra of L and T dwarfs taken by the IRS instrument (Cushing et al. (2006)).



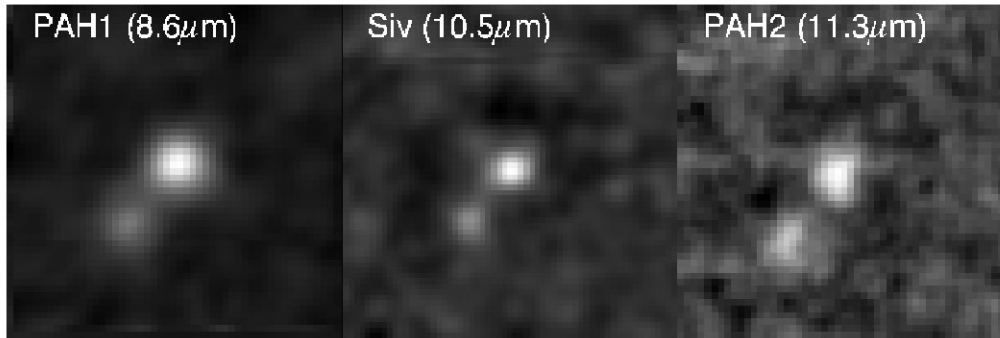
2.2 Mid-Infrared Imaging of Brown Dwarfs in Binary Systems

2.2.1 The case of ϵ Indi B

The power of sensitive, ground-based, high spatial resolution, mid-infrared imaging has recently been demonstrated for the close BD binary companion Indi Ba and Bb (see Sterzik et al. (2005)). The relative photometry between both components allowed them to derive effective temperatures independently from the determinations in near-infrared. As the distance is well known for the primary, the absolute photometry constrains radii and bolometric corrections, in contrast to Spitzer observations (Roellig et al. (2004)) that suffered from insufficient angular resolution to resolve both components (Spitzer diffraction limit at 10 μm is 3 arcsec).

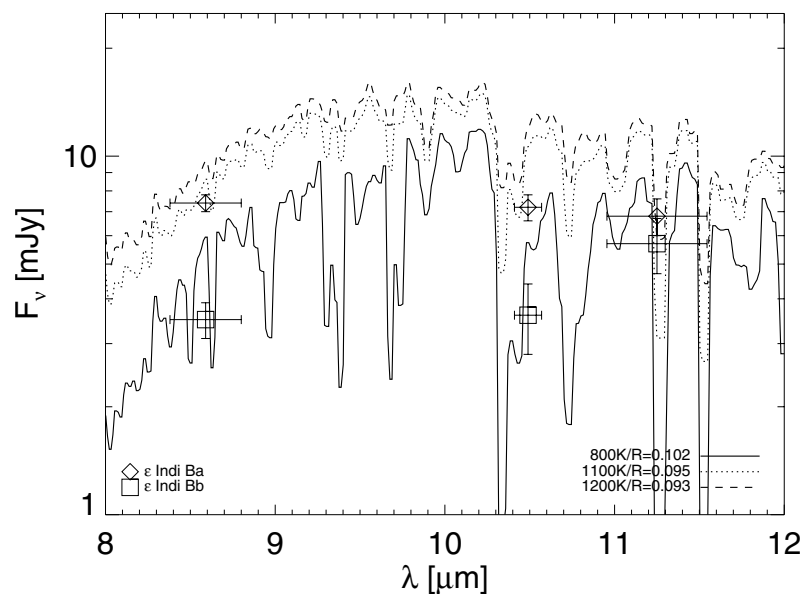
Using VISIR at the VLT Sterzik et al. (2005) did observe the binary in three narrow band filters at 8.6, 10.5 and 11.25 μm (see Figure 2.4). Both components were resolved during the observations and fluxes measured for both of them. In the following the measured fluxes

Figure 2.4: VLT/VISIR detection images of the binary brown dwarf ϵ Ind BaBb as published by Sterzik et al. (2005).



were compared to fluxes calculated from existing theoretical models. The fainter, less massive component (Bb) agreed well with “cloud-free” atmosphere models assuming an effective temperature of $T_{eff} = 800$ K. For the brighter, more massive component (Ba) existing determinations of the effective temperature yield values between $T_{eff} = 1200$ K (Roellig et al. (2004)) and $T_{eff} = 1500$ K (Smith et al., 2003). Theoretical models with this configurations however return too high fluxes, or if consistent with the measured fluxes would imply an unphysical small radius for the brown dwarf. The authors argue that the brown dwarf has a lower temperature of only about 1100K, for which the theoretical fluxes are in agreement with the measured values (see Figure 2.5).

Figure 2.5: VLT/VISIR photometry of the binary brown dwarf compared to selected theoretical models (Sterzik et al. (2005)).



In order to continue the effort to constrain atmospheric and evolutionary models of BDs, we have therefore conceived a mini-survey of close BD companions using the mid-infrared imager VISIR at the VLT. Section 2.2.2 reviews the target's properties and describes our observations. Section 2.2.3 describes the data reduction and analysis process. Section 2.2.4 presents the results of our survey, i.e. the photometry and the astrometry of the detected companions and the sensitivity limits obtained. Finally, Section 2.2.5 compares our results with the predictions of cool atmosphere models, to discuss their applicability and limitations.

2.2.2 Target Properties and Observations

For our target selection, we only considered the confirmed members of binary (or multiple) systems with known distances, as their primaries are well characterized in terms of metallicity and age. Only BD companions with expected mid-IR fluxes stronger than 1mJy and separations larger than 0.5 arcsec were selected, in order to fully adapt and exploit the sensitivity and spatial resolution of the mid-infrared imager VISIR at the VLT. We finished with a short list of four systems: GJ 229, HD 130948, HR 7329 and HR 7672. Their main characteristics are summarized in Table 2.1.

- GJ 229 B is the first unambiguous BD discovered (Nakajima et al. (1995)). Later on, orbital motion was detected by Golimowski et al. (1998), who observed GJ 229 B at three epochs spread over approximately one year using HST's Wide Field Planetary Camera 2 (WFPC2). Matthews et al. (1996) derived an effective temperature of 900 K from the measured broadband spectrum of GJ 229 B, assuming a radius equal to that of Jupiter. The same effective temperature was obtained by Leggett et al. (1999) by comparing colours and luminosity to evolutionary models developed by Burrows et al. (1997). In general model spectra for GJ 229 B (Marley et al. (1996); Allard et al. (1996)) reproduce the overall energy distribution fairly well and agree with $T_{eff} = 950$ K.
- HD 130948 BC is a binary brown dwarf companion detected by Potter et al. (2002). The separation between the two companions is (0.134 ± 0.005) arcsec at $PA = (317 \pm 1)^\circ$. Both companions have the same spectral type $(L4 \pm 1)$ and effective temperatures ($T_{eff} = (1900 \pm 75)$ K, Goto et al. (2002)).
- HR 7329 B is a BD companion detected by Lowrance et al. (2000) at a separation of 4'' from the early-type star HR 7329 A, a member of the β Pictoris moving group (Zuckerman et al. (2001)). Its optical spectrum points towards a spectral type M7/M8 and an effective temperature of 2405 to 2770 K for this young substellar companion. Guenther et al. (2001) presented evidence that the source is a co-moving companion.
- HR 7672 B, a common proper motion companion to the variable star HR 7672 A, was reported by Liu et al. (2002). They inferred an effective temperature of $T_{eff} = 1510 - 1850$ K for HR 7672 B and estimated an age of 1–3 Gyr for the system.

All targets were observed using VISIR mounted at the UT3 (Melipal) with the filters PAH1 ($\lambda_{cen} = 8.59 \mu\text{m}$, $\Delta\lambda = 0.42 \mu\text{m}$), PAH2 ($\lambda_{cen} = 11.25 \mu\text{m}$, $\Delta\lambda = 0.59 \mu\text{m}$) and SIV ($\lambda_{cen} = 10.49 \mu\text{m}$, $\Delta\lambda = 0.16 \mu\text{m}$). A nominal pixel scale of 0.075'' was used during all observations, and standard chopping and nodding techniques were employed, with a chop-throw amplitude of 6'' and 8'' for GJ 229, and a chopping frequency of 0.25 Hz. The nodding direction was chosen

Table 2.1: Target properties

Object	π [mas]	Age [Gyr]	[M/H]	separ. [arcsec]	P.A. [$^{\circ}$]	Spectral type B	T_{eff} [K]	log g
GJ229 (1)	173.19	0.2 (1) 0.03 (2)	-0.5--0.1 (4) -0.5 (2)	7.761 \pm 0.007 (3)	163.5 \pm 0.1	T7p	950 \pm 80 (4) 1000 \pm 100 (2)	5 \pm 0.5 (4) \leq 3.5 (2)
HD 130948 (5)	55.73	0.3-0.8 (6-8)	0.0 (10)	2.64 \pm 0.01 (5)	104.5 \pm 0.5	L4 \pm 1*	1900 \pm 75 (9)	
HR 7329	20.98	0.012 (12)		4.17 \pm 0.05	166.8 \pm 0.2	M7/M8	2600 \pm 200 (11)	
HR 7672	56.60	1-3 (13)	0.02 (10)	0.794 \pm 0.005 (13)	157.3 \pm 0.6	L4.5 \pm 1.5 (13)	1680 \pm 170 (13)	

*binary brown dwarf
Reference: 1.) Nakajima et al. (1995); 2.) Leggett et al. (2002b); 3.) Golimowski et al. (1998); 4.) Saumon et al. (2000); 5.) Potter et al. (2002); 6.) Gaidos (1998); 7.) Gaidos et al. (2000); 8.) Fuhrmann (2004); 9.) Goto et al. (2002); 10.) Valenti & Fischer (2005); 11.) Lowrance et al. (2000); 12.) Zuckerman et al. (2001); 13.) Liu et al. (2002)

parallel to the chopping direction and, consequently, with an equal nodding to chopping amplitude.

To ensure that the primary and the companion are within the FoV during chopping and nodding, the system was aligned horizontally on the detector. At the same time, this simplifies the reduction process, since the shifting and adding of the frames can be done using the brighter primary star. A summary of the observing log is given in Table 2.2, including the mean airmass during the observing run and the total integration time.

2.2.3 Data Reduction

The reduction was done using self-written IDL routines for bad-pixel replacement and for the shifting and adding of the frames. Bad-pixels were replaced by the mean value of the surrounding pixels within a box of 9×9 pixel, before subtracting (A-B) nodding positions. In the following, the relative shifts between the frames of one data-set were calculated via cross-correlation of the bright primary, before the frames were averaged. Since the VISIR detector was affected by randomly triggered stripes during part of the observations, a destriping technique developed by Pantin et al. (2007) was applied to the final co-added images.

2.2.3.1 Aperture Photometry

Standard aperture photometry was used to determine the relative photometry of all detected BDs. Using IDL ATV routines, a curve-of-growth method was applied to the brown dwarf companions to obtain the apertures where the signal-to-noise ratio is maximised. In the following, those apertures were used for the primary as well as for the standard stars. Thus the count-rate to flux conversion factor was determined and relative photometry obtained. The variation of the count-rate to flux conversion factors with aperture radius was screened for at least 3 consecutive aperture radii between 4 and 7 pixels (corresponding to radii of $0.3''$ to $0.525''$). At $10 \mu\text{m}$ the VISIR diffraction limit is $0.3''$, the chosen aperture radii are of the order or twice the diffraction limit. To calibrate the flux values different standard stars¹, observed before and after the targets, were used. The error bar estimation of the flux calibration is derived from the flux variations of the source measured in different apertures and from different standard stars. In cases where two independent measurements were taken, an average of the measured fluxes is quoted in Table 2.4.

As already mentioned, a destriping technique was applied to the final images to clean it of random stripes and thereby improve the image quality. To estimate the impact of the destriping on the photometry of the BDs, we performed the aperture photometry before and after the destriping process. In those cases in which the source is not located close to a stripe, no influence is noticeable. In contrast, in the cases where the BD is close to a stripe, a decrease in the measured count-rate, and consequently in flux, of the BD in the destriped images is perceivable. Nevertheless, this effect is expected, since the stripes in the "raw" images fall within the aperture radii and lead to an overestimation of the count-rate and therefore of the flux.

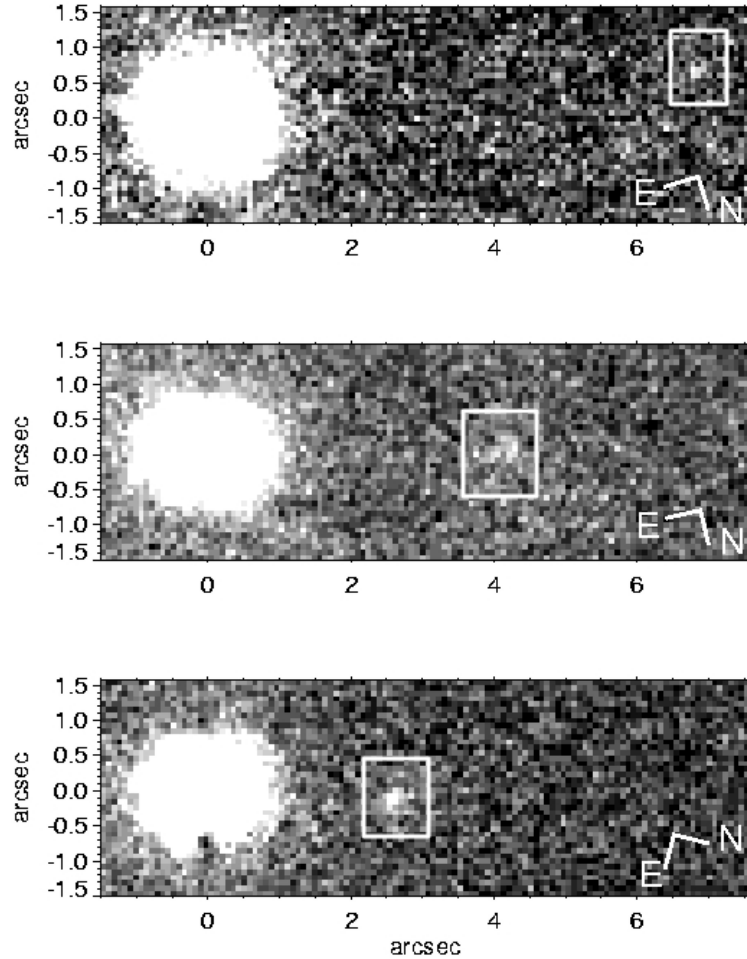
¹ Taken from the list of Cohen et al. (1999)

Table 2.2: Observing Log

Object	Filter	UT date dd/mm/yr	Airmass	DIMM ^a seeing ["]	humidity [%]	DIT [s]	NDIT	# of nods ^c	Int. time ^d [s]	Calibrator
GJ229	PAH1	08/01/06 ^b	1.109	0.91	17-50	0.016	123	12	2172.7	HD 26967, HD 75691
		10/02/06 ^b	1.195	0.79	23-55	0.016	123	18	3259.	HD 41047, HD 75691
	PAH2	03/02/06 ^b	1.044	0.83	20-40	0.008	246	6	1086.3	HD 41047, HD 26967
SIV		10/02/06	1.110	0.84	23-55	0.008	246	6	1086.3	HD 26967, HD 75691
		10/02/06	1.022	0.95	23-55	0.04	48	11	1943.	HD 26967, HD 75691
HD 130948	PAH1	09-10/07/06	1.524	0.67	6-8	0.02	98	22	3967.	HD 133774, HD 99167
	PAH2	11/07/06 ^b	1.541	0.91	7-10	0.01	197	22	3987.3	HD 149009
		04-05/08/06 ^b	1.734	0.71	7	0.01	197	11	1993.6	HD 149009, HD 145897
SIV		03/08/06	1.627	0.86	5-8	0.04	48	11	1943.	HD 145897
		05/08/06	1.606	0.62	6-11	0.04	48	11	1943.	HD 145897
HR 7329	PAH1	07/06/06	1.182	1.05	4-12	0.02	98	22	3967.	HD 178345
	PAH2	21/05/06	1.153	1.36	7-19	0.008	246	11	1991.6	HD 178345
	SIV	07/06/06	1.175	0.88	4-12	0.04	48	22	3886.1	HD 178345
HR 7672	PAH1	10/07/06 ^b	1.341	0.76	6-8	0.02	98	11	1983.5	HD 189695, HD 149009
		12/07/06 ^b	1.405	0.88	6-11	0.016	123	11	1991.6	HD 189695, HD 178345
	PAH2	10/07/06 ^b	1.385	0.81	6-8	0.01	197	11	1993.6	HD 189695, HD 220954
SIV		13/07/06 ^b	1.693	0.78	5-8	0.01	197	11	1993.6	HD 198048, HD 217902
		13/07/06 ^b	1.356	0.82	5-8	0.04	48	15	2649.6	HD 178345, HD 198048

a.) in V band at 550nm, b.) data showed stripes, c.) 23 chops per nod, d.) t=DIT × NDIT × # of chops × # of nods × 4

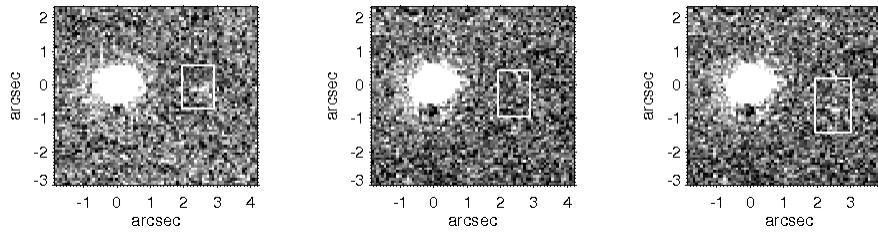
Figure 2.6: VISIR detection images of GJ299 B at $\sim 6.8''$ (upper), HR7329 B at $\sim 4.3''$ (middle) and HD 130948 BC at $\sim 2.5''$ (bottom) at $8.6\mu\text{m}$. To all images a σ filter with a box width of 5 pixel has been applied. Furthermore the N–E orientation of the data is over-plotted in the lower right corner of each image.



2.2.3.2 Detection Limits

To estimate the detection limits as a function of angular separation two approaches were explored. The standard deviation of the intensities within a 1 pixel wide annulus at a given radius was determined, as well as the standard deviation within a box of 5×5 pixels along a random radial direction. Using the obtained noise estimate, the contrast with respect to the peak intensity of the primary was calculated (see, e.g., Figure 2.8). The detection limits delivered by both methods are in good agreement. Additionally, to further test the derived detection limits, artificial companions, with fluxes varying between 2 and 10 mJy, were placed within the data at separations between $1''$ and $5''$. The limiting fluxes of the re-detectable artificial companions match the previously derived detection limits. Up to a separation of $1.5''$ the detection limit is dominated by the photon noise of the central star, and at larger separation the background noise from the atmosphere and the instrument limits our detections.

Figure 2.7: VISIR images of HD 130948 in the SIV filter taken on the 5th of August (left) and on the 3rd of August (middle). The binary brown dwarf companion was detected in the data from the 5th of August and is marked by a box. The flux was measured to be 5.7 ± 0.4 mJy. In the data set from the 3rd of August the companion was not detected. Its approximate location is at the same position as in the left image and also marked by a box. The right image shows the data from the 3rd of August, in which an artificial companion of 4 mJy has been placed. The artificial companion is located somewhat below the expected position of the real companion.



2.2.4 Results

Three of the four brown dwarfs were detected in PAH1, namely GJ 229 B, HR 7329 B and HD 130948 BC (see Figure 2.6), while only HD 130948 BC could be detected in SIV. Note that HD 130948 BC, a binary brown dwarf, was not resolved in our observations. HR 7672 B could not be detected in any of the filters. While the resolution of VISIR is sufficient to separate the brown dwarf and the primary ($0.79''$ - Liu et al. (2002); assuming negligible orbital motion), the data quality in PAH1 and SIV is low. The PSF of the primary is elongated, affecting the area in which the brown dwarf is expected, and thus adding noise.

Table 2.3: Separations and position angles of the detected brown dwarfs.

Object	UT date	sep. ["]	P.A. [°]
GJ 229	10/02/06	6.78 ± 0.05	168.4 ± 0.9
HD 130948	09/07/06	2.54 ± 0.05	103.9 ± 2.4
HR 7329	07/06/06	4.17 ± 0.11	167.2 ± 1.4

In Table 2.3 the measured separations and position angles of the detected brown dwarfs are given. To obtain the separation as well as the position angle of the brown dwarfs relative to their primaries, the pixelscale and N-orientation provided in the image header were used. Golimowski et al. (1998), used the HST's Wide Field Planetary Camera 2 (WFPC2) to observe GJ 229 B at three epochs, which were spread over approximately one year. Orbital motion of GJ 229 B was detected and a relative change of separation of $(0.088 \pm 0.010)''$ per year was measured. In the last 10 years, from November 1996 to February 2006, the separation between GJ 229 A and B changed by $(0.894 \pm 0.05)''$, resulting in an average change of separation of $(0.097 \pm 0.005)''$ per year. For HD 130948, only a minor change of separation is observable. From February 2001 to July 2006 the separation between HD 130948 A and BC decreased by $(0.09 \pm 0.05)''$. In the case of HR 7329 no orbital motion was observable. In Table 2.4 the obtained fluxes for the primary stars and the brown dwarfs, and the upper limits for the non-detections, are listed. In the case of HD 130948 BC the flux measured in

the data set from the 5th of August is quoted, as well as the upper limit obtained on the 3rd of August. While the observations of HD 130948 BC in SIV have been carried out at two different epochs, on the 3rd and the 5th of August, the object was only detectable in the second data set (see Figure 2.7) with a measured flux of (5.7 ± 0.4) mJy. The non-detection of HD 130948 BC in the data set from the 3rd of August can not be explained by a discrepancy in the sensitivity limits, see Figure 2.8. Both data sets clearly reach the same sensitivity limit. Furthermore, simulations of artificial sources showed that a companion with a flux of (4 ± 0.4) mJy (corresponding to a 5σ confidence level) would have been detected in both data sets. Hence, within ~ 48 hours HD 130948 BC varied by at least (1.7 ± 0.6) mJy.

Table 2.4: VISIR photometry of the primaries and brown dwarfs. In case of a non-detection upper limits are provided. The fluxes are quoted in mJy.

Object	PAH1	SIV	PAH2
GJ 229 A	1297. (47.)	923. (33.)	793. (26)
GJ 229 B	3.2 (0.5)	2. (0.3)	4. (0.9) ^a
HD 130948 A	861. (5.)	605. (27.) ^b	478. (6.)
HD 130948 BC	3.8 (0.4)	5.7 (0.4) ^b	1.8 (0.2) ^a
HD 130948 A		553. (27.) ^c	
HD 130948 BC		2. (0.4) ^{a,c}	
HR 7329 A	524. (19.)	404. (3.)	386. (24.)
HR 7329 B	3.2 (2.3)	1.3 (0.2) ^a	2.3 (0.2) ^a
HR 7672 A	880. (36.)	554. (33.)	519. (14.)

a.) limiting background (1σ), b.) 05/08/06, c.) 03/08/06

2.2.5 Discussion

2.2.5.1 Comparison with Models

As a final step we compare our obtained photometry to the models developed by Allard et al. (2001) and Burrows et al. (2006). Using their theoretical spectra, provided online², absolute model fluxes were calculated by integrating the theoretical spectrum over the VISIR filter bandpasses. The object radii R , which determine the absolute spectral flux calibration, were obtained from evolutionary calculations by Burrows et al. (1997). In Table 2.5 the calculated model fluxes are listed. Furthermore, the age and effective temperature combinations for which the object radius was determined are given. From Allard et al. (2001) we employed the AMES-cond and AMES-dusty models, representing the two extreme cases, in which either all dust has disappeared from the atmosphere (AMES-cond) or dust settling throughout the atmosphere is negligible (AMES-dusty). Following Allard et al. (2001) the AMES-dusty models should successfully describe dwarfs with effective temperatures greater than 1800K, while the AMES-cond models are better suited to describe the atmospheres of dwarfs with $T_{eff} \leq 1300$ K.

GJ 229 B: Saumon et al. (2000), have used high-resolution infrared spectra to determine the metallicity, effective temperature and gravity of the T dwarf (see also Table 2.1). While using an age of 0.2 Gyr they derived an effective temperature of $950 \text{ K} \pm 80 \text{ K}$ and a gravity

²<http://perso.ens-lyon.fr/france.allard/> and <http://zenith.as.arizona.edu/burrows/>

Table 2.5: Predicted mid-IR fluxes from different theoretical models. Values consistent within 3σ or with the given upper limit are marked in boldface.

Object	Reference	T_{eff} [K]	$\log g$ [cm/s^2]	[M/H]	age Myr	R/R_{\odot}	PAH1 [mJy]	SIV [mJy]	PAH2 [mJy]	
GJ229B	Allard ^a	900	5.0	0.0	200	0.122	3.30	2.97	5.06	
	Allard ^a	1000	5.0	0.0	200	0.122	4.67	4.55	6.68	
	Allard ^a	1000	3.0	0.0	200	0.122	4.80	6.69	7.94	
	Allard ^a	1000	3.0	0.0	30	0.133	5.70	7.95	9.44	
	Burrows ^c	900	5.0	0.0	200	0.122	3.35	3.0	4.25	
	Burrows ^c	900	5.0	-0.5	200	0.122	3.33	2.46	3.78	
	Burrows ^c	1000	5.0	-0.5	200	0.122	4.25	3.44	4.77	
	Burrows ^c	1000	5.0	-0.5	30	0.133	5.04	4.09	5.66	
	Burrows ^c	1000	4.5	-0.5	30	0.133	5.14	4.99	6.05	
	measured						3.2 ± 0.5	3.2^1	6.7 ¹	
	HD 130948BC	Allard ^b	1900	5.0	0.0	800	0.091	1.65	1.25	1.13
		Allard ^b	1900	5.0	0.0	300	0.102	2.07	1.57	1.42
Allard ^b		1900	3.5	0.0	300	0.102	1.67	1.21	1.11	
Burrows ^d		1900	5.0	0.0	300	0.102	1.53	1.26	1.17	
Burrows ^d		1900	5.0	-0.5	300	0.102	1.49	1.25	1.16	
measured							1.9 ± 0.3	2.9 ± 0.3^3	1.2 ¹	
measured								1.5 ¹		
HR 7329B		Allard ^b	2400	4.0	0.0	12	0.193	1.06	0.91	0.79
		Allard ^b	2600	3.5	0.0	8	0.278	2.80	2.30	2.55
		Allard ^b	2600	3.5	0.0	12	0.229	1.90	1.56	1.73
		Allard ^b	2600	4.0	0.0	12	0.229	1.76	1.44	1.25
		Allard ^b	2800	4.0	0.0	12	0.265	2.84	2.20	1.91
	measured						3.2 ± 2.3	1.9 ¹	2.9 ¹	

a.) AMES-cond models from Allard et al. (2001)

b.) AMES-dusty models from Allard et al. (2001)

c.) L & T cloud-free models from Burrows et al. (2006)

d.) L & T model with clouds from Burrows et al. (2006)

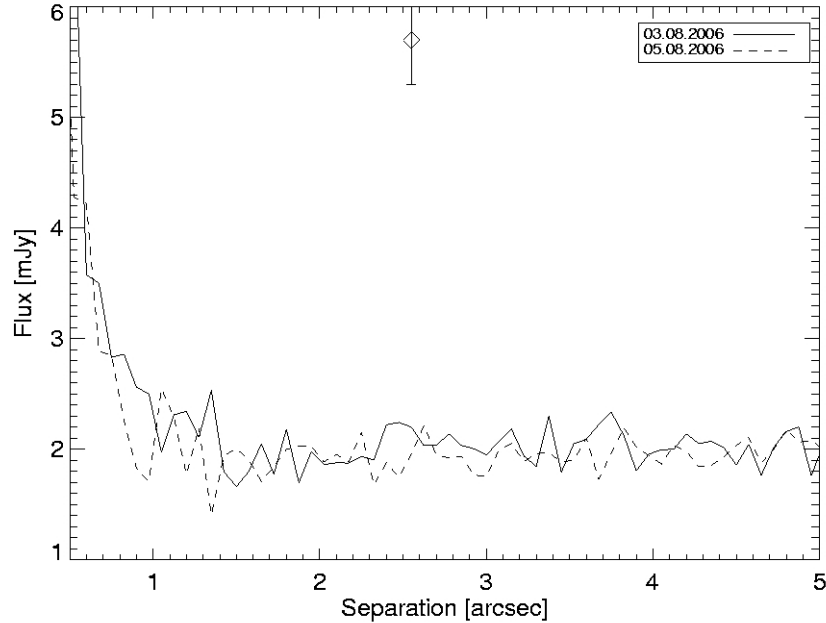
1.) upper limit, limiting background plus 3σ

2.) flux of one component assuming both L4 dwarfs

contribute equally to the measured flux

3.) only 05.08.2006

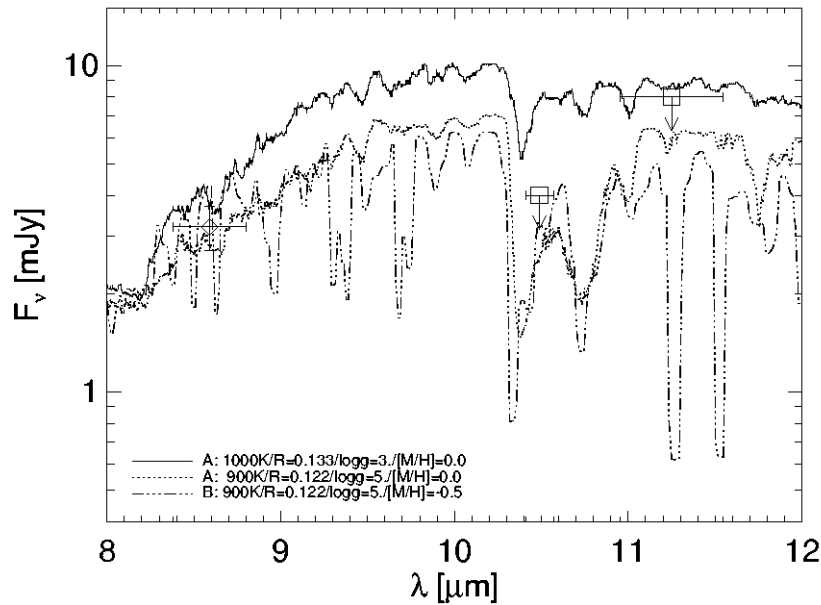
Figure 2.8: Comparison of the limiting background obtained from the two data sets of HD 130948 taken in the SIV filter. The over-plotted point corresponds to the detection on the 5th of August, with a flux of 5.7 mJy.



of $\log g = 5 \pm 0.5$. Later on, Leggett et al. (2002b) compared the observed low- and high-resolution spectra of GJ 229 A and GJ 229 B to theoretical spectra (AMES-models). Their best fit yields an $T_{eff} = 1000 \pm 100$ and a gravity of $\log g \leq 3.5$ for GJ 229 B, as well as a metallicity of $[M/H] \approx -0.5$ and an age of ~ 30 Myr (range 16–45 Myr) for the system. While the metallicity is determined within the spectra fitting procedure, the age is derived by a comparison with evolutionary models, and mainly constrained by the observed luminosity and the derived effective temperature of the A component. Using VISIR mid-IR photometry, absolute model predictions of both Allard et al. (2001) and Burrows et al. (2006) can then be tested for different combinations of T_{eff} , $[M/H]$ and gravity (when available, e.g. see Figure 2.9). From Table 2.5, we see that the PAH1, SIV and PAH2 photometry are consistent with model predictions for a $T_{eff} = 900$ K, $\log g = 5.0$ and $[M/H] = 0$ companion. At solar metallicity, an effective temperature of $T_{eff} = 1000$ K can be excluded at more than 2σ . At subsolar $[M/H] = -0.5$ metallicity, low gravity ($\log g < 4.5$) values remain excluded for $T_{eff} = 1000$ K. Therefore, excluding young ages predictions of Leggett et al. (2002b), the VISIR photometry clearly favours the initial physical parameters proposed by Saumon et al. (2000) for solar and subsolar metallicities

HD 130948 BC: As already mentioned, HD 130948 BC is a binary brown dwarf consisting of two L4 dwarfs. To compare our observations to the model predictions, we assumed that both brown dwarfs contribute equally to the measured fluxes, as the simplest assumption. An unequal distribution of the measured flux on one of the two brown dwarfs would only increase the afterwards described effect. The suggested effective temperature of ~ 1900 K places the binary in the regime of the AMES-dusty models. While the predicted PAH1 flux is in good agreement with our measurements, most models fail to reproduce the SIV flux

Figure 2.9: GJ229B: Comparison of theoretical spectra from Allard et al. (2001) and Burrows et al. (2006) with the VISIR photometry.



detected on August, 5. 2006, but would be consistent with the non-detection on August, 3. 2007. Using the models provided by Burrows et al. (2006) we tested the influence of different metallicities ($[M/H]=0.0$ and $[M/H]=-0.5$) on the predicted fluxes. The change is marginal, only about 0.05 mJy.

2.2.5.2 HD130948BC: Photometric Variability

While analysing the SIV data obtained for HD 130948, we found that the binary companion was detectable in only one of the two data sets. A possible explanation of this result is an intrinsic variability around $10.5 \mu\text{m}$ of one or both of the L dwarfs in the binary. Variability at $10.5 \mu\text{m}$ could either be caused by ammonia (NH_3) or silicates. Since the NH_3 absorption features, which were first identified in the mid-infrared spectra taken with Spitzer/IRAS by Roellig et al. (2004), and Cushing et al. (2006), appear at roughly the L/T transition this is unlikely to be the cause of the observed variability. A more favourable explanation may be an inhomogeneous distribution of silicate clouds, which characterise the atmospheres of L dwarfs with effective temperatures of roughly 1400–2000 K (Burrows et al. (2001)). Future VISIR observations of HD 130948 BC at $10.5 \mu\text{m}$ over different timescales should secure this photometric variability.

2.3 Follow-up Observations of HD 130948

2.3.1 Observation

In order to study the variation observed in HD 130948 BC we requested and were granted follow-up observations with VISIR at the VLT. The observations were carried out in March 2008 in 'Visitor mode' using the narrow band filters centered at $8.6\ \mu\text{m}$ (PAH1) and $10.5\ \mu\text{m}$ (SIV). The target was monitored over three half nights switching between the two filters. This approach was chosen to determine whether the suspected variability is confined to the region around $10.5\ \mu\text{m}$ or whether it may be a global feature.

Table 2.6: Observing Log of the HD 130948 observations in March 2008.

UT Date	Filter	Air-	seeing	DIT	N-	# of	Int. time	Calibrator
dd/mm/yy		mass	[']	[s]	DIT	nods	[s]	
25/03/08T05	PAH1	1.81	0.74	0.0125	157	10	1805.5	1, 2, 3, 4
25/03/08T07	PAH1	1.62	0.65	0.0125	157	11	1986.1	1, 2, 3, 4
26/03/08T05	PAH1	1.73	0.47	0.0125	157	12	2166.6	2, 5, 6, 7
26/03/08T08	PAH1	1.58	0.48	0.0125	157	11	1986.1	2, 5, 6, 7
26/03/08T09	PAH1	1.77	0.75	0.0125	157	5	902.8	2, 5, 6, 7
27/03/08T05	PAH1	1.72	0.67	0.0125	157	10	1805.5	2, 3, 5, 8, 9
27/03/08T08	PAH1	1.61	0.74	0.0125	157	10	1805.5	2, 3, 5, 8, 9
27/03/08T09	PAH1	1.84	0.83	0.0125	157	7	1263.8	2, 3, 5, 8, 9
25/03/08T05	SIV	1.63	0.77	0.025	78	12	2152.8	2, 3
25/03/08T06	SIV	1.51	0.65	0.020	78	13	1865.8	4
26/03/08T05	SIV	1.57	0.36	0.025	78	14	2511.6	2, 5, 6
26/03/08T07	SIV	1.52	0.32	0.025	78	13	2332.2	2, 5, 6
27/03/08T05	SIV	1.58	0.79	0.025	78	13	2332.2	2, 3, 5, 8
27/03/08T07	SIV	1.52	0.56	0.025	78	17	3049.8	2, 3, 5, 8

(1) HD 99167; (2) HD 145879; (3) HD 98118; (4) HD 149009; (5) HD 93813;
 (6) HD 187660; (7) HD 189695; (8) HD 115478; (9) HD 173780

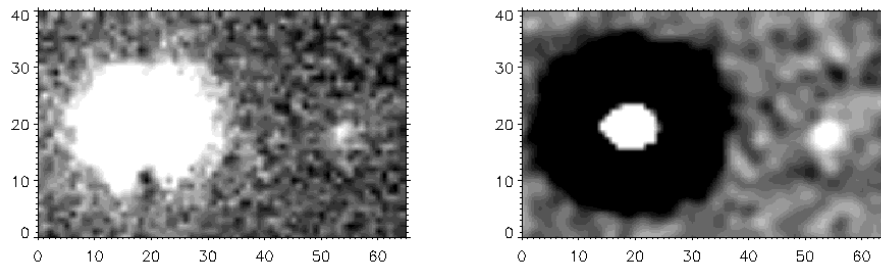
2.3.2 Data reduction and background filtering

Despite the standard chopping and nodding technique the data still showed global and local background variations. To remove these background variations, which limit the sensitivity, we applied a special wavelet filtering technique to the data before averaging over the single beams. The same procedure has to be applied to the standard stars, to achieve an exact calibration when performing photometry. Furthermore the size of the aperture has to be chosen small enough to avoid the rebound dark zone (see Figure 2.10), which is an intrinsic feature of the filtering process. Tests have shown that the photometry is not influenced by the filtering, but the signal to noise is improved. As an example, the SIV data of HD 130948BC from August, 5. 2006, is shown in the Figure 2.10 and the flux and S/N values are given in Table 2.7.

Table 2.7: Example of the measured photometry and the signal to noise before (4th and 5th column) and after (6th and 7th column) wavelet filtering. The values quoted in brackets are the uncertainties of the flux arising due to different standard stars.

Object	date	filter	flux	S/N	flux	S/N
	[ddmmyy]		[mJy]		[mJy]	
GJ 229 B	080106	PAH1	3.0 (0.3)	2.5	2.6 (0.4)	5.2
	100206	PAH1	2.9 (0.3)	1.6	4.7 (0.3)	5.2
HD 130948 BC	100706	PAH1	3.8 (0.4)	4.8	3.4 (0.2)	8.5
	050806	SIV	5.7 (0.4)	2.9	5.6 (0.4)	6.2
HR 7329 B	070606	PAH1	2.6 (0.2)	3.2	2.3 (0.2)	4.6

Figure 2.10: Comparison of the image quality before and after the background removal by filtering.



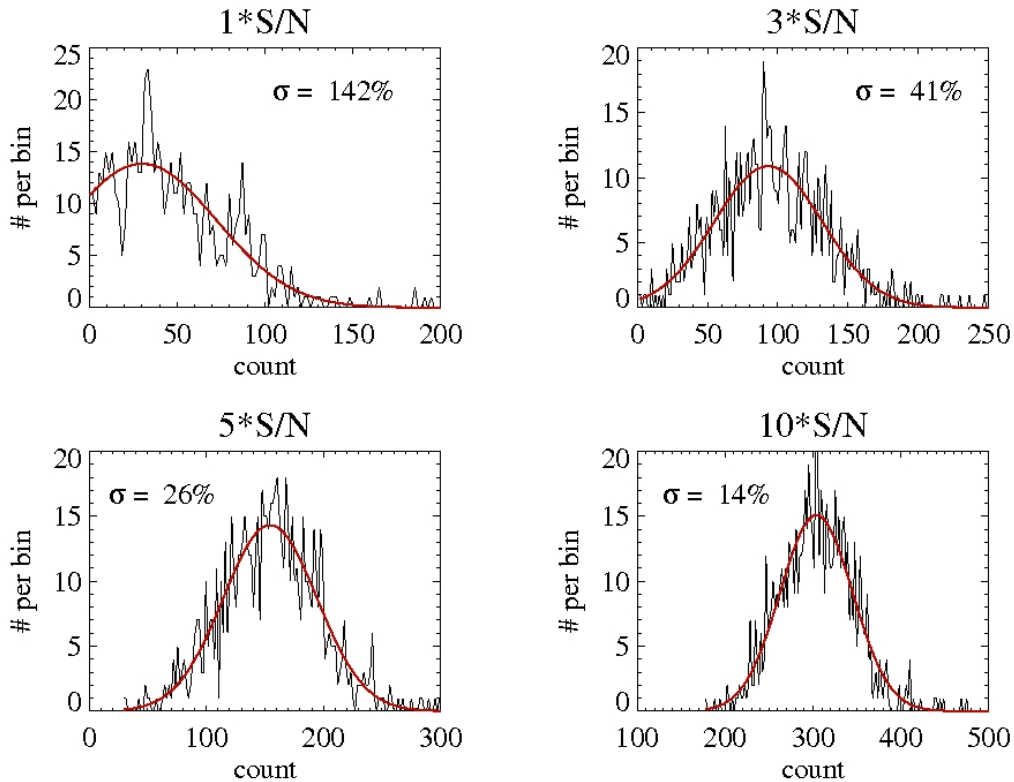
2.3.3 Simulations

To evaluate the photometric error of each independent observation, we performed extensive simulation, placing artificial sources into the data³. As artificial source the PSF of an associated standard star, scaled to the required signal-to-noise (S/N) was taken and placed at randomly determined positions. These coordinates are stored and passed on to the automatic photometry program, which is based on the IDL/ATV routine. For all data sets simulations for a variety of S/N values were run with a total of 1.000 artificial sources per S/N value. In case the positions of the artificial source overlaps with a beforehand defined area around the coordinates of HD 130948A and HD 130948BC, the result of the photometry is rejected. Thus the number of valid photometric points is reduced too about 600 to 650. The remaining points are binned in an histogram and a Gaussian function is fitted to the distribution, see Figure 2.11. The standard deviation of the Gaussian fit is taken as the photometric error of the corresponding S/N level.

In a second step we run simulations following the described approach to evaluate the influence of the background filtering on the signal to noise and the photometric error of a potential source. Therefore artificial sources with known signal to noise were placed in the reduced unfiltered images. After placing the artificial source in the data, the wavelet filtering technique

³Completely reduced image on which photometry was performed.

Figure 2.11: Example plot showing the results of the simulation for four different signal-to-noise values. To each distribution a Gaussian, whose standard deviation σ is given, was fitted.



was applied to obtain an filtered version of the artificial source. Photometry of the artificial sources in the un-filtered and filtered images and the estimation of the photometric error was done as described above. Additionally the mean signal to noise of the artificial sources in the filtered images was calculated. We tested the correlation between S/N and the photometric error of the un-filtered and filtered images on three different data sets. The results are illustrated in Figure 2.12. Both the un-filtered and the filtered data set show a correlation between the S/N of the source and the corresponding photometric error. For the un-filtered data the correlation can be expressed by : $y = 49/x$; while the filtered data follows $y = 108/x$. This is in agreement with the correlation of the S/N before and after filtering. The S/N after filtering is ~ 2.1 times higher than before. While the filtering process obviously increases the signal to noise ratio of the source it has no influence on the photometric error. The photometric error after applying the filtering technique is identical to the photometric error before filtering.

2.3.4 Results

Table 2.8 lists all the photometric data points obtained during the observations in 2006 and 2008 for the SIV and the PAH1 filter.

Figure 2.12: The three graphs display the correlations between the signal-to-noise (S/N) and the photometric error before and after the background filtering.

Upper graph: data points in black are before filtering, those in green are after filtering.

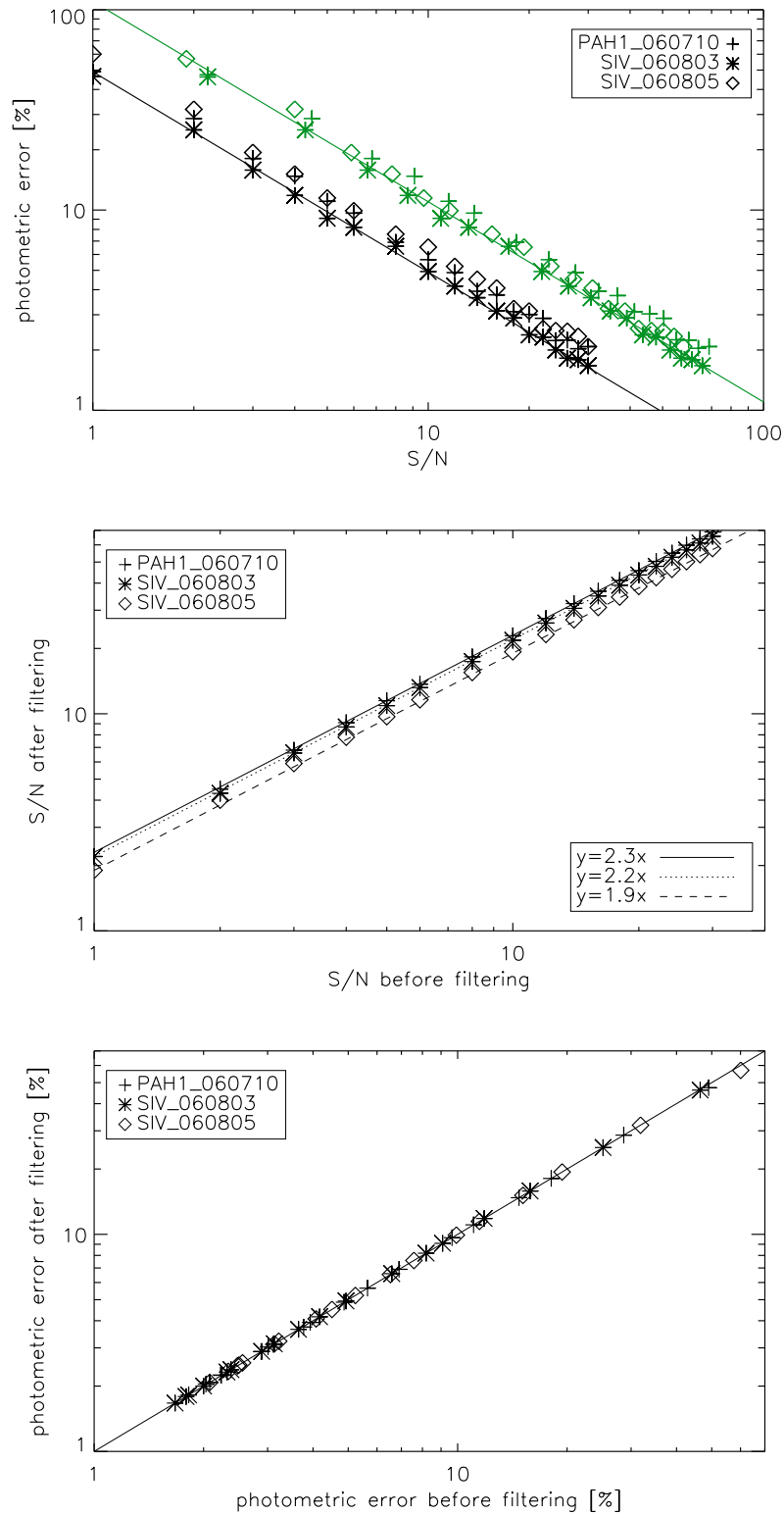


Table 2.8: The table states the fluxes, background limiting sensitivities and the signal to noise (S/N) measured for all observations of HD 130948BC. The measurements were obtained after applying the background filtering technique to all observation from 2006 and 2008. In red: 3σ upper limits.

date	filter	flux	simu	bg limit	S/N
dd/mm/yy		[mJy]	[%]	[mJy]	
10/07/06	PAH1	3.4 (0.2)	12.	0.4	8.5
03/08/06	SIV	2.7	41.	0.9	3.
05/08/06	SIV	5.6 (0.4)	19.	1.0	6.2
25/03/08T05	PAH1	2.4 (0.5)	80.	1.4	1.7
25/03/08T07	PAH1	4.4 (0.7)	25.	1.2	3.7
26/03/08T05	PAH1	4.0 (0.4)	21.	0.8	5.0
26/03/08T08	PAH1	3.6 (0.4)	25.	1.0	3.6
26/03/08T09	PAH1	3.7 (0.5)	38.	1.2	3.1
27/03/08T05	PAH1	3.9 (0.4)	39.	0.9	4.3
27/03/08T08	PAH1	3.9 (0.4)	28.	1.0	3.9
27/03/08T09	PAH1	4.2 (0.5)	30.	1.1	3.8
25/03/08T05	SIV	4.3 (0.5)	55.	2.2	2.0
25/03/08T06	SIV	5.7	32.	1.9	3.
26/03/08T05	SIV	3.9	35.	1.3	3.
26/03/08T07	SIV	3.6	26.	1.2	3.
27/03/08T05	SIV	3.6 (0.3)	43.	1.4	2.6
27/03/08T07	SIV	2.8 (0.2)	51.	1.1	2.6

Table 2.9: Parameters put into and results obtained from the variability tests.

Filter	N	\bar{f}	\bar{f}^*	χ^2	p	η
PAH1	9	3.72	3.90	1.79	98.7	0.41
SIV	4	4.08	3.95	2.95	39.9	0.91
SIV	8	4.03	3.75	5.51	59.8	0.72

To test whether the photometric measurements show evidence of variability we used two statistic approaches. The first is the χ^2 test:

$$\chi^2 = \sum_{i=1}^{i=N} \left(\frac{f_i - \bar{f}}{\sigma_i} \right)^2 \quad (2.1)$$

- f_i - flux of measurement i
- σ_i - photometric error of measurement i
- \bar{f} - mean flux of all measurements
- N - number of measurements

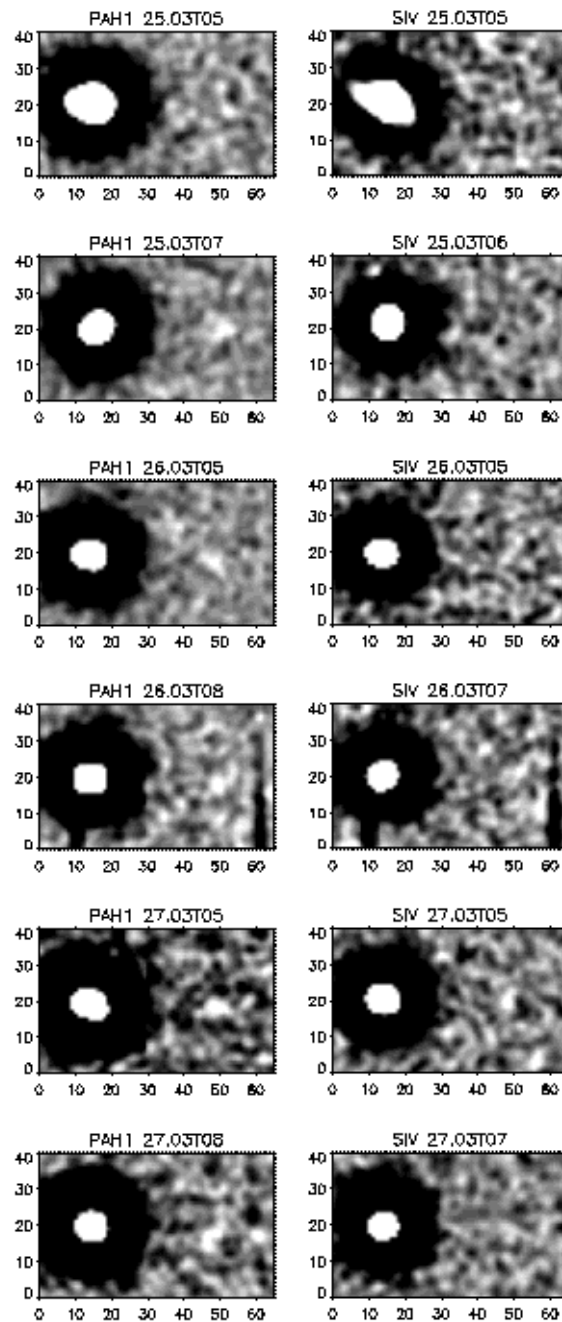
It evaluates the probability that the deviations of the photometric points are consistent with the photometric errors (Bailer-Jones & Mundt (1999), Morales-Calderón et al. (2006)). The null hypothesis for the test is that there is no variability. From the yielded χ^2 the probability (p) that the null hypothesis is true can be determined (look up tables). Thereby a large χ^2 indicates a greater deviation and thus a smaller p. If $p < 0.01$ we claim evidence for variability. The second test was introduced by Enoch et al. (2003) as a more robust statistic approach. They defined:

$$\eta = \frac{1}{N-1} * \sum_{i=1}^{i=N} \frac{|f_i - \bar{f}^*|}{\sigma_i} \quad (2.2)$$

where f_i , σ_i and N are as above and \bar{f}^* is the median flux of all measurements. If $\eta < 1$ than there is no evidence for variability, while for an $\eta \gtrsim 1$ the object is likely to be variable, but Monte-Carlo-Simulations would be necessary to obtain the probability with which the object is variable. Both statistics implicit the assumption that the random scatter in the observations is Gaussian, but the η -test is likely to be more robust in case of outliers.

Both tests were applied to each filter. For the SIV data points we calculated the χ^2 - and the η -test twice. One time only the detected data points were taken into account, disregarding the non-detections. The second time non-detections were accounted for by using the 3σ upper limit when calculating χ^2 and η . The results from both tests are given in Table 2.9. Neither the χ^2 - nor the η -test yields any evidence for variability either in PAH1 or SIV. All three computed values for η are well below 1 indicating that the source is not variable. While the probability calculated from the χ^2 - test confirms non-variability for PAH1, the result is much more uncertain for SIV, but still in favour of non-variability.

Figure 2.13: Sequence of the March 2008 observations of HD 130948 BC in PAH1 and SIV.



2.4 Conclusion

Using VISIR at the VLT, we performed a mini-survey of brown dwarfs in binary systems. The four selected brown dwarfs were imaged in three narrow band filters at 8.6, 10.5 and 11.25 μm . At 8.6 μm three of the brown dwarfs were detected and photometry was obtained. None of the brown dwarfs was detected at 11.25 μm , and only HD 130948 BC was detected at 10.5 μm . The observations of HD 130948 BC at 10.5 μm indicate a possible variation of one or both brown dwarfs of the binary.

To constrain the atmospheric properties of the brown dwarfs we compared the mid-infrared photometry to theoretical model spectra by Allard et al. (2001) and Burrows et al. (2006). The measured mid-infrared fluxes and upper limit of GJ 229 B are consistent with the characteristic parameters obtained, by Saumon et al. (2000) ($T_{\text{eff}} \sim 950 \text{ K}$, $\log g \sim 5$, respectively), while values of the effective temperature and gravity as suggested by Leggett et al. (2002b) ($T_{\text{eff}} \sim 1000 \text{ K}$, $\log g \leq 3.5$, respectively) result in too high model fluxes. As for HD 130948 BC, the model fluxes for $T_{\text{eff}} \sim 1900 \text{ K}$, $\log g \leq 5$ fit the measurement at 8.6 μm and the upper limits obtained at 10.5 μm and 11.25 μm . Nevertheless, the models are not in agreement with the flux measured for the detection of HD 130948 BC at 10.5 μm during one observing epoch. The disagreement of the two observation of HD 130948 BC at 10.5 μm led us to request follow-up observation to study the behaviour of the flux of the binary brown dwarf in two filters over an extended time interval. The observations yielded eight more data points in the narrow band filter around 8.6 μm and three detections of HD 130948 BC at 10.5 μm . In order to analyse whether the variations seen in the fluxes at 8.6 μm and 10.5 μm are statistically relevant we applied two statistical tests to both data sets taken in the different filters. From the results of both tests variability can neither be confirmed in PAH1 nor in SIV.

Chapter 3

Searching for Low-Mass Companions in the Mid-Infrared

3.1 Motivation

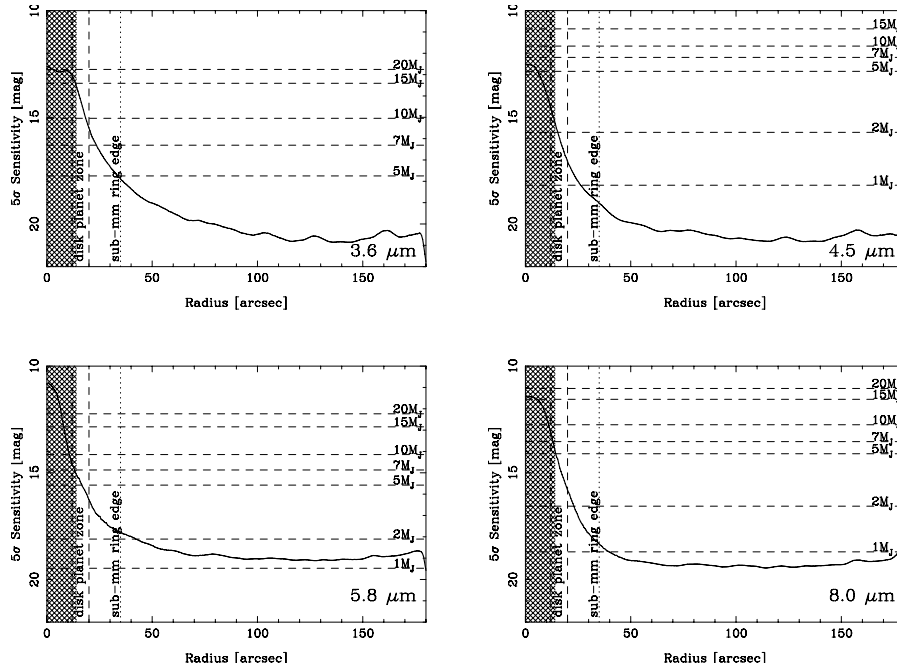
3.1.1 Previous Work

There are numerous surveys which have been or are searching for brown dwarfs and planetary companions, but most of them were or are carried out in the near-infrared concentrating on near-by, young stars (Metchev & Hillenbrand (2004), Masciadri et al. (2005), Chauvin et al. (2006), Biller et al. (2007), Neuhäuser et al. (2006)). Only three projects were or are conducted in the mid-infrared wavelength regime or in the near-infrared L and M bands. One of the first attempts was a $10\mu\text{m}$ broadband imaging survey carried out by van Buren et al. (1998). Using the Palomar 5 Meter telescope they observed eight near-by stars to search for sub-stellar companions. No detection was achieved, but objects brighter than 10mJy at separations between $2''$ - $10''$ from the primary would have been detectable. For the observed stars this upper flux limit translates into companions just slightly below the hydrogen-burning limit.

More recent surveys have been carried out by Kasper et al. (2007) and Heinze et al. (2006), whereas the last mentioned project is still on-going, with the aim to survey 50 near-by, moderate-aged stars for giant extrasolar planets. The observations are planned to be done in L' ($3.8\mu\text{m}$) and M- ($4.8\mu\text{m}$) band using the Clio camera together with adaptive optics system on the 6.5m MMT telescope. At these wavelengths giant planets should be even visible around near-by, old stars, up to 5.Gyr. So far 7 out of the 50 target stars have been observed, and Monte Carlo simulations to demonstrate the ability to detect Jupiter mass planets around them, have been performed. The simulations show that, in special cases, planets down to 6. Jupiter masses orbiting an 1.Gyr old star are detectable.

Finally, Kasper et al. (2007) observed a small sample of 22 young, nearby stars using the VLT/NACO system in the L band. The target sample is comprised out of members of the Tucana association and the β Pic moving group, which ages are estimated to be between 10. and 30. Myr. No companion has been detected, but the observations were sensitive to objects with masses down to $1. - 2M_J$ at separations larger than 5. to 30. AU.

With the rise of the *Spitzer Space Telescope* the mid-infrared wavelength regime became accessible to direct imaging searches for brown dwarfs and extrasolar planets. An example is

Figure 3.1: Sensitivity limit of ϵ Eri from the IRAC observation by Marengo et al. (2006).

the survey of $5' \times 5'$ fields surrounding stars in the solar neighbourhood conducted by Luhman et al. (2007) with the IRAC instrument. As an intermediate result two T dwarf companions to the near-by stars HN Peg and HD 3651 at separations of $43.''2$ and $42.''9$, respectively, have been announced. But, IRAC should be able to detect even lower mass objects, as shown by the observations of the main sequence star ϵ Eri (Marengo et al., 2006). Depending on the filter, sensitivity limits down to 1 Jupiter mass were reached (see Figure 3.1). As a disadvantage of the low resolution of the instrument and the required long integration times the area closest to the star will naturally be saturated and hence useless for the scientific purpose. For ϵ Eri a region (cross-hatched in Figure 3.1) within a radius of $14''$ (45 A.U.) from the star had to be excluded because of saturation effects and high residual noise after PSF subtraction.

But this drawback opens a niche for ground-based mid-infrared instruments.

3.1.2 Limits

While space-based mid-infrared observatories have the clear advantage of sensitivity compared to ground-based instruments, they are limited by the size of the primary mirror. Ground-based 8m class telescopes may not reach the same sensitivity limits as the Spitzer Space Telescope, but they have a much higher resolution, which makes them competitive when searching for companions at small angular separations from the primary star.

To get a rough notion of what kind of objects one would expect to detect with either of the two mid-infrared images at VLT and GEMINI, one has to combine the nominal sensitivity limit of the instrument with prediction from theoretical models. The nominal sensitivity lim-

Table 3.1: Predicted fluxes calculated from theoretical models (Allard et al., 2001) assuming an age of 0.5 Gyr.

M	M	T_{eff}	$\log g$	R	5 pc		10 pc	
					PAH1	Si5	PAH1	Si5
[M_{\odot}]	[M_J]	[K]		[R_{\odot}]	[mJy]	[mJy]	[mJy]	[mJy]
0.007	7.3	500	4.2	0.112	0.4	1.2	0.1	0.3
0.010	10.5	600	4.4	0.110	0.9	2.0	0.2	0.5
0.015	15.7	800	4.6	0.107	2.4	4.2	0.6	1.1
0.020	21.0	900	4.7	0.104	3.2	5.3	0.8	1.3

Table 3.2: Predicted fluxes calculated from theoretical models (Allard et al., 2001) assuming an age of 1 Gyr.

M	M	T_{eff}	$\log g$	R	5 pc		10 pc	
					PAH1	Si5	PAH1	Si5
[M_{\odot}]	[M_J]	[K]		[R_{\odot}]	[mJy]	[mJy]	[mJy]	[mJy]
0.0085	8.9	450	4.3	0.107	0.3	0.7	0.07	0.2
0.01	10.5	500	4.4	0.107	0.4	1.1	0.1	0.3
0.02	21.0	800	4.7	0.100	2.1	3.7	0.5	0.9
0.03	31.4	1000	4.9	0.096	3.9	5.3	1.0	1.3
0.04	41.9	1300	5.1	0.093	7.0	7.6	1.7	1.9

its for both VLT/VISIR and GEMINI/T-ReCS are published on the respective web pages. Since only one filter of each instrument will be of interest in the context of this work, the discussion will be limited to the filters in question. The PAH1 filter, centered at $8.6 \mu\text{m}$, of VISIR is given with a nominal sensitivity limit of $5 \text{ mJy } 10 \sigma/h$, while the T-ReCS web page states $1.6 \text{ mJy } 5 \sigma/30 \text{ min}$ (roughly $\sim 2.2 \text{ mJy } 10 \sigma/hr$) as sensitivity limit for the Si5 filter, centered at $11.7 \mu\text{m}$.

Taking theoretical models, like those from Allard et al. (2001), one can calculate the expected mid-infrared fluxes of objects with certain age, mass and effective temperature combinations, by integrating the theoretical spectra over the filter passband. Tables 3.1, 3.2 and 3.3

Table 3.3: Predicted fluxes calculated from theoretical models (Allard et al., 2001) assuming an age of 5 Gyr.

M	M	T_{eff}	$\log g$	R	5 pc		10 pc	
					PAH1	Si5	PAH1	Si5
[M_{\odot}]	[M_J]	[K]		[R_{\odot}]	[mJy]	[mJy]	[mJy]	[mJy]
0.015	15.7	400	4.6	0.098	0.1	0.4	0.03	0.1
0.030	31.4	600	5.0	0.090	0.9	1.6	0.2	0.4
0.040	41.9	750	5.2	0.085	1.3	2.1	0.4	0.5
0.050	52.4	950	5.3	0.082	2.7	3.2	0.7	0.8
0.060	62.8	1100	5.4	0.079	3.5	4.0	0.9	1.0

list exemplary results of such an exercise. The calculated theoretical fluxes are supposed to be taken as a guideline to get a feeling for what kind of object should be detectable (marked in bold face in all three tables) in a companion search survey employing ground based telescopes.

3.2 Survey

The most stringent limitation of surveys searching for faint companions are residual artefact's and time varying aberrations in the point-spread-function (PSF) around the bright primaries. One way to overcome the limitations of the optical and near infrared surveys is to observe at longer wavelengths. In the mid-IR ($10\mu\text{m}$), the residual optical aberrations of the PSF are of much less concern, and for 8m-class telescopes, they can basically be neglected at angular separations larger than 1 arcsec from the primary star. This project aims at detecting low mass companions to bright, near-by stars, using the mid-infrared facilities VISIR at the VLT and TReCS at Gemini/South. The favourable flux contrast between the primary and a potential secondary in the $10\mu\text{m}$ regime allows us to search for companions having temperatures below 1000K at separations of only 1" to 3" from the primary. E.g., for a star at a distance of 5 parsec from the sun these separations translate to 5- 15 AU, a domain highly interesting for planetary formation, and where orbital periods get too long to make such objects easily (i.e. within a short time span) detectable by radial velocity or astrometric monitoring. We stress that our observations are complementary to other ground or space based efforts (both direct imaging and indirect methods), since we target a separation region hard to access.

3.2.1 Target Sample

The complete sample of the VISIR and T-ReCS observations is compound of fourteen stars, all selected according to the following three criteria: optical and near-infrared brightness, distance and visibility. Since both the VLT and the GEMINI/South are located on the southern hemisphere, possible targets were required to have declinations southward of $+15^\circ$. Concerning the first criteria the targets were required to be brighter than $V=5$ mag and $K_s=3$ mag, so that they are most likely to be excluded from common optical and near-infrared, direct imaging surveys. As a final requirement we wanted the targets to be near-by (<10 pc) to be able to resolve companions at physical distance of 5 to 15 AU, a domain highly interesting for planetary formation. Not all targets fulfill this last constraint, which is due to observational time constraints and the lack of fitting targets to observe.

Three of the observed targets are planet host candidates. One of them is β Hyi a G0 main sequence star situated at a distance of ~ 7.5 pc from the Sun. Since 2002 the star is known to have a linear radial velocity trend (Endl et al., 2002), most likely caused by giant planet or substellar companions located at a separation $>1''$. The remaining two targets are ϵ Eri and ϵ Ind A, both described in more detail below.

ϵ Eri : At a distance of only 3.2 pc is ϵ Eri the nearest star with a detected circumstellar disc (Greaves et al., 1998) and a planet candidate. It has been extensively studied using radial velocity, astrometry and direct imaging techniques. Starting in 1995, Walker et al. (1995)

Table 3.4: Combined target list of the VISIR (note: V) and T-ReCS (note: T) observations.

Object	π [mas]	SpT	age [Gyr]	range [Gyr]	V [mag]	K [mag]	IRAS 12 μ m [Jy]	note
Sirius	379.21	A1 V	0.17 ⁸ ; 0.24 ⁹	0.23–0.25 ⁹	-1.47	-1.39	143.	V
ϵ Eri	310.74	K2 V	0.85 ⁷	0.7–0.9 ^{3,4,5,6,7}	3.73	1.78	9.52	V, T
Procyon A	285.93	F5 IV	1.7 ^{1,2}	1.5–1.9 ^{1,2}	0.34	-0.66	79.1	V
ϵ Indi A	275.79	K4 V	1.3 ²	0.8–2.0 ²	4.69	2.24		V, T
τ Cet	274.18	G8 V	0.3 ¹ ; 7.2 ² ; 5.1 ³ ; 10 ⁷	0.2–12.1 ^{2,7}	3.50	1.79	9.56	V
Altair	194.45	A7 V	1.2 ²	1.1–1.4 ²	0.77	0.10	33.0	V
36 Oph	167.08	K2 V			4.32		5.81	V
δ Pav	163.74	G8 IV	9.3 ¹	5.5–10.8 ¹	3.56	1.93	7.67	V
β Hyi	133.78	G0 V	5.2 ¹	3.5–7.0 ¹	2.80	1.37	11.8	T
ζ Tuc	116.38	F9.5 V	3.5 ¹ ; 6.5 ²	2.4–10.7 ^{1,2}	4.20	2.77	3.18	V
β Vir	91.74	F9 V	2.7 ¹ ; 2.6 ² ; 4.5 ³	2.2–3.2 ^{1,2}	3.61	2.27	5.22	V
β Leo	90.16	A3 V	0.2 ² ; 0.1 ⁷	0.1–0.4 ^{2,7}	2.14	1.88	6.97	V
Arcturus	88.85	K1.5 III			-0.04	-2.91	793.	V

References: 1.) Holmberg et al. (2007); 2.) Lachaume et al. (1999); 3.) Wright et al. (2004); 4.) Saffe et al. (2005); 5.) Henry et al. (1996); 6.) Song et al. (2000); 7.) Di Folco et al. (2004); 8.) Rieke et al. (2005); 9.) Liebert et al. (2005); 10.) Porto de Mello et al. (2008)

presented radial velocity observations suggesting a planet candidate in an about ten year long orbit around ϵ Eri. Three years later, Cumming et al. (1999) published radial velocity data taken with the Lick Observatory showing also significant variations, but with a period of only 6.9 years. Combining all the existing radial velocity observations with additional data from the McDonald Observatory Planet Search Program (Cochran & Hatzes, 1993), Hatzes et al. (2000) confirmed the presence of long period radial velocity variations most likely to be explained by a planetary companion with a period of 6.9 years. Additional evidence for the planetary companion ϵ Eri b comes from the astrometric observations spanning a total time of about 15 years (Benedict et al., 2006). In combination with the radial velocity data the authors determined for ϵ Eri b a period of 6.85 ± 0.03 yr, a perturbation semimajor axis of $\alpha = 1.88 \pm 0.2$ mas and an inclination of $i = 30.1^\circ \pm 3.8^\circ$. This inclination is consistent with the disc inclination determined by Greaves et al. (2005). Assuming a stellar mass of $M_\star = 0.83 M_\odot$ for ϵ Eri A, Benedict et al. (2006) calculate a mass of $M = 1.55 M_J \pm 0.24 M_J$ for ϵ Eri b. Furthermore, the radial velocity data seems to indicate a long-term linear trend, consistent with a Jupiter-mass object at larger separations ($P \sim 50 - 100$ yr). The suggestion that ϵ Eri may harbour a second planet has already been made by Deller & Maddison (2005). They speculated, that a second planet, ϵ Eri c may have shaped the discs morphology.

ϵ Ind : The system consists of a K4 main sequence star and a binary brown dwarf companion at a projected separation of about 1460 AU. The physical companion, dubbed ϵ Ind BaBb, has been discovered in 2003 (Scholz et al., 2003) and was soon afterwards found to be a binary consisting of two T dwarfs (Volk et al. (2003), McCaughrean et al. (2004)). The two components have spectral types of T1 and T6 and estimated masses of $47 \pm 10 M_J$ and $28 \pm 7 M_J$, respectively, assuming an age of 1.3 Gyr for the system (McCaughrean et al., 2004). However, new astrometric monitoring data of the ϵ Ind system points towards a much higher total mass of $121 M_J$ for the brown dwarf binary (Cardoso et al., 2008), implying that the system may be as old as 5 Gyr.

Furthermore, radial velocity data of ϵ Ind A shows a linear trend most likely caused by a distant stellar companion as well as by a very long-period ($P > 20$ yrs) planetary companion (Endl et al. (2002)). The observations were carried out with the ESO Coudé Echelle Spectrometer (CES) on La Silla. The best-fit to the RV measurements gives an RV shift of 0.012 ± 0.002 m/s per day. The rms scatter around the slope is given as 11.6 m/s. Until now no visual companion has been found and, even a deep search with VLT/NACO in H and Ks did not reveal a companion (Geißler et al. (2007)). The observations were limited to objects with $H < 16$ mag and $K_s < 15.6$ mag at a separation of $3''$. Applying theoretical models (Baraffe et al., 2003) the limiting magnitudes were converted into a lower mass limit of $15 M_J$, assuming a system age of 1 Gyr. Thus, the yet unidentified radial velocity companion of ϵ Ind A is most likely substellar.

3.2.2 Observations and Data Reduction

As already mentioned observations were carried out using the mid-infrared facilities at the VLT (VISIR) and the GEMINI/South (T-ReCS).

Table 3.5: Log of the GEMINI/ T-ReCS observations.

Target	Date	P.A.	Airmass	FRM time	Int. time	Calibrator	note
	ddmmyy	[%]		[ms]	[s]		
ϵ Eri	010907	0.	1.147	25.856	926.67	HD23249	
ϵ Eri	010907	20.	1.082	25.856	926.67	HD23249	
ϵ Ind	160807	0.	1.120	25.856	926.67	HD211416	set1
ϵ Ind	160807	340.	1.156	25.856	926.67	HD211416	set1
ϵ Ind	210807	0.	1.122	34.474	926.67	HD211416	set2
ϵ Ind	210807	340.	1.167	34.474	926.67	HD211416	set2
β Hyi	270807	0.	1.571	25.856	926.67	HD224889	set1
β Hyi	270807	20.	1.509	25.856	926.67	HD224889	set1
β Hyi	270807	0.	1.465	25.856	926.67	HD224889	set2
β Hyi	270807	20.	1.464	25.856	926.67	HD224889	set2

GEMINI/South : The Observations with T-ReCS were conducted in August and September 2007 in service mode. Each target was imaged at two different instrument angles separated by 20° in the Si5 broad band filter centered at $11.7\mu\text{m}$. Table 3.5 lists the basic set-up parameters and observing conditions for all T-ReCS observations. During the observations the nodding direction was chosen to be parallel, with a nod and chop throw of 15 arcsec. The chopping angle was tilted between 30° and 50° east of north, so that per chopping cycle the telescope was only half the time on source. Background removal was done by subtracting the frames of corresponding chopping positions of each nod position and afterwards subtracting the images from the two corresponding nodding positions. The final step is to align and average all frames of each observation block.

VLT : The observations with the VISIR instrument were conducted during two nights of 'Visitor Mode' observations in March and July 2008. Visitor mode was required since we employed VISIR's the newly implemented 'Burst mode'. The 'Burst mode' is essentially a lucky imaging approach. While during standard observations about a hundred to two hundred single millisecond integrations are averaged before they are written to file, each single integration is saved separately during 'Burst mode' observations. This technique allows to align the PSF's of all single integrations before averaging them and thus to correct displacements and PSF jumps which may occur during the observations. We choose to observe all targets in the narrow-band filter centered at $8.6\mu\text{m}$ (PAH1), since it was the most sensitive filter offered for VISIR at the time. The chopping and nodding direction was set to 'perpendicular' with a chop and nod throw of $8''$. All observations were conducted using the small pixel scale of $0.075''$ per pixel. As with the T-ReCS observations each target was observed at two instrument position angles separated by 30° . More information can be found in Table 3.6.

Since all of the targets are rather bright, they induce striping in the VISIR detector. The pattern of the stripes is regular (every sixteen pixel) and can effectively be removed by a destriping algorithm developed by E. Pantin. The destriping technique was applied to all raw data frames before continuing with the subtraction of the chopping and nodding frames to remove the background. Since we choose the perpendicular nodding direction with a small chop and nod throw, the reduced images contain four beams (four images of the target at the

Table 3.6: Log of VLT/VISIR observations.

Target	UT date	P.A.	Airmass	seeing	DIT	# of	Int. time ²
	ddmmyy	[°]		["]	[ms]	beams ¹	[s]
Sirius	280308T00:00	0	1.08	1.29	12.5	152640	1908.0
Sirius	280308T01:06	0	1.24	1.18	12.5	152640	1908.0
Procyon	280308T02:25	-30	1.54	1.39	10.0	79600	796.0
Procyon	280308T03:00	0	1.79	0.99	12.5	68688	858.6
β Leo	280308T03:59	0	1.29	0.85	12.5	76320	954.0
β Leo	280308T04:29	0	1.31	0.77	20.0	47520	950.4
β Leo	280308T05:01	-30	1.40	0.58	12.5	152640	1908.0
β Vir	280308T06:22	-30	1.43	0.61	12.5	99216	1240.2
β Vir	280308T07:04	0	1.70	0.53	12.5	99216	1240.2
Arcturus	280308T08:06	0	1.61	0.59	12.5	99216	1240.2
Arcturus	280308T08:50	-30	1.88	0.84	12.5	99216	1240.2
36 Oph	170708T23:16	0	1.21	1.00	20.0	95040	1900.8
36 Oph	180708T00:17	30	1.07	1.00	20.0	95040	1900.8
del Pav	180708T01:26	0	1.60	0.90	16.0	119040	1904.6
del Pav	180708T02:24	30	1.46	0.83	16.0	119040	1904.6
Altair	180708T03:34	0	1.23	0.87	20.0	95040	1900.8
Altair	180708T04:30	30	1.20	0.72	20.0	95040	1900.8
ζ Tuc	180708T05:38	0	1.60	0.75	20.0	59400	1188.0
ζ Tuc	180708T06:14	30	1.50	0.64	20.0	59400	1188.0
τ Cet	180708T07:03	0	1.43	0.64	20.0	95040	1900.8
τ Cet	180708T07:58	30	1.19	0.66	20.0	95040	1900.8
ϵ Eri	180708T09:06	0	1.46	-	20.0	59400	1188.0
ϵ Eri	180708T09:41	30	1.29	1.50	20.0	59400	1188.0
ϵ Ind ³	030707T10:03	0	1.31	0.76	20.0	-	631.1
ϵ Ind ³	030707T10:35	55	1.38	0.61	20.0	-	631.1

¹number of observations with given Detector Integration Time (DIT)

²Int. time = # of beams * DIT; ³ standard VISIR observation

Calibrators March : HD 111067, HD 173780, HD 61935, HD 79554, HD 83425

Calibrators July : HD 220009, HD 2261, HD 2436, HD 133774, HD 161096

four chop and nod positions). The beams are in the following cut out, aligned and averaged to produce a final image.

3.2.3 Analysis and Results

After the preliminary data reduction the IDL/ATV routine was used to obtain photometry for the objects. The measured fluxes of the T-ReCS and VISIR targets are listed in Table 3.7.

To enhance the visibility of faint sources we used the approach of angular differential imaging (ADI). Each of the targets was observed at two instrument position angles (PA) separated by 20° and 30° , respectively. The corresponding data sets at the different position angles are subtracted to improve the visibility at angular separations close to the star. Furthermore, by rotating one of the data sets to the exact same position angle as the second data set a higher total integration time can be reached by averaging the two data sets (in the following always referred to as the averaged data, frame or image). To compare the sensitivity of the different data sets we calculated the radial dependent standard deviation.

Table 3.7: Measured fluxes from the GEMINI/ T-ReCS observations at $11.7\mu\text{m}$ and the VLT/VISIR at $8.6\mu\text{m}$.

Target	$11.7\mu\text{m}$	$8.6\mu\text{m}^1$	$8.6\mu\text{m}^2$
ϵ Ind	4.01 (0.03)	7.7 (0.1)	7.7 (0.1)
ϵ Eri	6.75 (0.01)	11.9 (0.2)	10.4 (0.2)
β Hyi	8.95 (0.04)	-	-
β Vir	-	6.2 (0.2)	6.5 (0.2)
β Leo	-	8.9 (0.3)	8.8 (0.3)
τ Cet	-	11.7 (0.2)	11.9 (0.2)
ζ Tuc	-	1.5 (0.1)	1.9 (0.1)
Sirius	-	-	-
Altair	-	44.0 (0.8)	44.3 (0.8)
Procyon	-	-	-
36 Oph	-	2.0 (0.1)	2.1 (0.1)
del Pav	-	6.4 (0.1)	9.3 (0.1)
Arcturus	-	-	-

¹first measurement, usually at P.A. 0°

²second measurement, usually at P.A. 30°

GEMINI : The reduced images of the three T-ReCS targets, ϵ Eri, ϵ Ind and β Hyi are presented in Figure 3.2. The Figure also displays the ADI subtracted and the averaged image. The small source seen in the ADI subtracted images of β Hyi is a background star introduced by the chopping of the telescope, as can be conclude from the fact that it appears only as negative source at PA = 20° . No other faint source was detected in any of the images.

The radial dependent sensitivity limits of the different data sets were calculated from the standard deviation and are shown in Figures 3.5, 3.3 and 3.4. Both for ϵ Ind and β Hyi two data sets at position angles 0° and 340° and 20° , respectively, were obtained. Thus in Figures

Figure 3.2: Reduced images of the T-ReCS targets. From top to bottom : image at PA = 0°, rotated by 20°, average and the ADI subtracted.

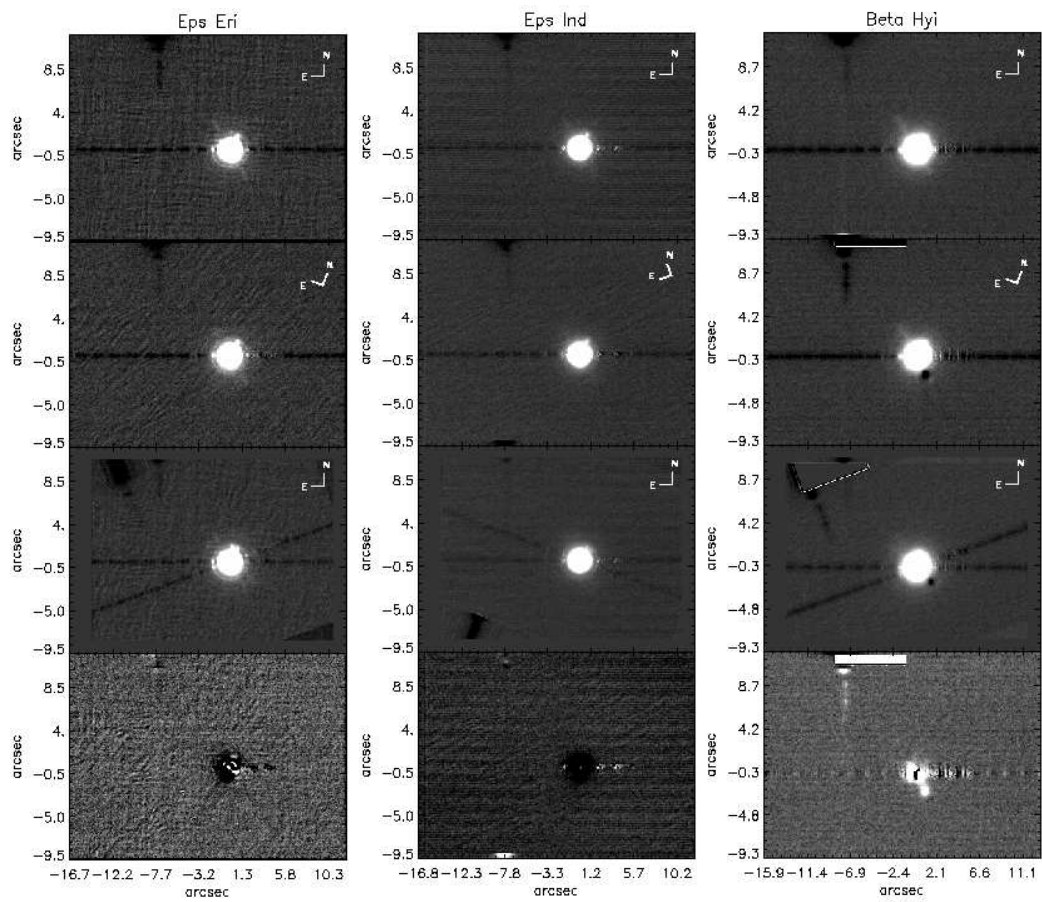


Figure 3.3: 3σ detection limits of the GEMINI/T-ReCS observations of ϵ Ind. The plot on the left shows the comparison between the detection limits of the two data sets. Too each data set belong two observations at PA = 0° and 340° . The graph on the right compares the detection limits of the average of the two observations at PA = 0° and 340° , respectively, too the detection limits obtained from the difference image and the averaged image of the former.

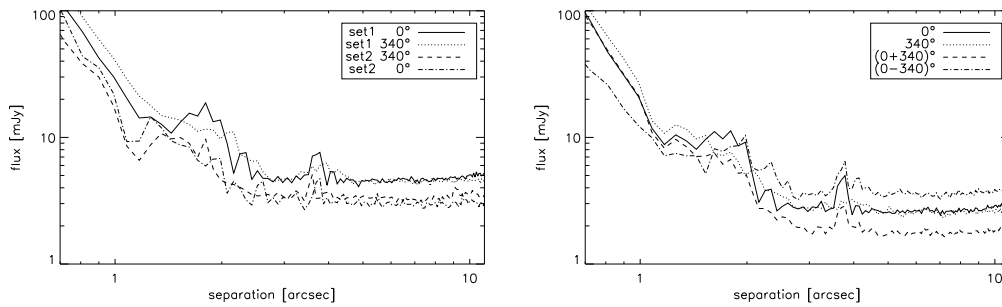
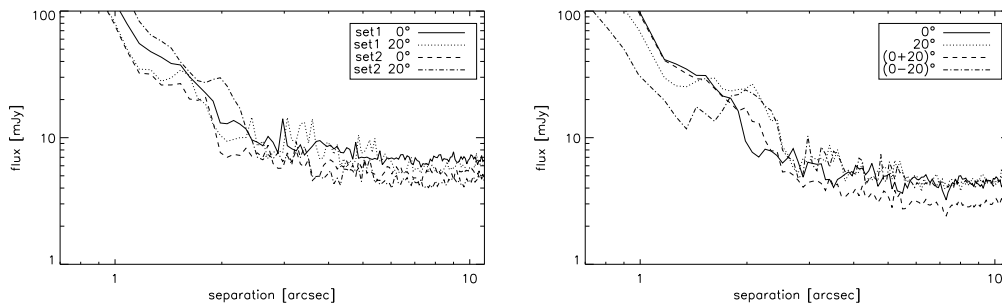


Figure 3.4: 3σ detection limits of the GEMINI/T-ReCS observations of β Hyi. Same as for ϵ Ind only that the position angles are PA = 0° and 20° .



3.3 and 3.4 the detection limits of each set of observations as well as the detection limits of the averaged data sets are presented. Taking the sensitivity limits as foundation one can roughly estimate what kind of companions, in terms of mass, could have been detected if present. E.g., in case of ϵ Eri the minimum detection limit for the T-ReCS observations (Si5 filter) is between 2 and 3 mJy. This limit in combination with the age and the distance of ϵ Eri (from Table 3.4), can be compared to the theoretical predictions listed in Tables 3.1 and 3.2. Considering the distance modulus, this simple comparison yields values of 7.3 - 10.5 M_J as minimum masses. At the distance of ϵ Eri (3.2 pc) this signifies that we are able to detect planetary mass objects at separations of 7 to 32 AU. Still, at $1''$ - the maximum separation of the planetary companion ϵ Eri b from the primary - our sensitivity limits are ten times higher, making the detection of the companion unfeasible.

VISIR : The principle idea behind the 'burst' mode is to store every single integration to be able to correct for displacements of the PSF and to average only the highest quality frames. Thus for each target at both position angles we calculated final images averaging only the best 10%, 30%, 50%, 70% and 100% of all single integrations. The development of sensitivity limit from 10%, over 50% to 100% of the total integration time is displayed for ϵ Eri in

Figure 3.5: 3σ detection limits of the GEMINI/T-ReCS observations of ϵ Eri. Compared are the detection limits from the data taken at PA = 0° and 20° as well as the detection limit obtained from the difference image and the averaged image of the two position angles.

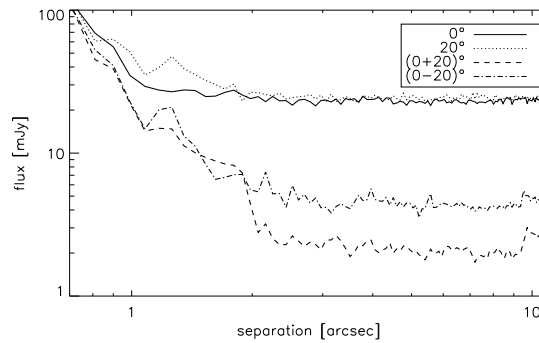
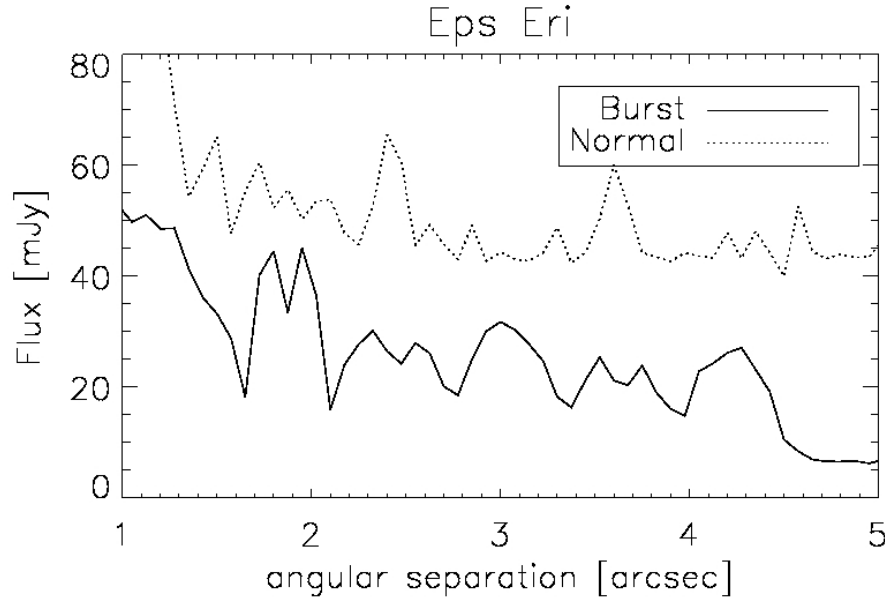


Figure 3.7 exemplary. Identical graphs for the remaining targets can be found in Appendix A. In all cases the development of the sensitivity limits at PA = 0° and 30° is presented first. The third graph finally shows the comparison of the 100% sensitivity limit at the two position angles with the sensitivity limit of the ADI subtracted and the averaged image.

Identically as for the T-ReCS observations the sensitivity limit can be translated into a minimum detectable mass. Again, for ϵ Eri the sensitivity limit reached during the observations is between 5 and 10 mJy, which roughly translates to 15.7 to 31.4 M_J . Despite a longer integration time the sensitivity limit of the VISIR observation is somewhat higher than for the T-ReCS observations, which is due to the smaller pass-band of the VISIR PAH1 filter.

But, when comparing standard VISIR observations to observations using the 'Burst' mode, the advantage of the 'Burst' mode becomes clear. Figure 3.6 shows both the detection limits of ϵ Eri, which was observed in 'Burst' mode, and ϵ Ind, taken with the standard observation mode of VISIR. The later one had to be scaled to the flux and to the integration time of the observations of ϵ Eri, before the comparison.

Figure 3.6: Comparison of the sensitivity limit reached with standard VISIR and 'Burst' mode observation.

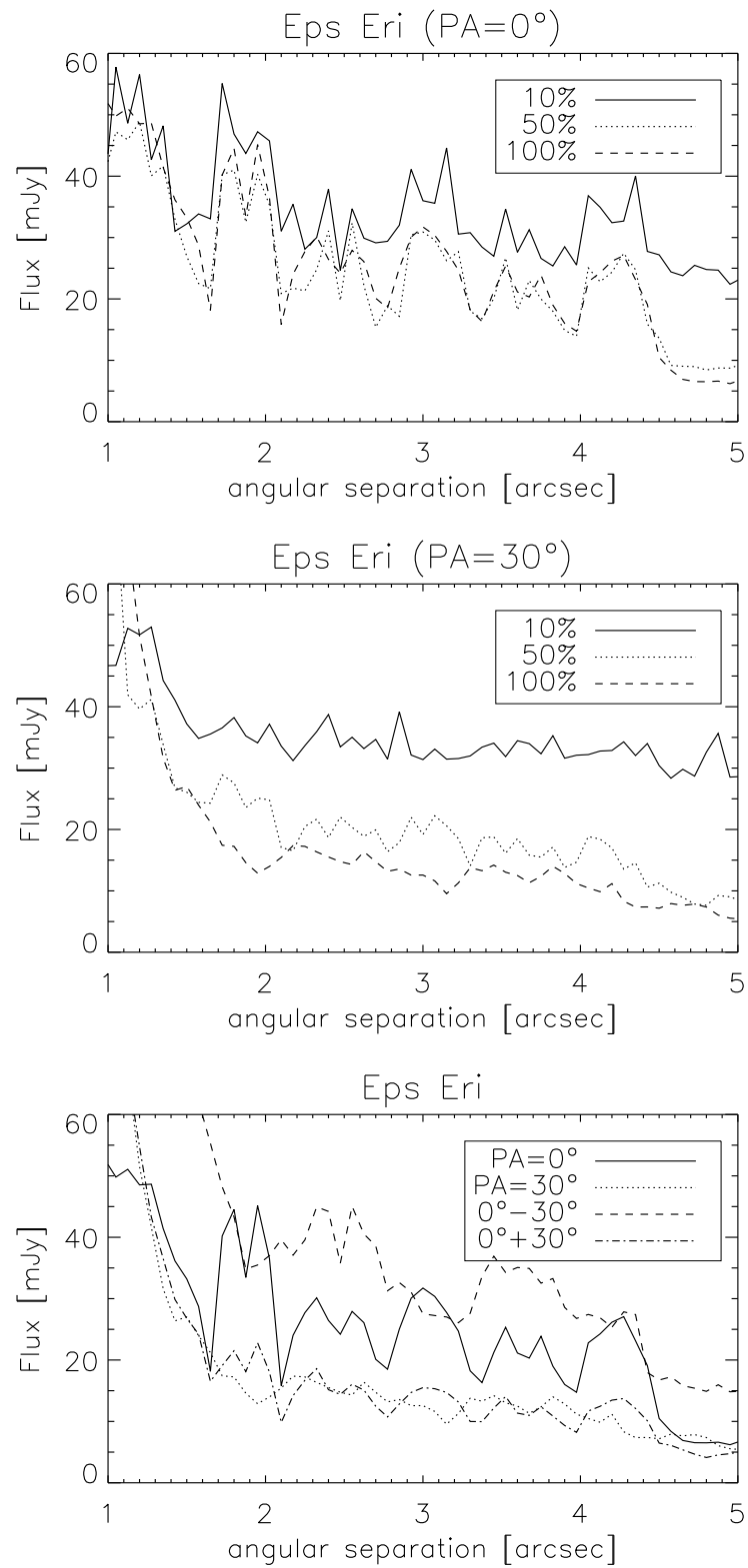


3.3 Conclusion

We conducted a survey of thirteen optical and near-infrared bright, near-by stars using the mid-infrared facilities T-ReCS at the GEMINI/South and VISIR at the VLT, aiming at the detection of low-mass and planetary companions at separation of a few AU from the primary. While none such companion was detected, we provide upper limits for all observations.

With T-ReCS we observed three of the targets (ϵ Ind, ϵ Eri and β Hvi) using a broad band filter centered at $11.7\mu\text{m}$. The observations reach sensitivity limits down to 2-3 mJy (3σ) at separations larger than $2''$, which translates to 6.4 to 14.9 AU at the distances of the targets. The remaining ten targets and ϵ Eri were observed with VISIR, employing its newly commissioned 'Burst' mode, in the narrow band filter at $8.6\mu\text{m}$. In the best cases, sensitivity limits in the order of a few mJy were reached, e.g., 5 mJy (5σ) at separations larger than $2''$ for β Leo (Figure A.2) and β Vir (Figure A.3).

But even for the youngest and closest stars of our target sample a sensitivity limit of 5 mJy would not allow the detection of objects with masses less than $15M_J$. Thus, the detection space of the VISIR observations is limited to brown dwarf companions a priori.

Figure 3.7: 5σ detection limit of the VISIR 'burst' mode observation in July 2008.

Chapter 4

Polarimetric Differential Imaging of Circumstellar Discs

4.1 Principles of Polarimetric Differential Imaging

The first AO system at an 8 m class telescope equipped with polarimetric differential imaging capabilities was the HoKupa'a at Gemini North. A warm Wollaston prism was inserted between the AO instrument and the science camera to split the light into two beams, an ordinary and an extra-ordinary one. The two beams were then projected simultaneously on the detector. By subtracting the two beams the non-polarised light, mainly light coming from the central star and the speckle noise is removed. Only the polarised light, e.g.; the scattered light from the disc, remains after the subtraction.

4.1.1 Polarimetric Differential Imaging

To obtain an image of the polarised intensity (PI) of an object two data sets taken at polarisation angles of 0° and 45° or 90° and 135° , respectively, are necessary. However to reduce systematic errors, such as the instrumental polarisation, it is advisable to obtain data sets at all four polarisation angles. Each data set contains two simultaneously acquired images of the source. The ordinary (I_o) and extra-ordinary (I_e) beams have a phase difference of 90° . By subtracting the two orthogonally polarised beams the Stokes Q and U vectors are obtained.

$$0: \quad Q^0 = I_o - I_e \quad (4.1)$$

$$45: \quad U^{45} = I_o - I_e \quad (4.2)$$

$$90: \quad -Q^{90} = I_o - I_e \quad (4.3)$$

$$135: \quad -U^{135} = I_o - I_e \quad (4.4)$$

To correct for instrumental effects the Stokes vectors of redundant data sets are then combined.

$$Q = \frac{Q^0 - (-Q^{90})}{2} \quad (4.5)$$

$$U = \frac{U^{45} - (-U^{135})}{2} \quad (4.6)$$

Now, the polarised intensity (PI) can be calculated from the combined Stokes vectors.

$$PI = \sqrt{\frac{Q^2 + U^2}{2}} \quad (4.7)$$

Finally, the absolute polarisation P can be calculated:

$$P = \sqrt{\frac{(\frac{Q}{I_Q})^2 + (\frac{U}{I_U})^2}{2}} \quad (4.8)$$

Where I_Q and I_U are the averaged intensities:

$$I_Q = \frac{I_o^0 + I_e^0 + I_o^{90} + I_e^{90}}{4} \quad (4.9)$$

$$I_U = \frac{I_o^{45} + I_e^{45} + I_o^{135} + I_e^{135}}{4} \quad (4.10)$$

From the Stokes Q and U vectors the position angle of the polarisation can be calculated:

$$\theta = 0.5 * \arctan\left(\frac{U}{Q}\right) \quad (4.11)$$

During the whole reduction process special care must be given to the subtractions of the ordinary and extraordinary beams, as well as to the co addition of single exposures and Stoke vectors. Before addition or subtraction the respective images must be aligned with sub-pixel accuracy to avoid artificial polarimetric features and/or a destruction of any polarimetric signal.

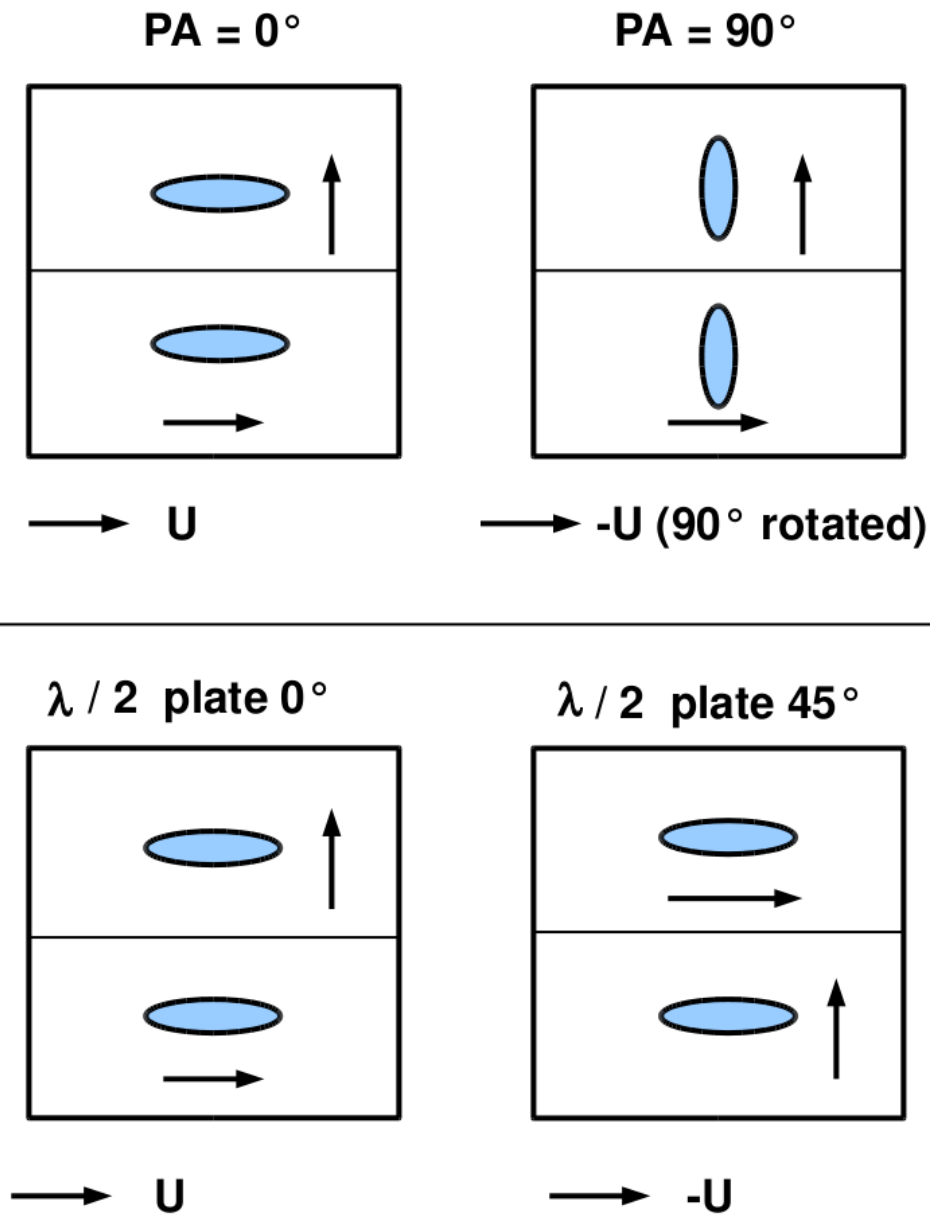
4.1.2 Differential Polarimetry with NACO

The NACO¹ system is a adaptive optics assisted, near-infrared instrument attached to the one of the Nasmyth foci of the fourth unit telescope (UT4, Yepun) at the Very Large Telescope (VLT). The abbreviation NACO consist of two acronyms: NAOS (Nasmyth Adaptive Optics System), which is the adaptive optic system feeding the near-infrared camera CONICA (Near-Infrared Imager and Spectrograph). The camera is equipped with a detector of 1024 × 1024 pixel, and provides imaging, spectroscopy, coronagraphy, differential imaging (SDI) and polarimetric imaging in the range from 1-5 μm.

In order to conduct polarimetric imaging two cold Wollaston prism and a λ/2 retarder plate are available. Thus NACO polarimetric differential imaging can either be done by rotating

¹NACO homepage : <http://www.eso.org/sci/facilities/paranal/instruments/naco/>

Figure 4.1: The sketch is illustrating the two possible ways of polarimetric differential imaging with NACO. Thereby the ellipse symbolises the astronomical object and its orientation on the detector, while the arrows indicate the orientation of the polarisation. The upper panel refers to the case when the telescope is rotate, while the lower panel is illustrating the rotation of the half-wave plate. Note that in the case of telescope rotation the orientation of the source in the redundant data sets is rotated by 90° .



the instrument or by rotating the $\lambda/2$ retarder plate to obtain data sets at different polarisation angles. The principles of the two approaches are illustrated in Figure 4.1. In both cases the Wollaston prism splits the incoming light into two orthogonal beams, an ordinary and an extra-ordinary. To avoid overlaying of the beams a mask, consisting of alternating opaque and transmitting strips, is inserted into the focal plane. As usual, to measure the Stokes vectors a second set of observations, with the Wollaston prism rotated by 45 degrees is needed. This is achieved by either rotating the entire instrument or, in case the half-wave plate is used, by rotating it by 22.5° .

4.2 Project Description

In 2004 Apai et al. (2004) presented the first high-contrast observation carried out with the newly implemented PDI mode of NACO. The observations targeted TW Hya, a classical T Tauri star, and were able to trace the polarised disc emission from $0.1''$ to $1.4''$. The observations showed impressively, that the technique is capable of imaging circumstellar material at very high resolutions.

Following the example of Apai et al. (2004) a sample of twelve young stars was observed with the PDI mode of NACO. Intrinsically the complete data set is a combination of two separately started project. While the aim is the same, to study the properties of the discs in polarised light, the two data sets vary, inconsequentially, in the mode of execution. This difference has no influence on the results, but has to be considered during the reduction of the data and will be mentioned and explained in the corresponding section.

4.2.1 Target sample

The 2004 targets were selected from previous ISAAC observations of objects in the ρ Oph star forming region, while the targets from 2006 were selected because they are young, show prominent near-ir excess and the existence of a disc had already been demonstrated. The complete sample is presented in Table 4.1, while only some of the targets are discussed in more detail below.

ρ Ophichi star forming region : is one of the closest star-forming regions. The distance is estimated to be about 130pc and there are over 300 members associated with the main cloud L1688. Star formation is ongoing in the dense cores of L1688 with a median age for young stellar objects of 0.3Myr. Spectroscopic studies have characterized a population of 100 YSOs that lie at the periphery of the L1688 cloud with a median age of 2Myr (Bouvier & Appenzeller (1992), Martin et al. (1998), Wilking et al. (2005)). Nevertheless, there are indications that the formation of this surface population of stars surrounding the L1688 core was contemporaneous with low mass stars in the Upper Scorpius subgroup, with a median age for the formation of 2-5Myr. For a recent review of the ρ Ophichi star forming region see Wilking et al. (2008).

Chameleon star forming region : the southern constellation of Chamaeleon is situated at 160-180 pc from the Sun (Whittet et al., 1997). It is segmented in three main clouds (Cha I, II, and III), each with an angular sizes of a few square degrees. Most of the star formation is occurring in Cha I, which currently contains 237 known members. Comparisons of the H-R

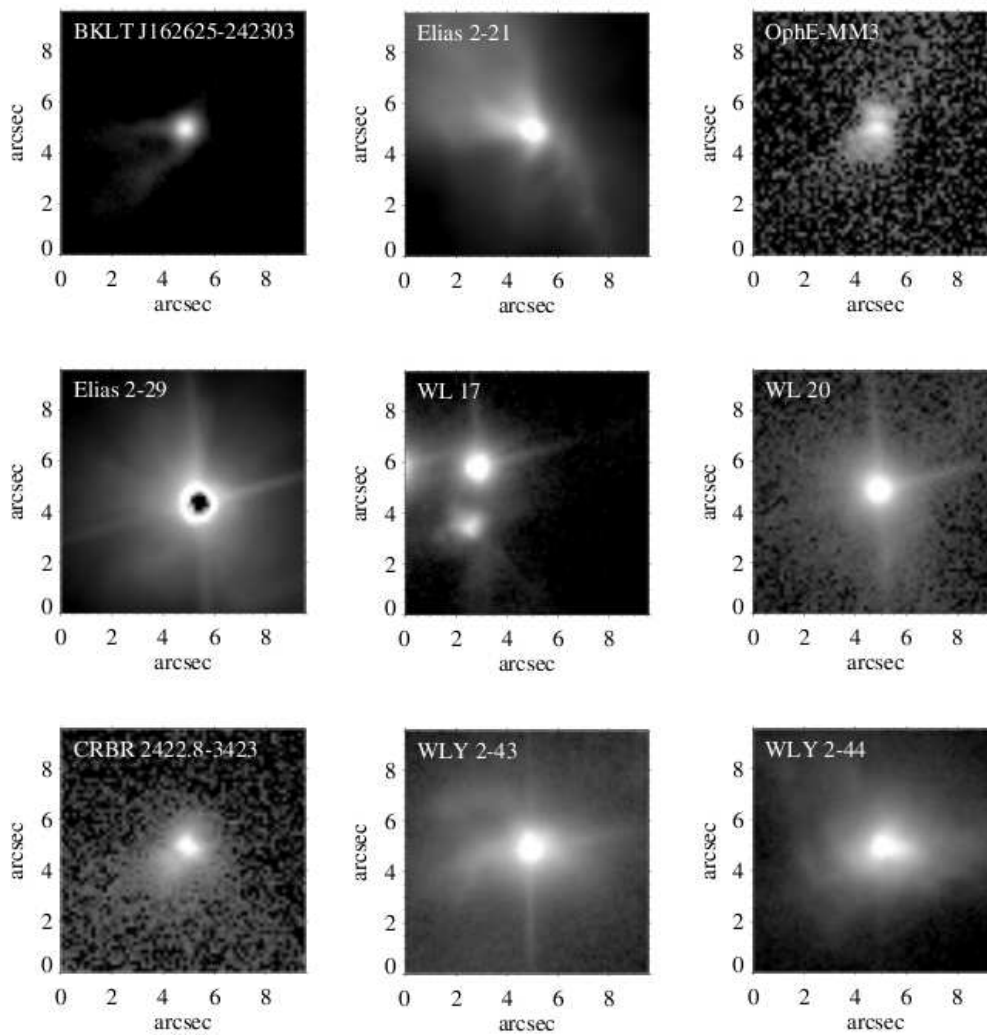
Figure 4.2: ISAAC images of the ρ Ophiuchi targets.

Table 4.1: NACO PDI targets

Object	π	SpT	age	H	K_s	note
	[mas]		[Myr]	[mag]	[mag]	
BKLT J1626-2423	~ 8		0.3 – 5	14.66	12.82	ρ Oph
CRBR 2422.8-3423	~ 8		0.3 – 5			ρ Oph; CI I ¹
Elias 2-21	~ 8		0.3 – 5	10.83	12.85	ρ Oph; CI I
WL 17	~ 8		0.3 – 5	14.29	10.97	ρ Oph; CI II
WL 20	~ 8		0.3 – 5	11.26	9.59	ρ Oph; CI II
WLY 2-43	~ 8	K 5	0.3 – 5	13.52	9.75	ρ Oph; CI I
WLY 2-44	~ 8	K 8	0.3 – 5	13.68	9.65	ρ Oph; CI I
HD 109573	13.74 ⁴	A 0	8	5.79	5.77	
CR Cha	5.97 ⁴	K 2	~ 2	7.82	7.31	Cha I; TT ²
DI Cha	4.49 ⁴	G 1	~ 2	6.94	6.22	Cha I; TT
HD 97048	6.31 ⁴	A 0	2 – 3	6.67	5.94	Cha I; HA
HD 100546	10.32 ⁴	B 9	≥ 10	5.96	5.42	HA ³

¹ classified as Class I or II by Bontemps et al. (2001) ; ² T-Tauri type star;

³ Herbig Ae/Be Star; ⁴ revised parallaxes by van Leeuwen (2007)

diagram for Cha I to evolutionary models by Chabrier and Baraffe assign Cha I a median age of 2 Myr. The disk fraction in Cha I is roughly constant at 50% from 0.01 to 0.3 M_{\odot} and increases to 65% at higher masses. For a more comprehensive discussion of the Chameleon star forming region see the review by Luhman (2008).

HD 109573 : also known as HR 4796A, is a young (8 Myr; Stauffer et al. (1995)) main sequence star with a circumstellar disc (Jayawardhana et al. (1998), Koerner et al. (1998), Schneider et al. (1999), Schneider et al. (2009)). The existence of a dusty debris disc was first inferred by Jura (1991) from its thermal infrared signature. In the following mid-infrared observations by Jayawardhana et al. (1998) and Koerner et al. (1998) indicated dust emission at separations of 60 - 87 AU (revised distance). The first observations to directly image the dust were conducted by Schneider et al. (1999) using the NICMOS instrument of the Hubble Space Telescope (see Figure 4.3). The coronagraphic observations revealed a ring with a radius of 76 AU (1.05 arcsec) and a width of 18.5 AU. The images also suggested a brightness asymmetry of the disc, similar to the one seen in the mid-infrared images taken by Telesco et al. (2000).

The dust ring scatters starlight at visible to near-IR wavelengths and emits thermally in the infrared. The spatially resolved scattered light and thermal emission are assumed to be caused by grains with radii on the order of a few μm . But the presents of larger grains (a few tens of μm) is required to explain the unresolved emission at infrared and sub-mm wavelengths (see Debes et al. (2008) and references therein).

HD 97048 : has been classified as a HAe star of group I with evidence of a flared disk according to the classification by Meeus et al. (2001), since its SED is rising in the IR (Acke & van den Ancker, 2004). Spectroscopic observations revealed the presence of strong PAH (Polycyclic Aromatic Hydrocarbon) features at 3.3, 6.2, 7.7, 8.6 and 11.3 μm and nano-

Figure 4.3: Comparison of the NICMOS image of HD 109573 with the STIS image (Schneider et al., 2009). The red dot marks the center of the ring while the yellow star marks the location of the star. Both images show a decrement in ring brightness at P.A. $\sim 230^\circ$.

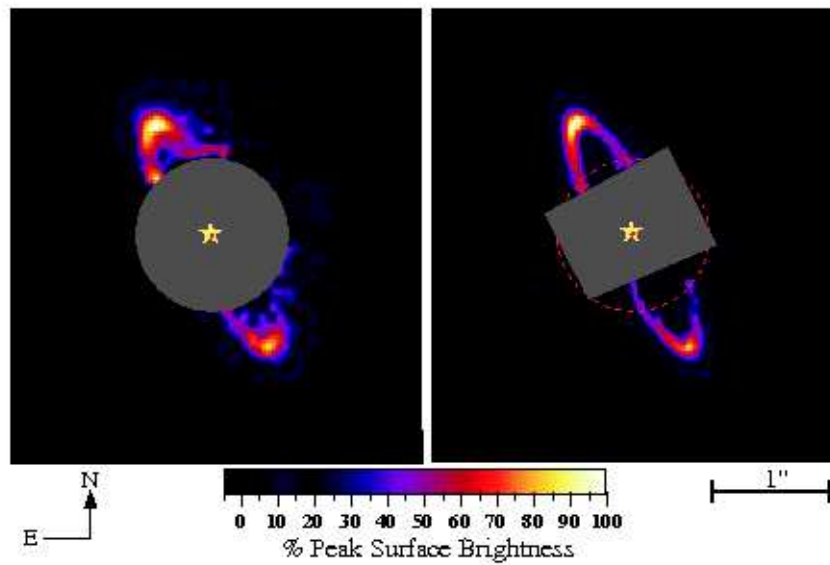


Figure 4.4: From Doucet et al. (2007) Displayed are VISIR observations of HD 97048 (left) and a PSF reference star (right). Both images were obtained in the PAH2 filter (centered at $11.3 \mu\text{m}$) and normalized to see the extension. The object is more extended than the reference with an east/west asymmetry in the emission.

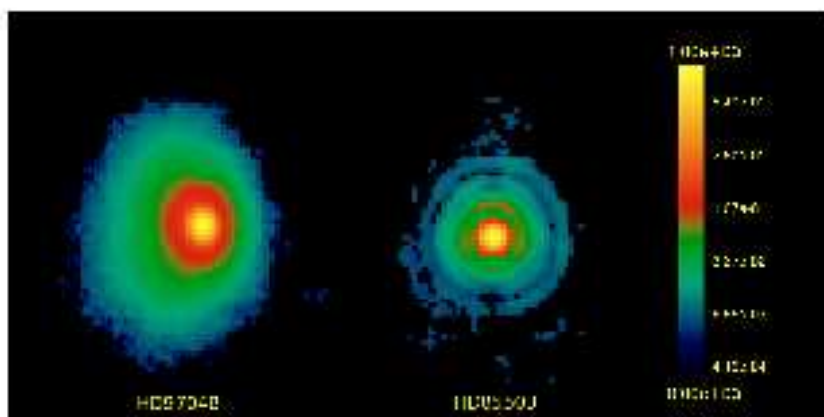
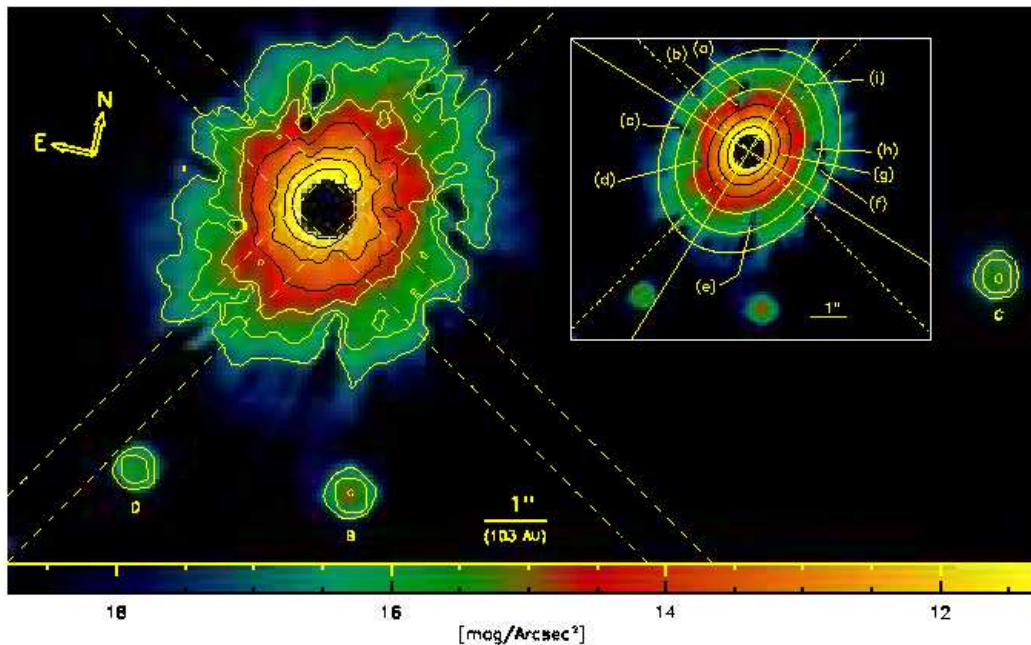


Figure 4.5: HST / NICMOS observations of the disc around HD 100546 from Augereau et al. (2001).



diamond features in the 3.4-3.5 μm region (Siebenmorgen et al. (2000), Van Kerckhoven et al. (2002)), but no silicate emission band at 10 μm . More recent observations with VISIR at the VLT showed extended emission of PAHs at the surface of a flared disc (Lagage et al., 2006). The disc itself, shown in Figure 4.4 is inclined to the line of sight by $42.8^{+0.8}_{-2.5}$ °.

HD 97048 is the only Herbig star for which the flaring of the disc has been observed by direct imaging, with a flaring index of 1.26 ± 0.05 . The measured flaring index is in good agreement with hydrostatic flared disk models (Lagage et al. (2006), Doucet et al. (2007)). This geometry implies that a large amount of gas should be present to support the flaring structure and that the disk is at an early stage of evolution.

From the comparison to evolutionary tracks an age of the order of 3 Myr has been estimated (Martin-Zaïdi et al., 2007).

HD 100546 : is an isolated young main-sequence (Herbig Be) star with an estimated age of 10 Myr (van den Ancker et al., 1998). The circumstellar disc around HD 100546 was first resolved in the near-infrared using the ADONIS instrument mounted on the 3.6m telescope at La Silla (Pantin et al., 2000). The coronagraphic observations revealed circumstellar material at angular separations from 0.4'' to 2'', consistent with the presence of a disc with an inclination of $50^\circ \pm 5^\circ$ from edge-on. NICMOS coronagraphic observations (Figure 4.5) conducted by Augereau et al. (2001) detected scattered light at angular distances from 0.5'' to 3.8'' from the star and a significant azimuthal asymmetry in the disc. High resolution images taken with the Space Telescope Imaging Spectrograph (STIS) revealed a complex circumstellar structure surrounded by an envelope of material up to 10'' from the star (Grady et al., 2001). The images showed bright and dark lanes in the disc, reminiscent of spiral structure.

Nulling interferometric observations at $10\ \mu\text{m}$ led to the determination of a disc radius of 30 AU and suggested the presence of an inner hole (Liu et al., 2003). Evidence for a hole close to the star has also emerged from spectroscopic data. STIS observation in the ultraviolet evince a deficit of molecular hydrogen close to the star, which the authors interpret as a central gas and dust cavity with a radius of 13 AU (Grady et al., 2005). Also Acke & van den Ancker (2006) infer the presence of a 4.3 AU wide gap 6.5 AU away from the star from their study of the $6300\ \text{\AA}$ line of [OI].

HD 100546's mid-infrared spectrum shows strong emission in crystalline silicates similar to the spectrum of Comet C/1995 O1 (Hale- Bopp) (Malfait et al., 1998). Amorphous silicate emission bands are visible at 10 and $18\ \mu\text{m}$ as well as strong PAH bands at 3.3, 6.2, 7.7, 8.6 and $11.2\ \mu\text{m}$ (Meeus et al., 2001). Models of the circumstellar material suggest a relatively large fraction of small ($0.1\ \mu\text{m}$) forsterite and large ($1.5\ \mu\text{m}$) enstatite grains (Malfait et al. (1998); van Boekel et al. (2005)). According to models by Bouwman et al. (2003), the large amorphous silicate grains and small forsterite grains appear to have different temperatures, although they overlap in radial distance from the star.

“All these spectroscopic models indicate a highly evolved disk both in terms of particle size and crystalline fraction. ... The lack of detectable gas, the presence of large particles, and the evidence for an inner hole suggest that HD 100546 is an evolved pre-main-sequence star, a 'transitional' disk perhaps ... (Ardila et al., 2007).”

4.2.2 Observations and Reduction

Observations were carried out using the NACO instrument at the VLT in Visitor mode during four nights in April 2004 and four nights in April 2006. The PDI observations in 2004 were conducted before the implementation of the $\lambda/2$ wave plate, requiring the rotation of the instrument by 45° to obtain Stokes U and Q vectors and, hence, the polarisation. Additionally for most of the targets redundant data sets (rotated by 90° from the initial position) were obtained to reduce the effects of the instrument polarisation. By April 2006 NACO had been equipped with a rotatable $\lambda/2$ wave plate, thus to obtain Stokes U and Q vectors a rotation of the $\lambda/2$ wave plate by 22.5° is sufficient. Redundant data sets, rotating the $\lambda/2$ wave plate by 45° from the initial position, were taken for all targets from 2006. All Observations were conducted in H, Ks, NB 1.64, IB 2.18, IB 2.21 and/or L' with a pixel scale of $0.0271''$ per pixel, except for the observations of HD 109573, which were done with a pixel scale of $0.01326''$ per pixel. The central wavelength and the filter band widths are listed in Table 4.2.

Table 4.2: NACO filter bands.

Filter	λ_C [μm]	Δ [μm]
H	1.66	0.33
Ks	2.18	0.35
L'	3.8	0.62
NB 1.64	1.644	0.018
IB 2.18	2.18	0.06
IB 2.21	2.21	0.06

Considering the highly variable sky in the infrared the observations were taken using a jitter/dither pattern to allow the subtraction the sky background. Different integration times

Table 4.3: Observing log of the PDI observations in 2004.

Target	UT date	Filter	DIT	Int. time	Air-	see-	P.A.
	ddmmyy		[s]	[s]	mass	ing	[°]
BKLT J1626-2423	060404	Ks	150	600.	1.04	0.89	0
CRBR 2422-3423	060404	Ks	150	300.	1.10	0.51	0
	060404	Ks	180	540.	1.13	0.50	0
Elias 2-21	030404	Ks	1.79	26.9	1.06	0.80	0, 45, 90, 135
	030404	Ks	20	180.	1.06	0.79	0, 45, 90, 135
	030404	Ks	60	360.	1.05	0.76	0, 45, 90, 135
	030404	Ks	120	360.	1.04	0.79	0, 45, 90, 135
	060404	H	30	180.	1.10	0.82	0, 45, 90, 135
	060404	H	180	540.	1.10	0.80	0, 45, 90, 135
	030404	IB 2.21	200	800.	1.05	0.75	0
	060404	L'	0.17	91.8	1.01	0.77	0, 45, 90, 135
HD 109573 ¹	070404	H	3	30.	1.64	0.65	0, 45
	070404	H	10	120.	1.69	0.60	0, 45
	070404	H	60	120.	1.70	0.60	0, 45
	070404	IB 2.21	20	200.	1.67	0.54	0, 45
	070404	IB 2.21	50	200.	1.69	0.65	0, 45
WL 17	050404	Ks	12	72.	1.04	0.51	0, 45, 90, 135
	050404	Ks	60	360.	1.04	0.50	0, 45, 90, 135
	050404	Ks	120	360.	1.04	0.49	0, 45, 90, 135
	050404	IB 2.21	180	360.	1.13	0.53	0, 45, 90, 135
WL 20	040404	Ks	12	36.	1.28	0.47	0, 45
	040404	Ks	25	225.	1.27	0.48	0, 45
	040404	Ks	120	360.	1.25	0.52	0, 45
	040404	Ks	240	720.	1.20	0.49	0, 45
WLY 2-43	050404	Ks	12	72.	1.24	0.40	0, 45, 90, 135
	050404	Ks	200	600.	1.22	0.40	0, 45, 90, 135
	050404	IB 2.21	100	200.	1.07	0.36	0, 45, 90, 135
WLY 2-44	040404	Ks	60	360.	1.04	0.55	0, 45, 90, 135
	040404	Ks	200	600.	1.04	0.53	0, 45, 90, 135

¹ H and IB 2.21 observations with additional neutral density filter

were chosen to trace the polarisation pattern at different angular separations, since the central part of the stellar point spread function (PSF) is likely to be saturated for longer integration times. Targets, filters and corresponding integration times for the observations in 2004 and 2006 are listed in Table 4.3 and Table 4.4, respectively.

Table 4.4: Observing log of the PDI observations in 2006.

Target	UT date	Filter	DIT	Int. time	Air-	see-	P.A.
	ddmmyy		[s]	[s]	mass	ing	[°]
CrCha	100406	H	0.35	357.	1.64	1.10	180
	100406	H	1.0	360.	1.74	1.01	0
	100406	Ks	0.5	360.	1.67	0.83	180
	100406	Ks	1.2	360.	1.66	0.89	0
DiCha	090406	H	0.5	360.	1.68	0.82	0.
	090406	Ks	0.5	240.	1.66	0.94	0.
	090406	NB 1.64	5.	400.	1.67	0.79	0.
	090406	IB 2.18	1.3	468.	1.71	1.02	0.
HD 97048	080406	H	0.35	357.	1.68	0.60	0.
	080406	Ks	0.35	238.	1.66	0.59	0.
	080406	NB 1.64	3.	900.	1.68	0.66	0.
HD 100546	070406	H	0.35	446.3	1.51	1.08	155.
	070406	Ks	0.35	386.8	1.43	1.02	65.
	070406	NB 1.64	3.0	300.	1.43	0.95	65.
	070406	IB 2.18	0.6	270.	1.44	0.98	65.

After subtracting the images of different dither positions to remove the sky-background, the frames were flat-fielded. Bad pixel replacement was accomplished by substituting the pixel by the mean of the surrounding pixel. Since the data obtained in 2004 still showed a large amount of hot pixel, a sigma filter was applied to smooth them. In order to calculate the Stokes U and Q vectors according to equations 4.1 to 4.4 the ordinary and extra-ordinary beams are cut out and the beams from all dither positions are averaged, after shifting them to a common center. The averaged ordinary and extra-ordinary beams are finally subtracted from each other, to obtain the Stokes vectors at each position angle. Before continuing with the reduction all Stokes vectors generated from the observation in 2004 must be rotated to a common position angle, since the rotation of the instrument does not only change the direction of the polarisation, but also the orientation of the source on the detector as illustrated in Figure 4.1. Then, the next step the Stokes vectors at redundant position angles are calculated according to equations 4.5 and 4.6, to reduce the effects of the instrument polarisation. From the averaged Stokes U and Q vectors the polarised intensity as well as the position angle of the polarisation are computed following equations 4.7 and 4.11, respectively. The position angle of the polarisation is needed to generate the polarisation maps, in which the polarisation pattern becomes apparent. Finally, the total intensity (I) is calculated by averaging I_U and I_Q (from equations 4.9 and 4.10). From the total intensity (I) and the polarised intensity (PI) the degree of polarisation ($P = PI/I$ in %) can be calculated, which facilitates the recognition of regions of higher polarisation.

Finally, there are some remaining remarks concerning specific targets or observations :

- BKL T J1626-2423 and CRBR 2422.8-3423 have only been observed at one position angle, rendering the calculation of the polarised intensity impossible.
- WL 20 appears doubled in the data taken at PA = 0°. Therefore the data set was disregarded and only the observations at PA = 45° have been reduced. Thus, for WL 20 the polarised intensity could not be computed.
- Despite short DIT's the in 2006 observed targets are saturated in the center. For Cr Cha, Di Cha and HD 97048 the region within a radius of 2 pixel (0.054") and for HD 100546 the region within a radius of 3 pixel (0.081") has been saturated.

4.2.3 Results

A first impression of the targets can be gained from the contour plots of the intensity (I) distribution of the targets (see Figure 4.6). HD 109573, Di Cha, Cr Cha, WLY 2-43, WL 17 and HD 100546 show no obvious extended structures. Their PSF's appear point like and no nebulosity's associated with the stars are visible in the intensity images. There are two sources, Elias 2-21 and WLY 2-44, which are associated with extended nebulosity. Elias 2-21 shows a bipolar flux distribution, i.e. two lobes of extended nebulosity. The large scale structure and the surrounding environment of the sources can be seen in Figure 4.2.

The polarisation vector patterns observed in the different filters are presented and discussed in the following section. Generally the patterns can be divided in categories based on their appearance. Centrosymmetric patterns are arranged in a circle or ellipse about the central illuminating source. The pattern is aligned, when the polarisation vectors are arranged in parallel lines, while a random pattern shows no apparent structure whatsoever, indicating that no polarisation is detected.

The measured polarisation for the 2006 targets is lower than for the targets of 2004, as can be seen from the degree of polarisation. The 2006 sources are generally older and have discs, which are in later stages of their evolution and hence, a lower amount of dust to scatter and polarise the light from the central source.

4.2.4 Individual targets

4.2.4.1 Compact objects

The objects Cr Cha, Di Cha, HD 97048, WLY 2-43 and HD 109579 all have point-like morphologies in both total and polarised flux. Last can be seen in the polarisation maps (like Figure 4.7), since the intensity of the polarised flux is layed under the polarisation vectors as contours.

- Di Cha : The polarisation maps of Di Cha in H, Ks and NB 1.64 are presented in Figure 4.7 in the left hand column. While the polarisation vectors in H and Ks show an aligned pattern, they are randomly arranged in NB 1.64. The orientation of the polarisation vectors in H is almost north to south, while the orientation in Ks is from north-west to south-east. Both observation have a low degree of polarisation with $P_H = 3-4\%$ and $P_{Ks} = 5-10\%$, while the background has a degree of polarisation around $\sim 2\%$.

Figure 4.6: Contour plots of the flux profile of nine of the PDI sources. North is up, east is left. Only HD 100546 is rotated by 65° north to the west.

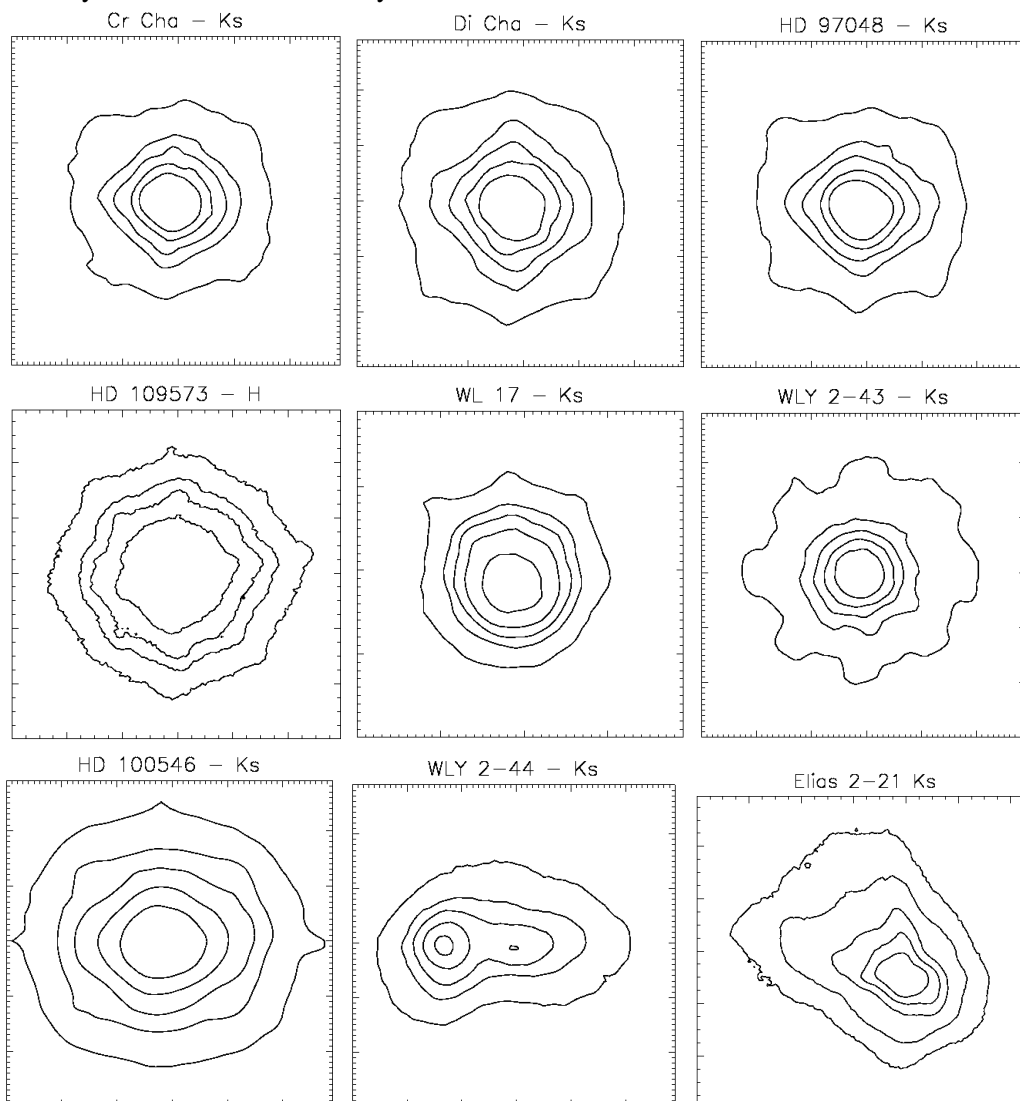


Figure 4.7: Polarisation maps for DI Cha (left) and HD 97048 (right). North is up, east is left.

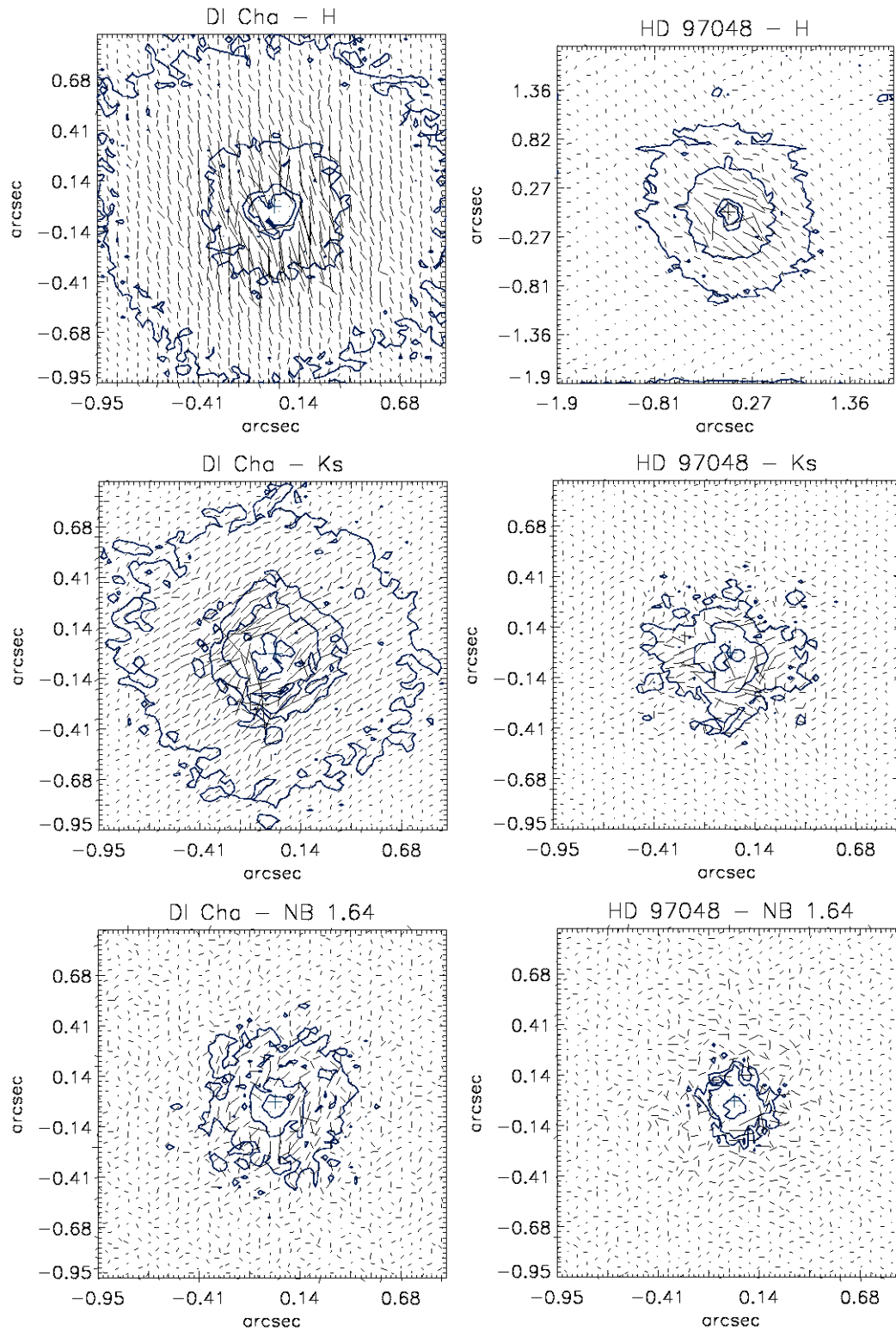
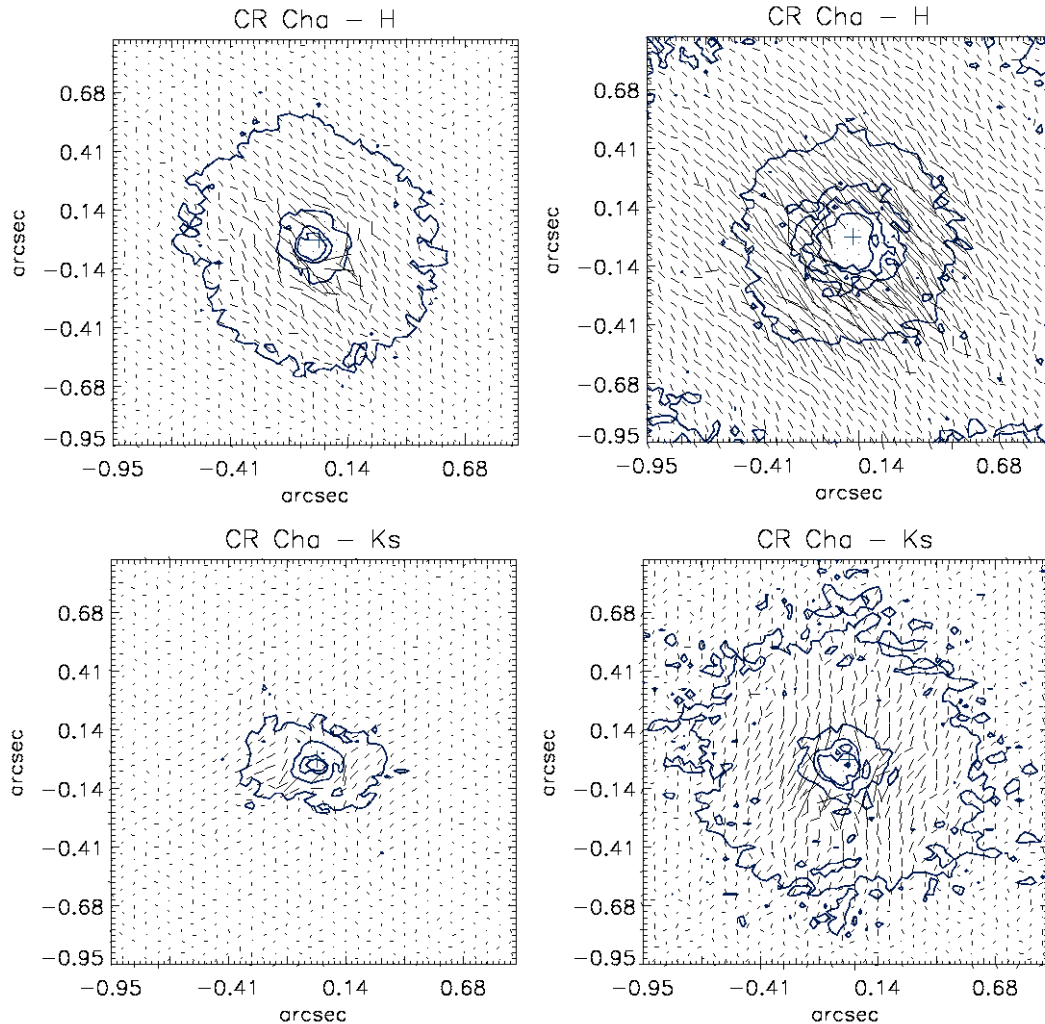
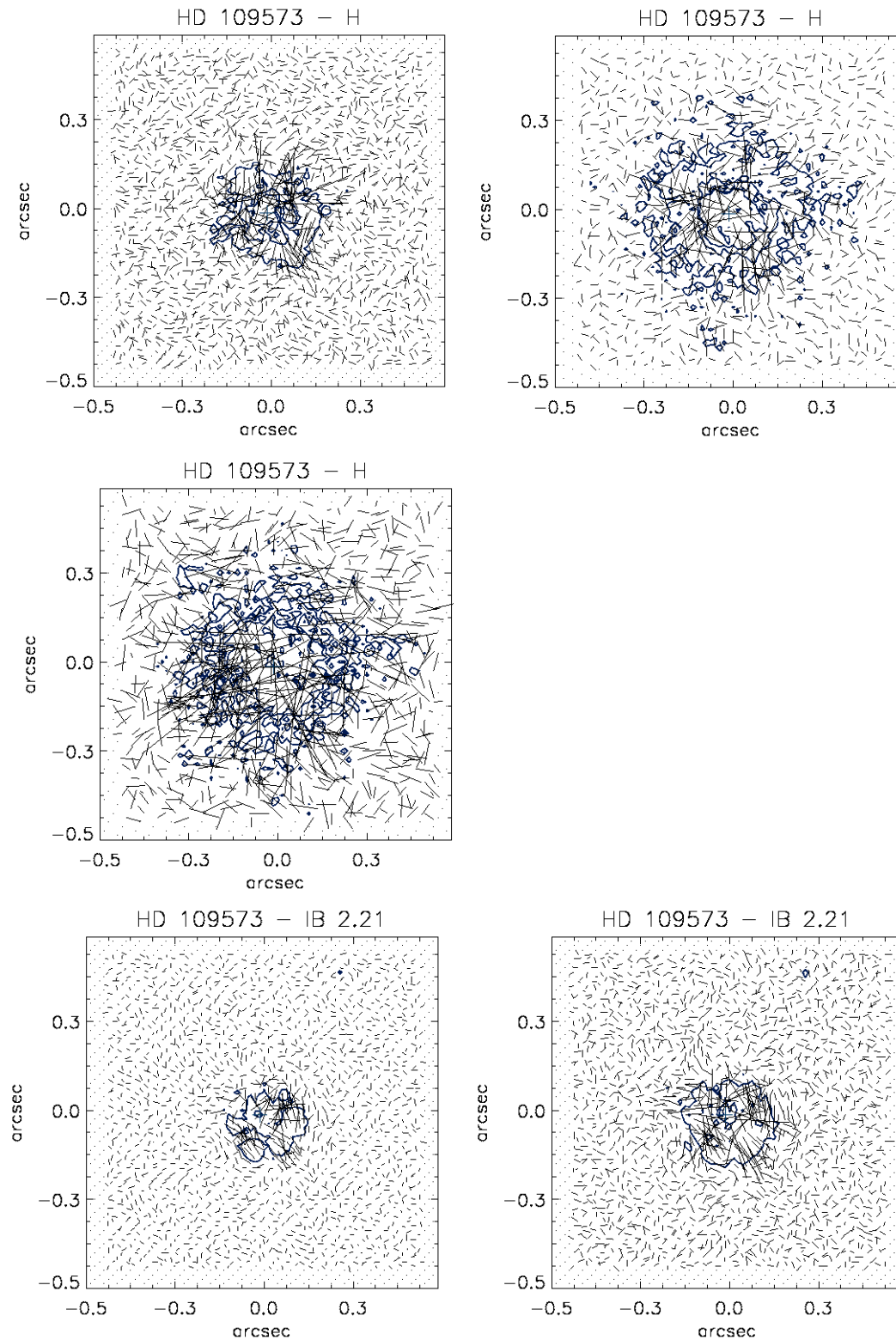


Figure 4.8: Polarisation maps of CR Cha in H and Ks filters at position angles 0° (right) and 180° (left). Observations at PA= 180° were obtained with a shorter DIT. North is up, east is left at PA= 0° .



- HD 97048 : Figure 4.7 at the right hand side. The polarisation vectors have an aligned pattern in H, while they are random both in Ks and NB 1.64.
- Cr Cha : The target was observed using short and long detector integration times (DIT's) in H and Ks filters. All four polarisation maps (Figure 4.8) show an aligned pattern, which is stronger for the observations with longer DIT's. The polarisation patterns in H and Ks are not orientated in the same direction, but rotated by about 45° . In both filters the highest degree of polarisation is between 5-8%, while the background has a degree of polarisation of approximately 2%. Interestingly, the PI image in Ks (short DIT) appears to be far more elongated, with a different axis of elongation then the polarised intensity observed in H band.

Figure 4.9: Polarisation maps of HD 109579 in H (DIT = 3, 10 and 60s) and IB 2.21 (DIT = 20 and 50s) filters. North is up, east is left.



- HD 109579 : All polarisation maps (Figure 4.9) exhibit a random polarisation pattern. Additionally to the maps presented in Figure 4.9 we produced maps showing the surroundings of HD 109579 at larger separations in order to search for traces of the dust ring at $1.05''$. No signs, neither in the polarised intensity distribution nor in the polarisation maps, of the dust ring could be found.
- WLY 2-43 : Aligned polarisation pattern, covering an extended area of the polarised intensity distribution in both Ks and IB 2.21 (see Figure 4.10).
- WL 17 : The contour plots of the polarised intensity (Figure 4.11) in Ks show a lobe towards the north-east, which extends up to $0.5''$ from the center and is not distinguishable in the total intensity distribution. The central sources and the extending lobe are covered by a structured vector pattern, which is aligned over the center (marked by the blue plus sign), but appears to become slightly centrosymmetric over the lobe. In addition the degree of polarisation is highest over the lobe with P_{Ks} up to 30%, while the surrounding region has a degree of polarisation lower than 8%. Interestingly, the direction of the elongation of the polarised intensity of WL 17 in the IB 2.21 filter differs from the orientation in Ks.

4.2.4.2 HD 100546

While HD 100546 appears point-like in the intensity distribution (Figure 4.6), its polarised intensity distribution is elongated along the east-west direction in H, Ks and IB 2.18 (see Figure 4.12). Only in NB 1.64 the polarised intensity is point-like. Here the structure of the polarisation vectors is random, contrary to the H band where the pattern is aligned along the axis of elongation, and contrary to the Ks and IB 2.18 filters, where the polarisation vectors are curved, not centrosymmetric, but rather bended away from the center of the star.

Figure 4.13 displays the Stokes U and Q vectors of HD 100546, which both show the so-called butterfly pattern. Usually a butterfly pattern is a sign for a face-on disc, like in the case of TW Hya (Apai et al., 2004). For HD 100546 this is not possible, since the disc has a measured inclination of $50^\circ \pm 5^\circ$ from edge-on. Following the approach by Apai et al. (2004) we plotted the polarisation signal in dependence of the position angle (Figure 4.14). The profile is similar to sinusoidal, but somewhat offset to higher negative count rates.

The maps of the degree of polarisation show two regions of higher polarisation, like in Figure 4.13, in H, Ks and IB 2.18. In all three filters the measured degree of polarisation is about $P = 6 - 7\%$, while the background polarisation is less than 2%.

4.2.4.3 WLY 2-44

The intensity distribution of WLY 2-44 (Figure 4.13) shows two intensity maxima separated by approximately $0.36''$. While the eastern source is the star, the western source could either be a secondary or a maxima of the outflow from WLY 2-44. Since it appears as a bright source in both the Stokes vectors and the polarised intensity distribution, it is very unlikely that the western source is a secondary star. Additionally the highest degree of polarisation $P_{Ks} \sim 65\%$, compared to $P_{BG} = 15\%$ for the background, coincides with the position of the western intensity maxima.

Figure 4.10: Polarisation maps of WLY 2-43 in Ks (DIT = 12 and 200s) and IB 2.21 (DIT = 100s) filters. North is up, east is left.

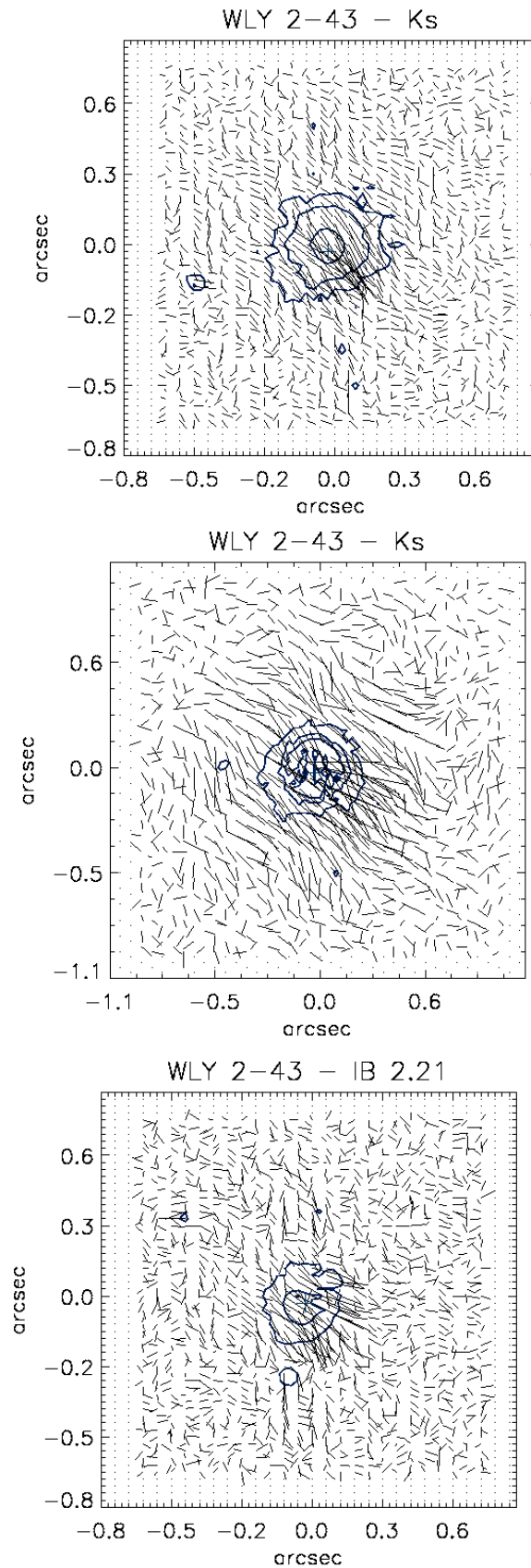


Figure 4.11: Polarisation maps of WL 17 in Ks (DIT =12, 60 and 120s) and IB 2.21 (DIT = 180s) filters. North is up, east is left.

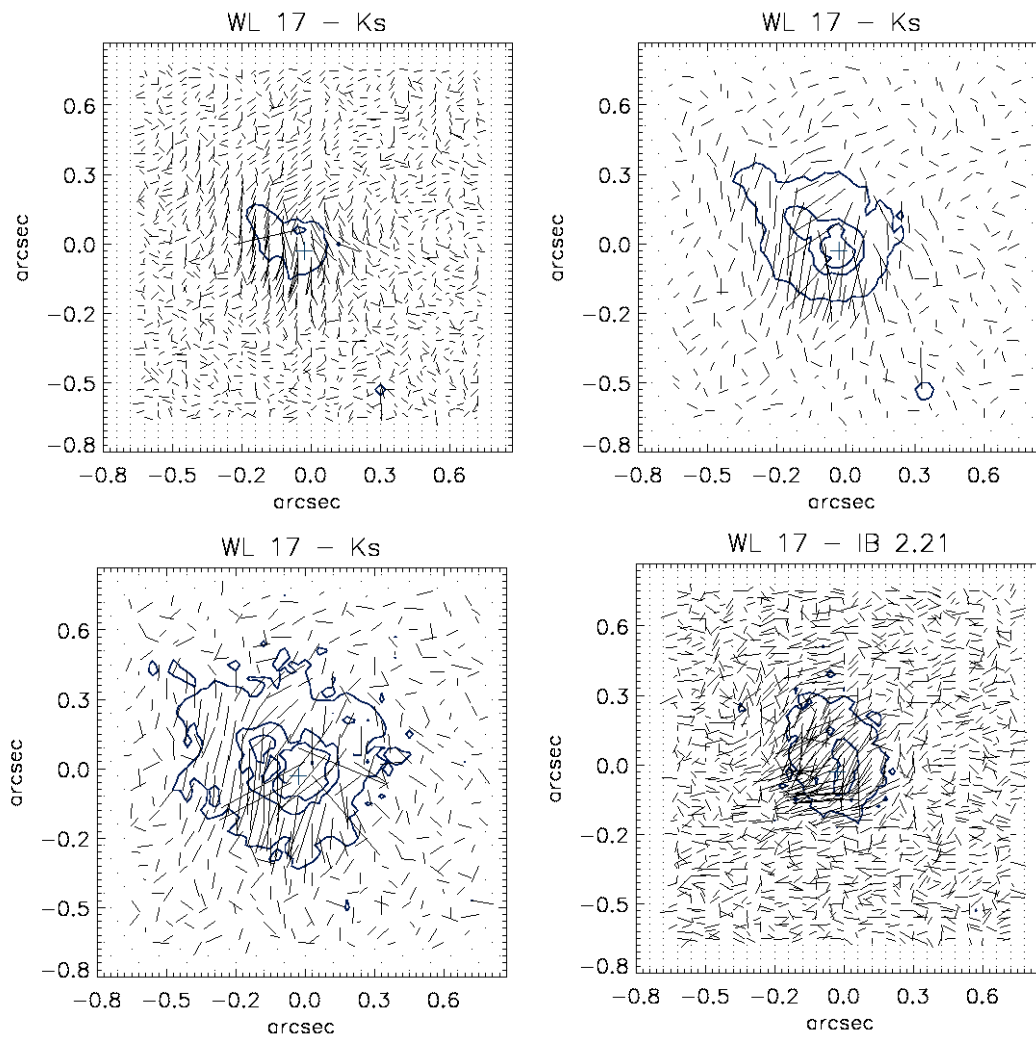


Figure 4.12: Polarisation maps of HD 100546 in H, Ks, IB 2.18 and NB 2.18 filters. The H band map has been rotated by 90° to match the position angle of the three other observations. north east?

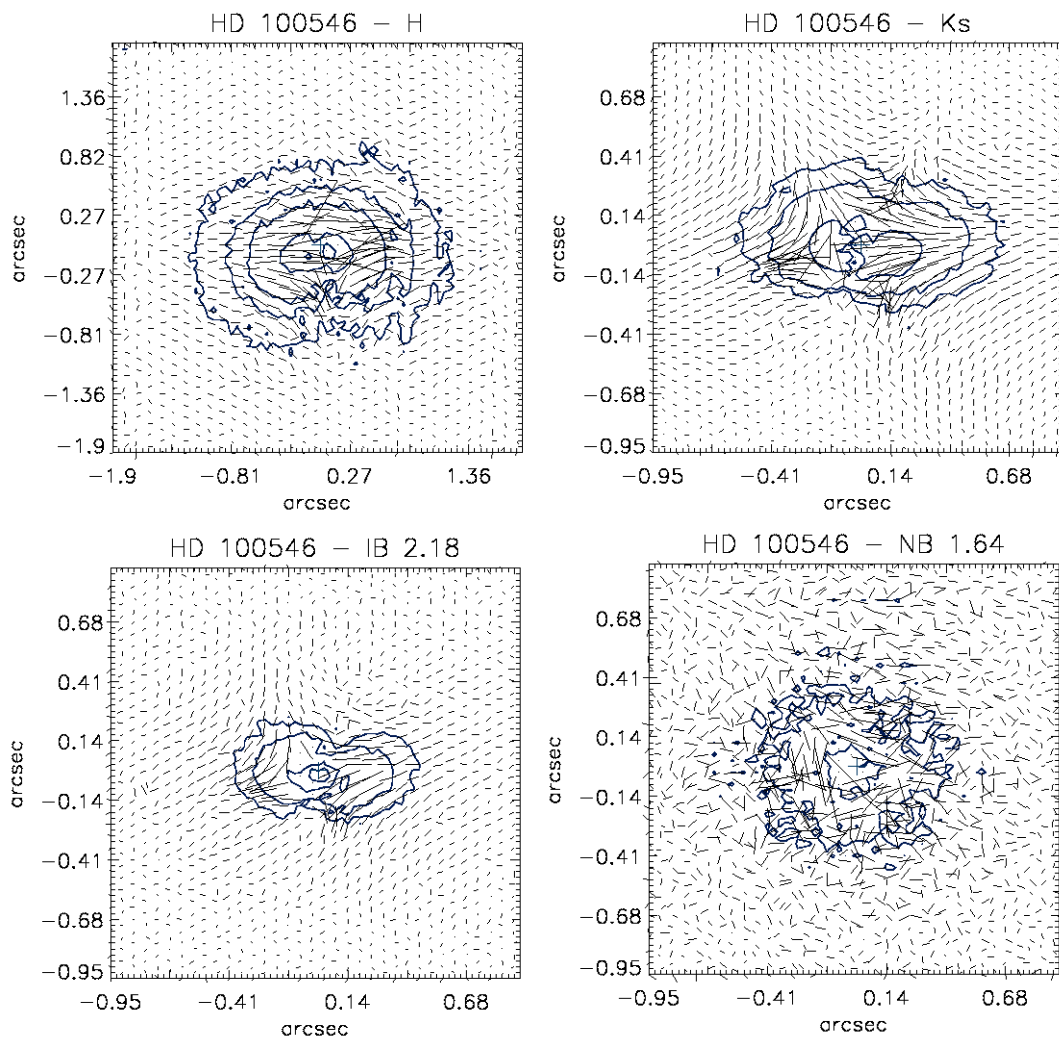


Figure 4.13: Comparison of the Stokes U and Q vectors, the polarised intensity PI, the intensity I and percentage of polarisation for HD 100546 (left) and WLY 2-44 (right) in Ks band.

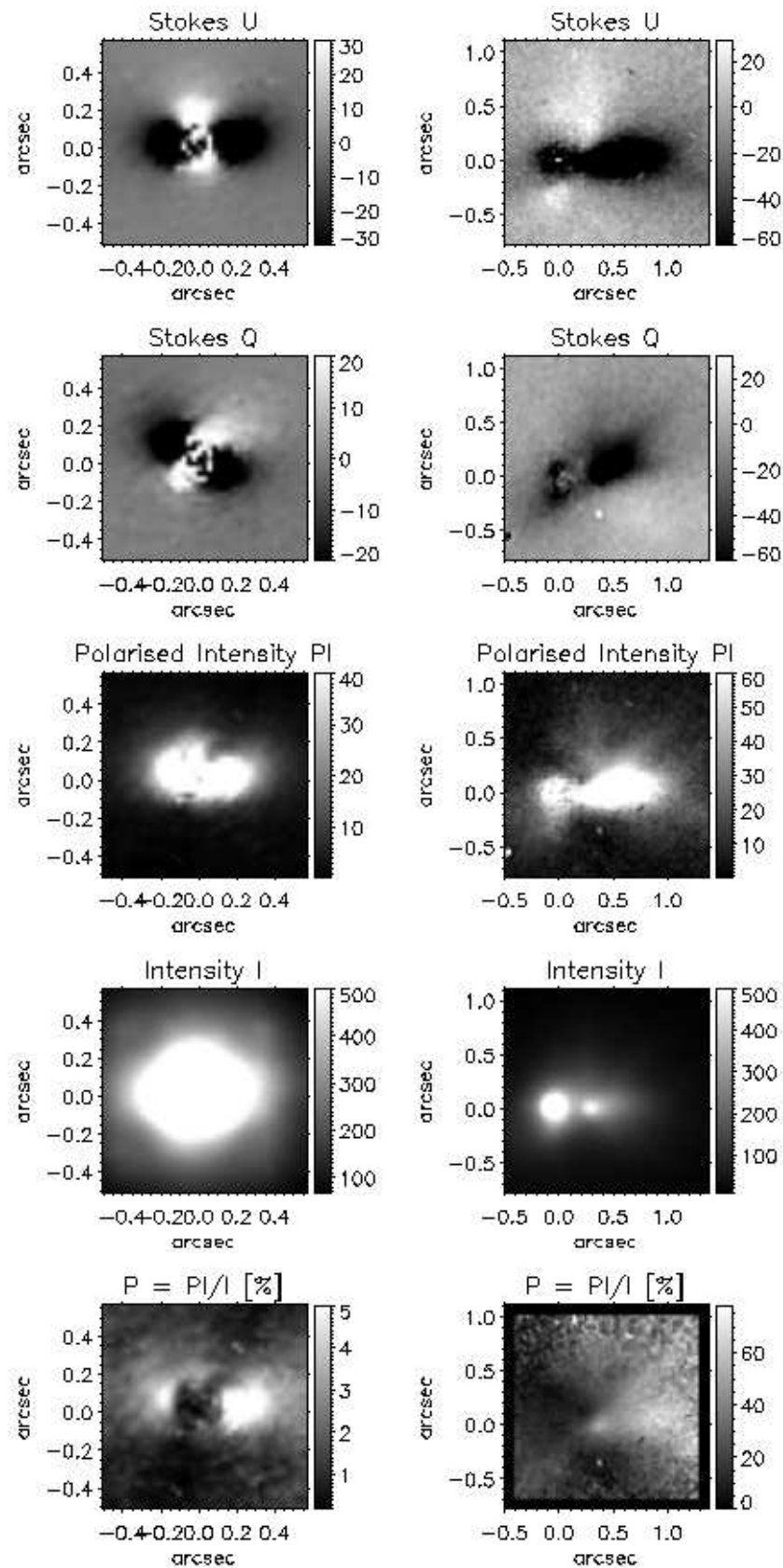
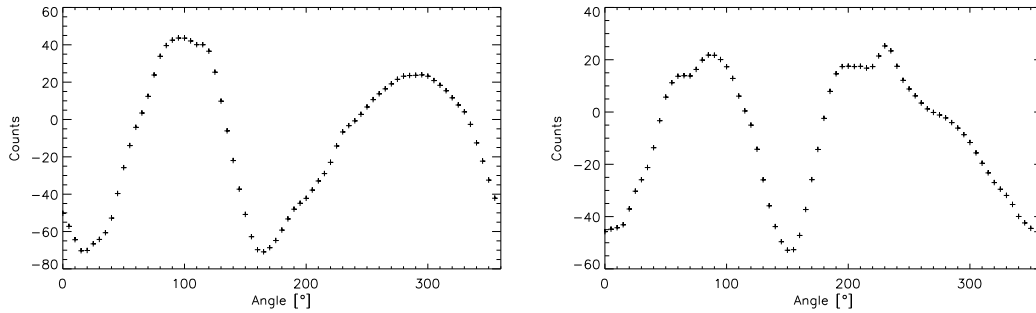


Figure 4.14: Polarisation signal in the Stokes U (left) and Q (right) component as a function of position angle in an annulus between 0.08'' and 0.27'' in Ks. Data points were averaged over 5 degrees.



The polarisation maps of WLY 2-44 (Figure 4.15) show an aligned polarisation pattern, somewhat offset from central source, but directly across the second intensity maxima. This outflow can be traced in western direction up to 1.5'', towards the north-west up to 1.3'' and towards the west up to 0.8'' from the stars position. Moreover, in the bottom polarisation map of Figure 4.15 a second aligned pattern of the polarisation vectors appears from the central source in south-eastern direction. This alignment may indicate the presence of a second outflow covered by the star. A weak illumination in the south-eastern corner is also apparent in the Stokes U vector and the polarised intensity image, and can be traced up to 0.5'' from the star.

4.2.4.4 Elias 2-21

The raw images and the total intensity image of Elias 2-21 clearly show a dark lane, likely a disc close to edge-on, rotated by about 45° west of north. The two intensity maxima on the eastern and the western side of the discs plane are separated by $\sim 0.37''$. Lobes of nebulosity are visible, extending from the disc plane up to about 1.9'' towards the east and about 1.5'' in south-western direction (Figure 4.16). Thereby the western lobe has a particular S-shape close to the disc. Towards the north a third lobe of nebulosity is visible. It can be traced up to 1.9'' in H band and 1.4'' in Ks band, respectively.

The polarisation maps of Elias 2-21 are presented in Figures 4.17, 4.18, 4.19 and 4.20. The polarisation vectors in the eastern and western lobe have a strongly aligned pattern, while they are centrosymmetric in the northern lobe, which is best visible in the polarisation maps with longer DIT's in Ks (Figure 4.19) and in the L band (Figure 4.20). While the aligned vector patterns of the eastern and western lobe, suggest that the dust particles are aligned along the outflow direction, the centrosymmetric pattern of the northern lobe is characteristic of a reflection nebula dominated by single scattering. Thus, the northern lobe is more likely to be an illuminated dust cavity rather than a third outflow.

Still, all three lobes have high degrees of polarisation (Figure 4.16). The bright eastern nebulosity has a degree of polarisation of up to $P_{Ks} \leq 70\%$. For the south-western lobe a P_{Ks} of about 50% can be measured, while the northern illumination shows with $P_{Ks} \sim 35\%$ the lowest degree of polarisation of the three. The dark lane traceable between the eastern and western lobes is only to about 10% polarised. This obscured region of low polarisation is

Figure 4.15: Polarisation maps of WLY 2-44 in Ks (DIT = 60 and 200s). North is up, east is left.

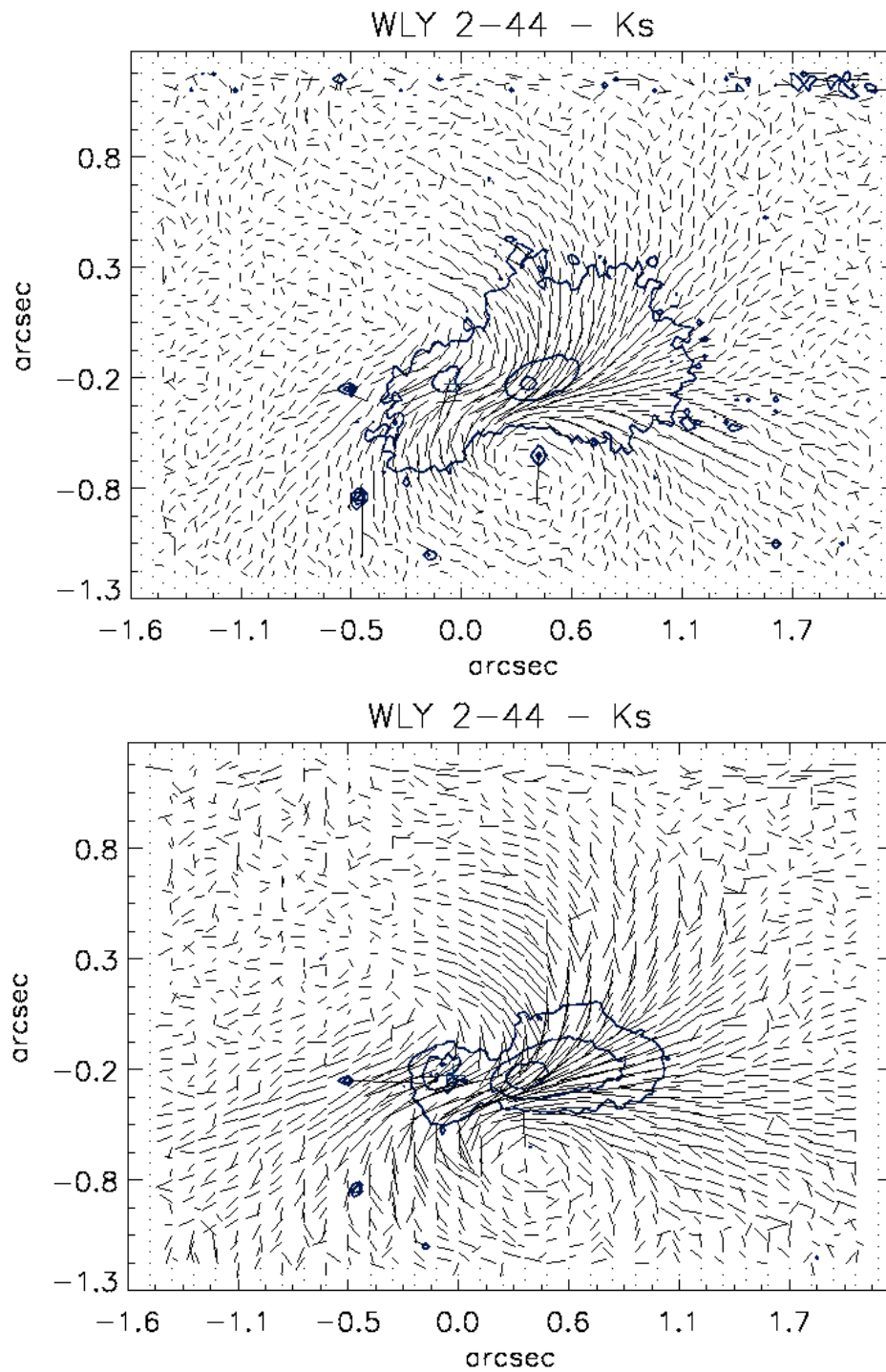


Figure 4.16: Comparison of the Stokes U and Q vectors, the polarised intensity PI, the intensity I and percentage of polarisation for Elias 2-21 in H (left) and Ks (right). North is up, east is left.

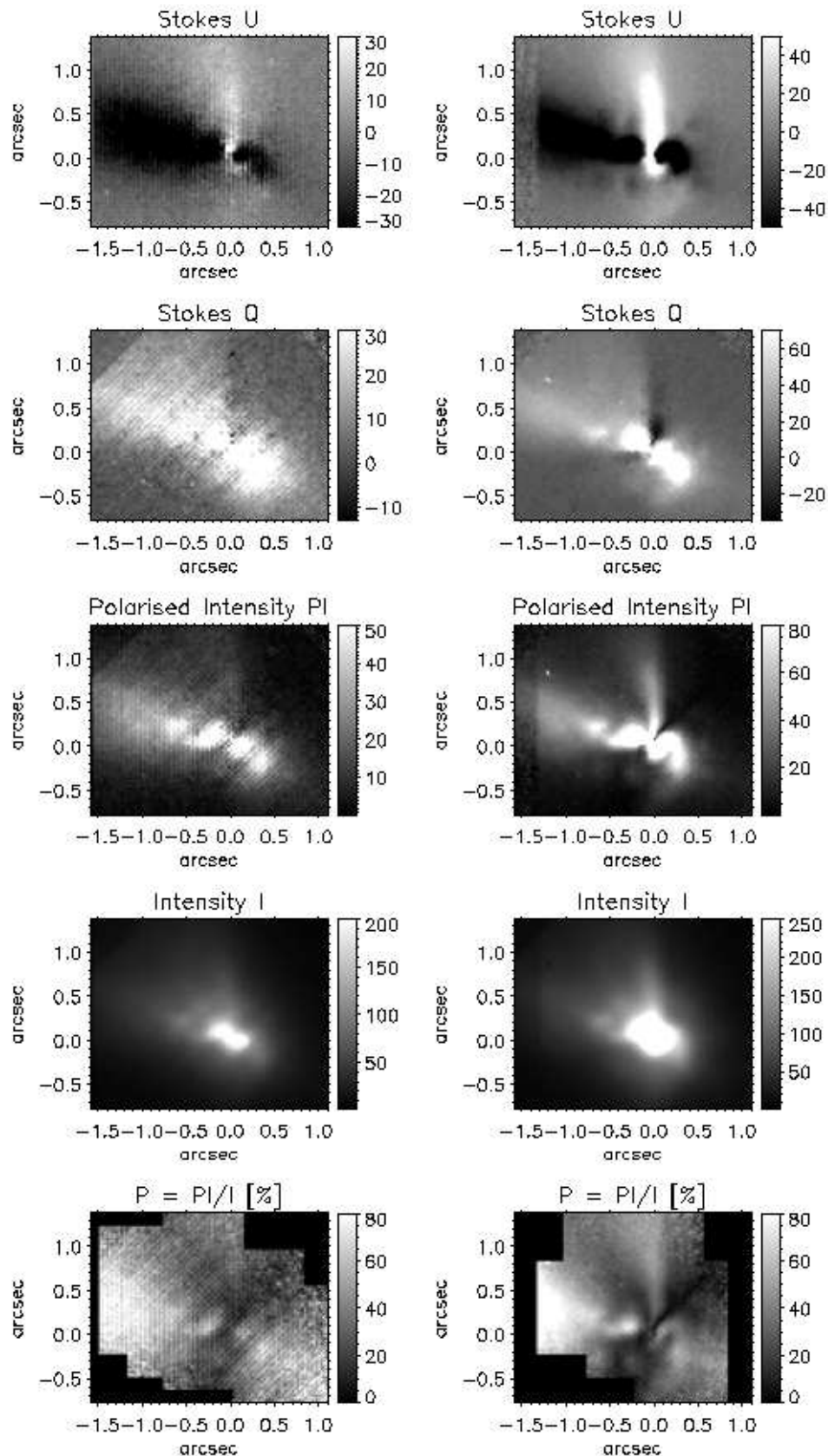


Figure 4.17: Polarisation maps of Elias 2-21 in H (DIT = 30 and 180s). North is up, east is left.

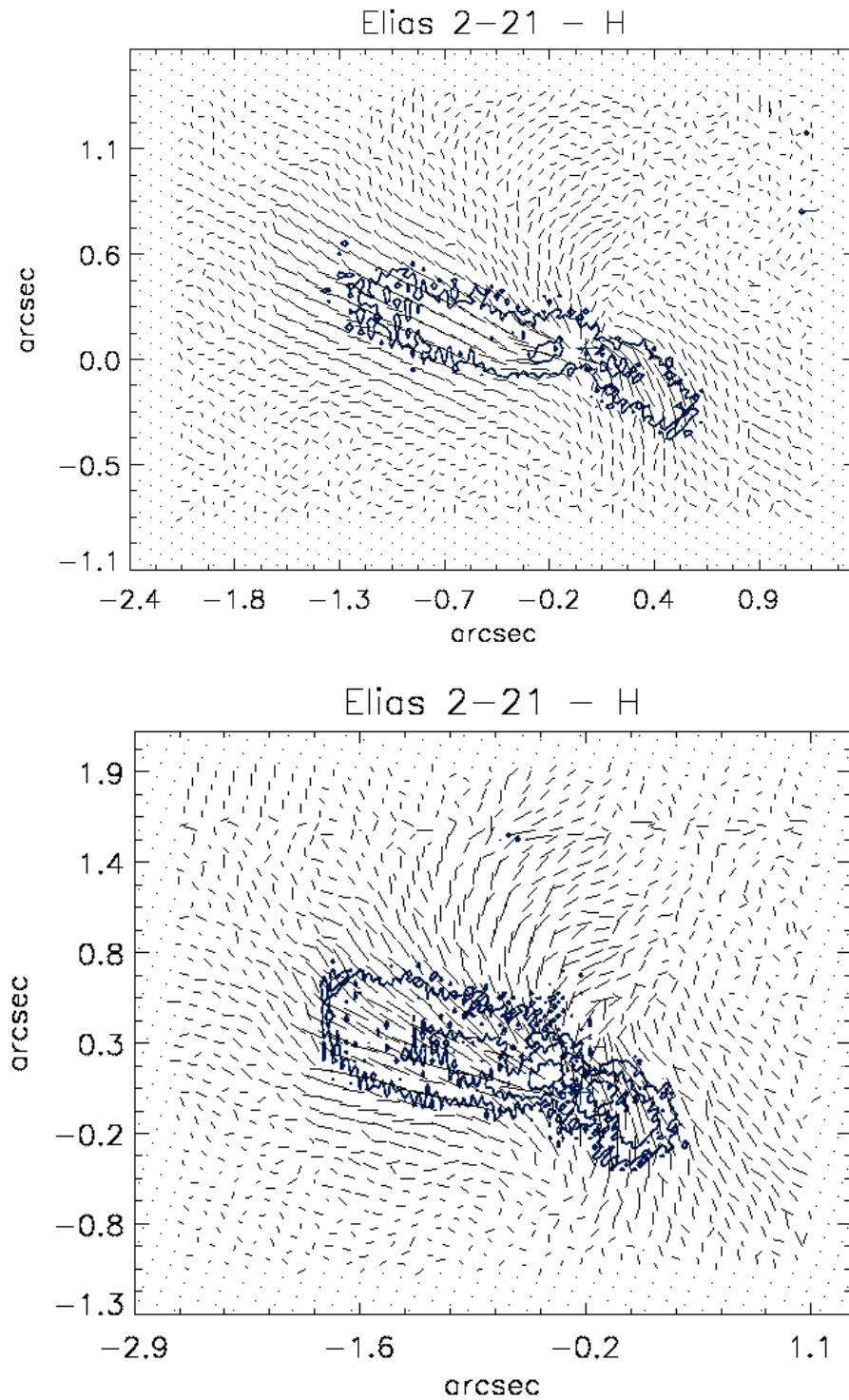


Figure 4.18: Polarisation maps of Elias 2-21 in Ks (DIT = 1.7 and 20 s).

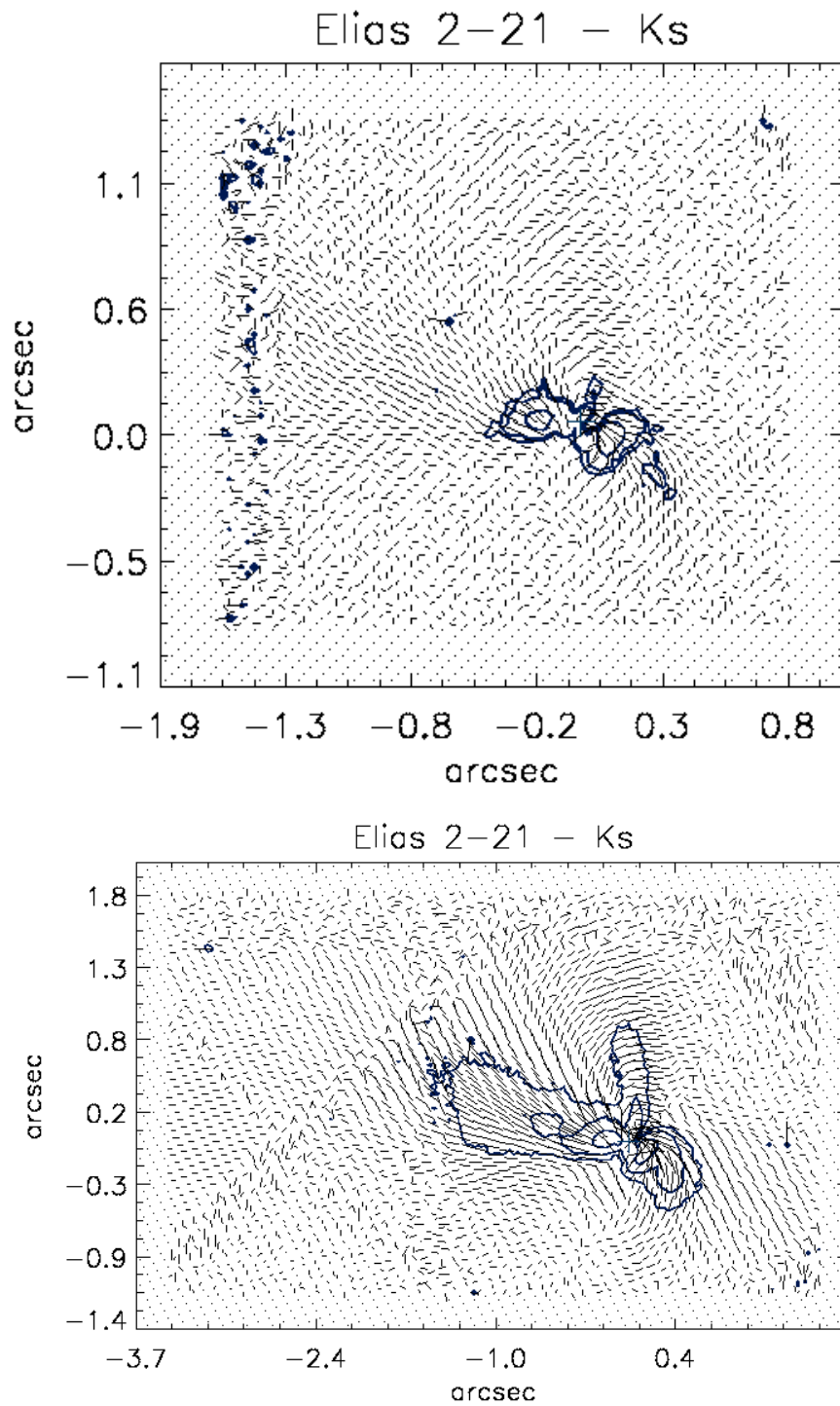


Figure 4.19: Polarisation maps of Elias 2-21 in Ks (DIT = 60 and 120s). North is up, east is left.

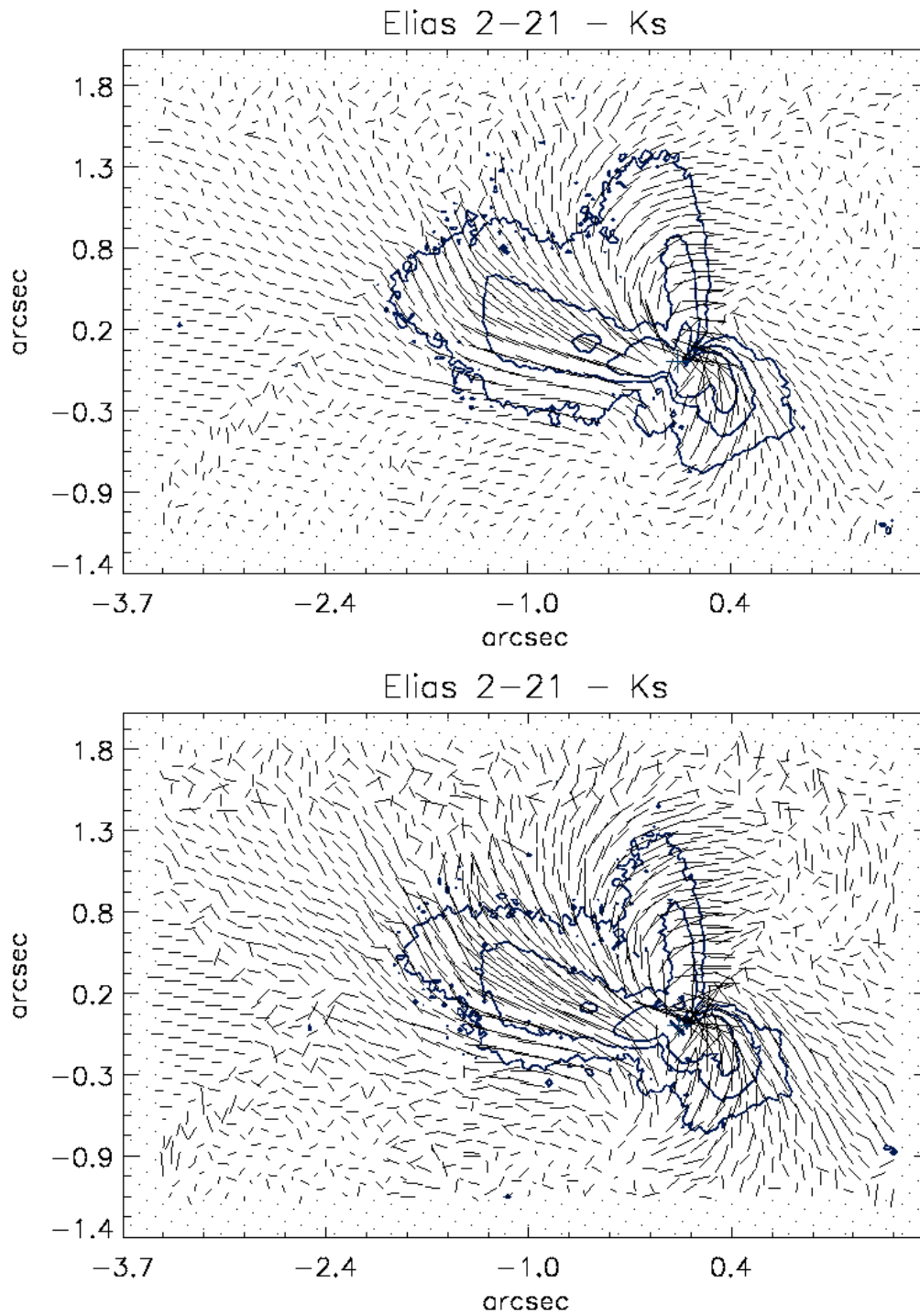
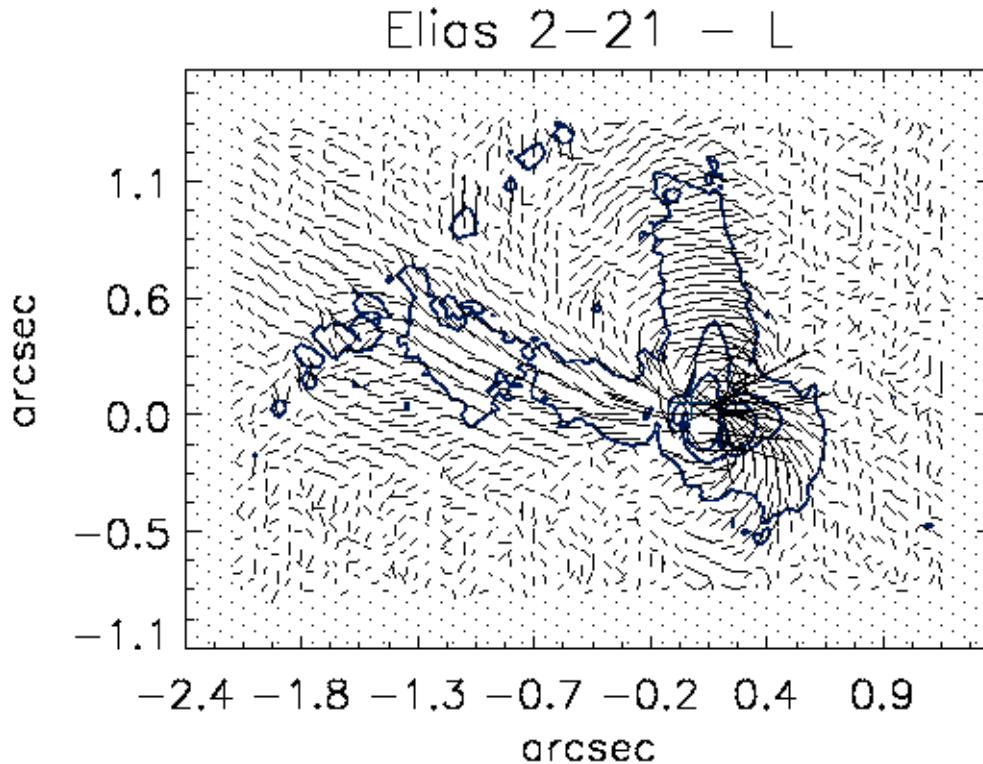


Figure 4.20: Polarisation map of Elias 2-21 in L'. North is up, east is left.



the edge on disc. The low polarisation in the disc is due to multiple scattering (Kóspál et al. (2008), Bastien & Menard (1990)). Oddly, the polarisation maps show no polarisation vectors orientated parallel to disc plane as predicted by theoretical models from, e.g., Whitney & Hartmann (1993) and Fischer et al. (1996).

4.2.5 Discussion

None of the eight sources, for which the polarisation maps could be calculated, shows a centrosymmetric vector pattern, which is commonly associated with young stellar objects (Gledhill (2005), Hales et al. (2006) and Beckford et al. (2008)). Instead seven of the eight sources exhibit an aligned vector pattern in one or more filters. Those patterns of parallel lines are usually referred to as polarisation disc. To reproduce a polarisation disc in theoretical models a population of aligned grains has been necessary (Lucas & Roche, 1998).

Still, there are four proposed mechanism for the production of a polarisation disc :

1. dichroic extinction
2. double scattering on a physical thick disc
3. double scattering from the cavity walls down onto the equatorial plane
4. an 'illusory disc' created by the PSF of the telescope, when flux from bright regions above and below the mid plane is spread into the fainter equatorial region

'Illusory discs' were first reported by Whitney et al. (1997), who also stated that the size of an 'illusory disc' decreases with increasing spatial resolution, while a real polarisation disc may emerge with improving resolution. Since the observations were conducted with high spatial resolution it is rather unlikely that they are pure 'illusory discs'. Additionally, since none of the observations of Di Cha, Cr Cha, HD 97048 or WLY 2-43 show indications for a physical thick disc, we disregard explanation 2. as possible scenario.

Fischer et al. (1996) conducted extensive simulations of polarimetric observations in the near-infrared wavelength regime. Thereby the pre-main sequence object is assumed to consist of a disc, a bipolar outflow and the cloud core. In their models aligned polarisation vectors preferably appear in connection with multiple scattering and as striking features close to the disc plane. Fischer et al. (1996) state that "... these polarisation patterns are produced by illuminating the disc with light scattered from the lobes." Furthermore, they note that aligned polarisation patterns generally appear more pronounced for larger angles of inclination (closer to edge-on), higher densities, smaller wavelengths and larger particles. While a disc-like arrangement of the polarisation vectors is preferably seen for nearly edge-on discs, the authors point out that one of their models also shows aligned vector patterns for small angles of inclination.

The latter scenario could explain, why we observe aligned polarisation vector patterns without indications for an edge-on disc.

As mentioned before the polarisation vector patterns of Di Cha and Cr Cha show a change in orientation between the H and Ks band observations. Since all of the observations of each target were taken during the same night a variation in the structure of the source itself, like a outburst, is unlikely. An explanation may be found in the morphology of the polarised intensity. For Cr Cha the polarised intensity profile is clearly elongated along the west-east direction in Ks, while the profile in H band displays a generally rounded shape with a slight elongation from north-west towards south-east. Such a behaviour has already been described by Gledhill (2005). There polarimetric observations of IRAS 20461+3853 in J and Ks bands also display a changing polarisation vector pattern connected to a change in the morphology of the polarised intensity. Only, for Di Cha no such change in the PI morphology is evident. The polarised intensity both in H and Ks band appears to be nearly point-like.

4.3 Conclusion

We observed twelve young stars using the polarimetric differential imaging mode (PDI) of NACO to trace the extend of the disc material at high angular resolution. For eight of the observed targets we were able to calculate the Stokes U and Q vectors and therefrom the polarised intensity distribution of the sources. While most of the sources have a point-like intensity distribution as well as a point-like polarised intensity distribution and show only local, aligned polarisation patterns over the PSF area, three stars exhibit a more complex polarised vector pattern. Two of them, WLY 2-44 and Elias 2-21, are associated with extended nebulosity's traceable in the intensity distribution as well as in the polarised intensity distribution. Thereby, Elias 2-21 clearly shows a bipolar flux distribution, separated by an almost edge-on disc. For WLY 2-44 only one extended nebulosity is visible in the intensity and polarised intensity maps. But, there is evidence for a second nebulosity/outflow covered by the central star in the Stokes vectors, the polarised intensity and the polarisation maps.

Furthermore, both targets exhibit high degrees of polarisation, up to 70%. Generally, the ρ Oph targets show a much higher degree of polarisation, if detected, than the older targets, which is explained by the more evolved state of their discs.

Chapter 5

Summary and Outlook

Finally, to summarize the work presented :

- To test the ability of current theoretical models to reproduce the mid-infrared spectra of brown dwarfs, we observed a small sample of brown dwarfs in multiple systems with VISIR in three narrow band filters. The measured fluxes agreed quite well with the theoretical calculated flux values.
- While the first observations of the binary brown dwarf HD 130948BC showed indications of being variable at $10.5\ \mu\text{m}$, follow-up monitoring observations proved it to be stable at both $8.6\ \mu\text{m}$ and $10.5\ \mu\text{m}$. Despite the fact that no definite variability could be detected in the case of HD 130948BC near- and mid-infrared monitoring program's discover more and more photometric variable brown dwarfs (Goldman et al. (2008), Morales-Calderón et al. (2006)). The detection of photometric variability may provide information's about the inhomogeneity of the atmospheres, which could host weather-like phenomena.
- While the mid-infrared survey for low-mass and planetary companions to bright, near-by star using T-ReCS and VISIR did not return any detection, it proved that planetary and brown dwarf companions are detectable at separation as close as $2''$ from the primary at mid-infrared wavelengths.
To better suppress the limiting background noise and thus to improve the sensitivity limits reached by the VISIR, we plan on reducing the VISIR data with a more sophisticated pipeline developed by E. Pantin.
- Polarimetric differential imaging observations in combination with high angular resolution are a powerful tool to study circumstellar environments of young stellar objects and stars at close separations from the central source. The technique allows us to trace outflows extending from the source and reflection nebula in the surrounding neighbourhood of the source.
In the context of this work we studied twelve young objects using near-infrared observations conducted with NACO in PDI mode. Two of the observed objects showed extensive outflows extending up to $1.9''$ from the center of source. In those too cases the regions of high polarised intensity were associated with a high degree of polarisation.

To completely understand the composition of the objects, our future goal is to simulate their structure, the observed polarised intensity and the resulting polarisation vector pattern, using the models by Wolf et al. (2003). The theoretical modelling will help us to understand the distribution of the dust and to determine basic properties like composition and size of the scattering particles.

Within this thesis different aspects of the environment of stars have been studied. We analysed the spectral behavior of brown dwarf companions in the mid-infrared, conducted a mid-infrared search to discover new brown dwarf and planetary companions and studied the dust environment of young stellar objects and stars using polarimetric observations in the near-infrared. But however different and unconnected those studies may seem, in the end they all aim for a better understanding of star formation and evolution.

Appendix A

VISIR 'Burst' Mode Detection Limits

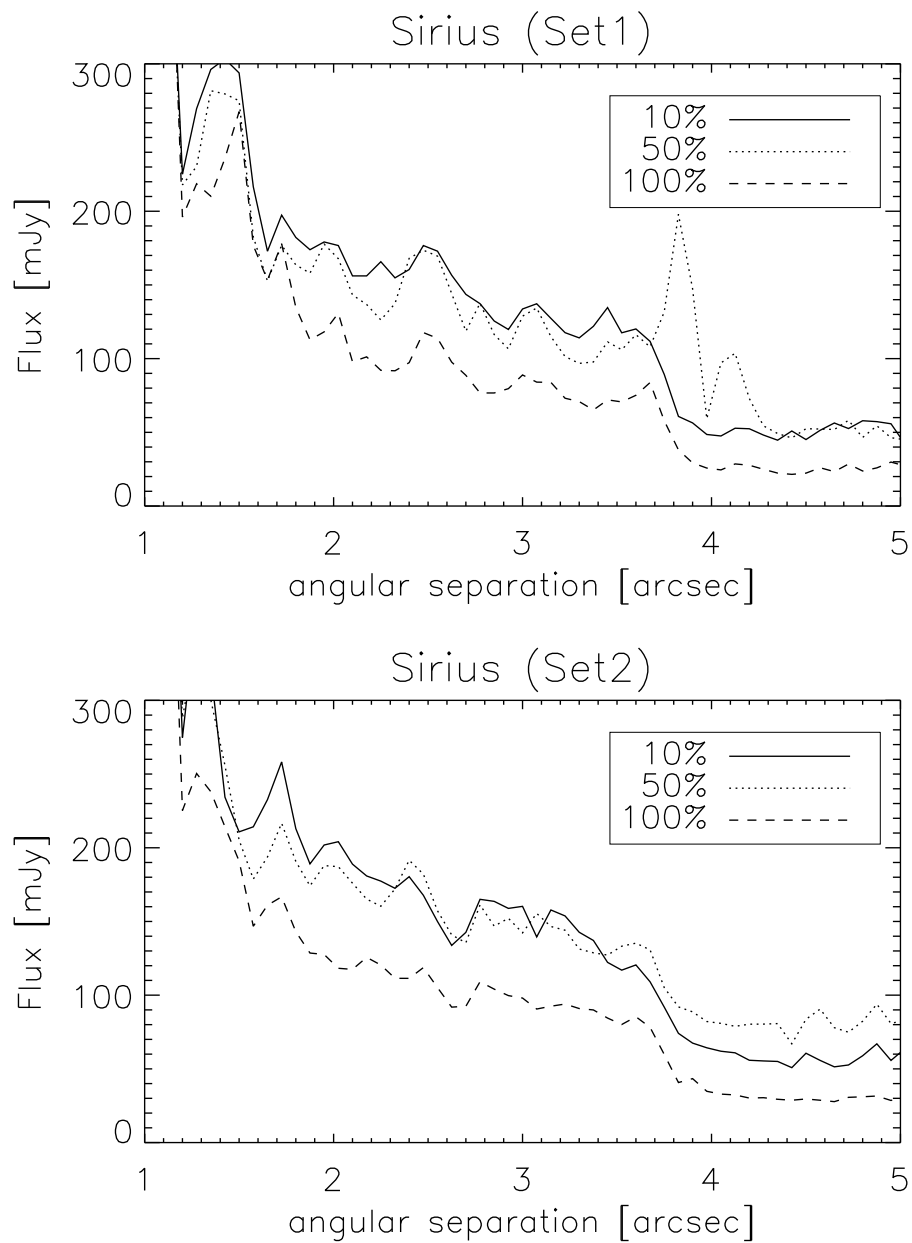
Figure A.1: 5σ sensitivity limit from the observations of Sirius.

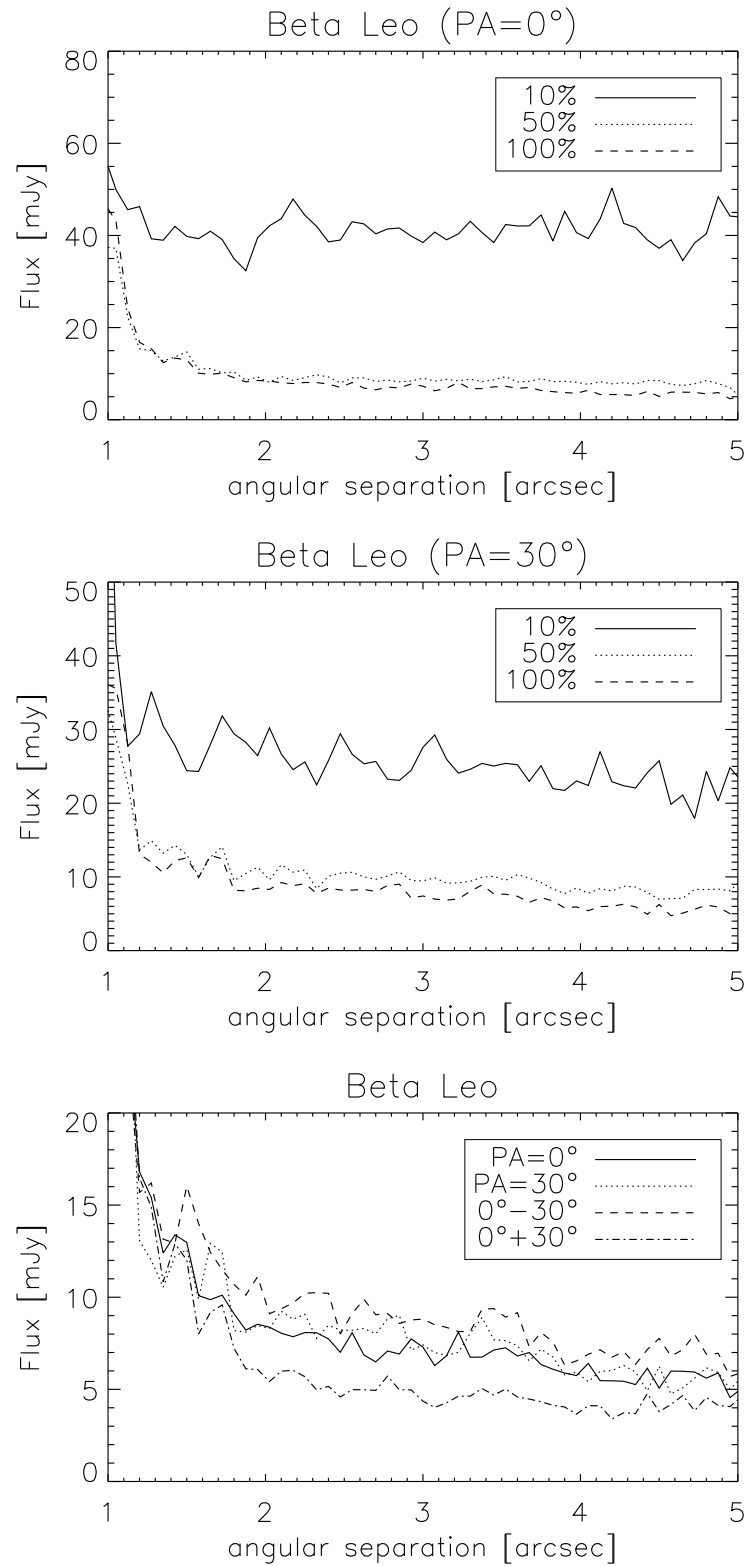
Figure A.2: 5σ sensitivity limit from the observations of β Leo.

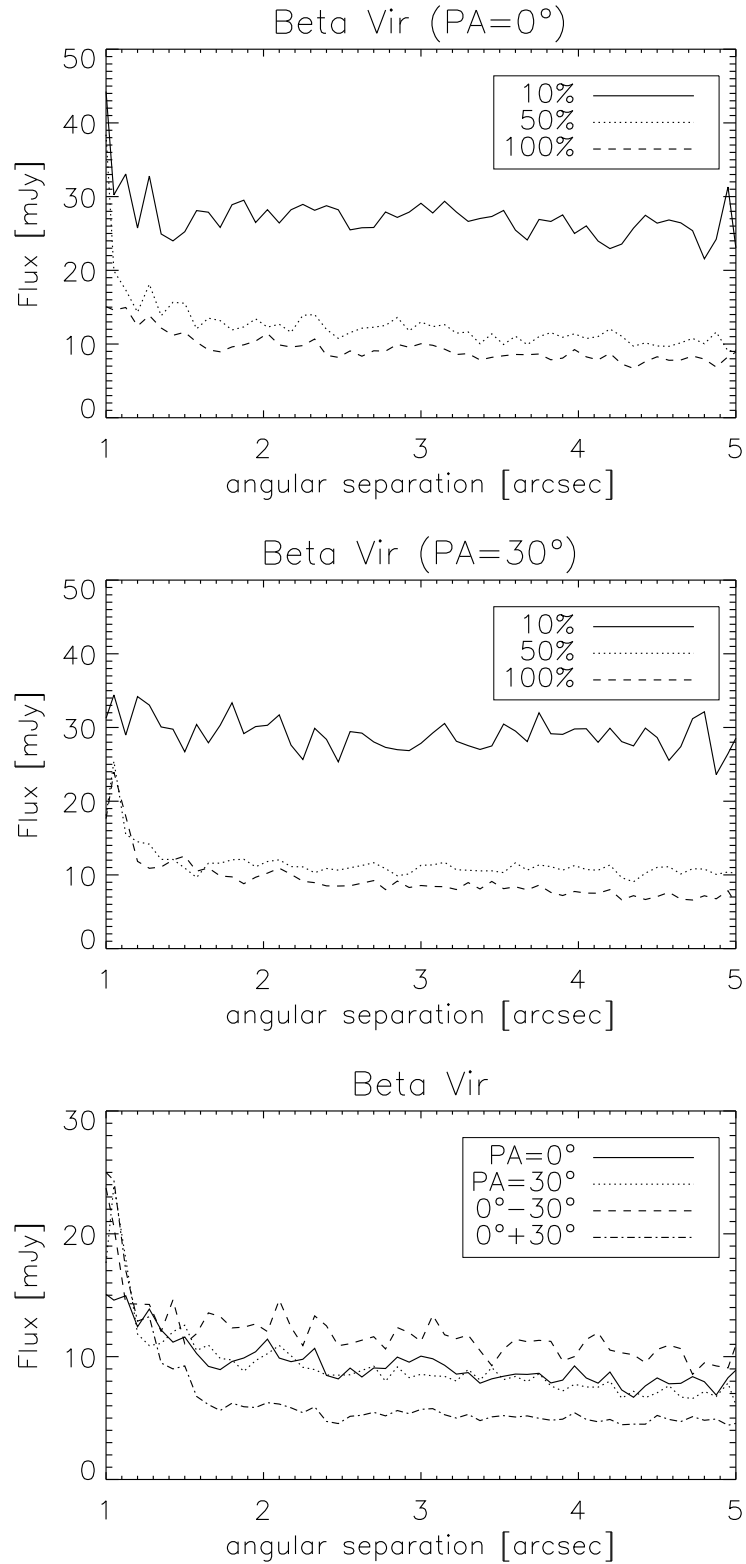
Figure A.3: 5σ sensitivity limit from the observations of β Vir.

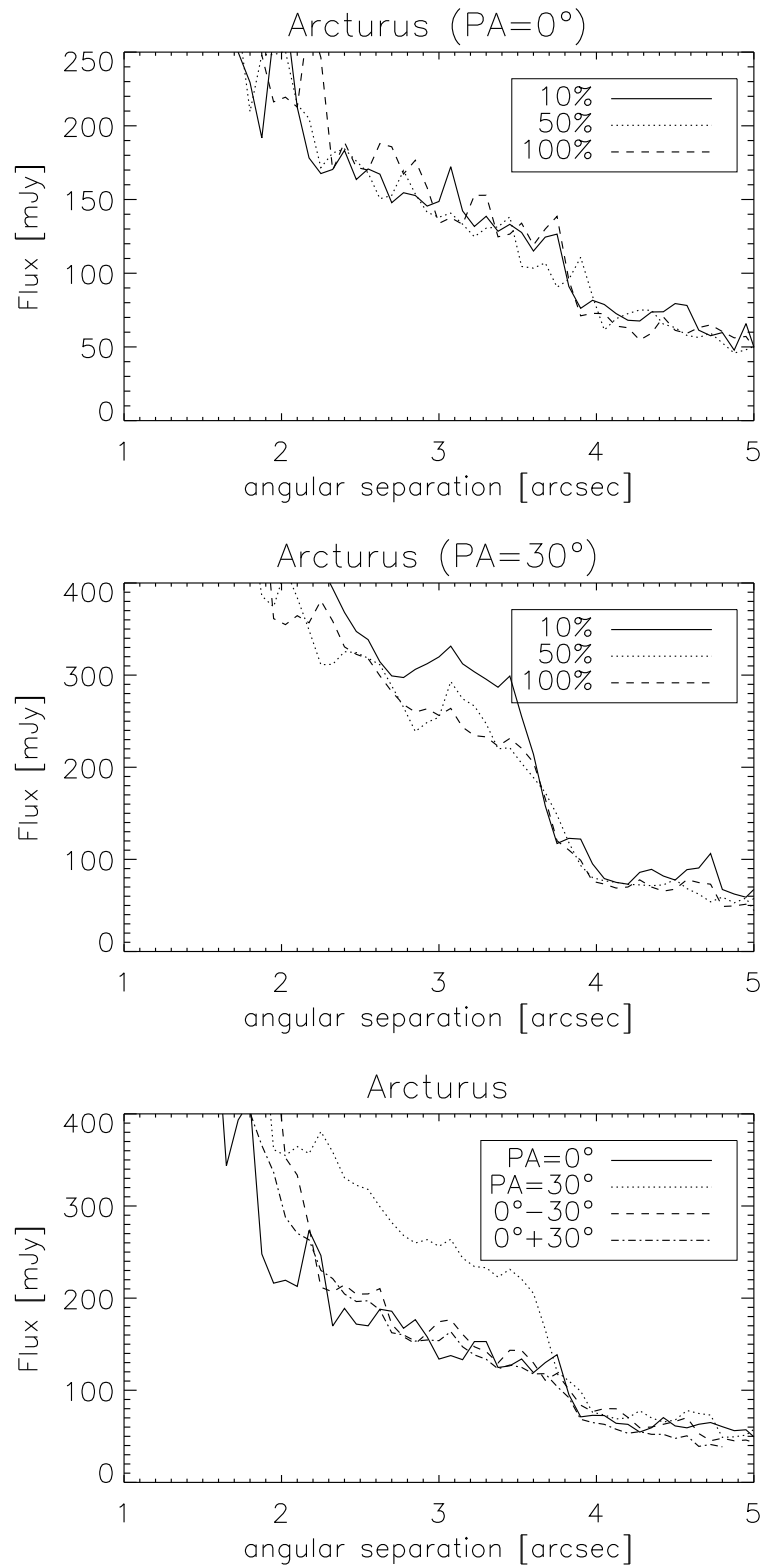
Figure A.4: 5σ sensitivity limit from the observations of Arcturus.

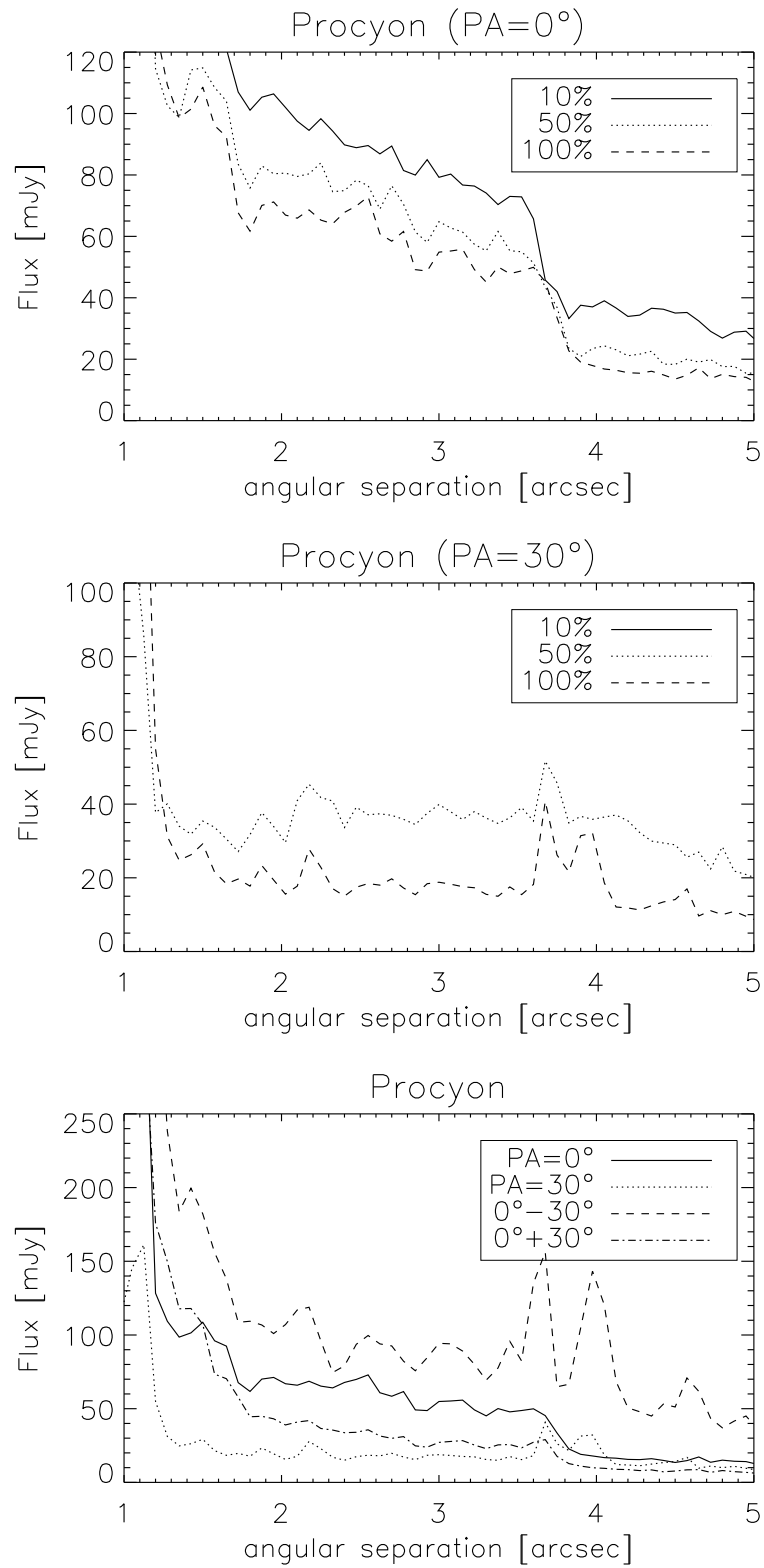
Figure A.5: 5σ sensitivity limit from the observations of Procyon.

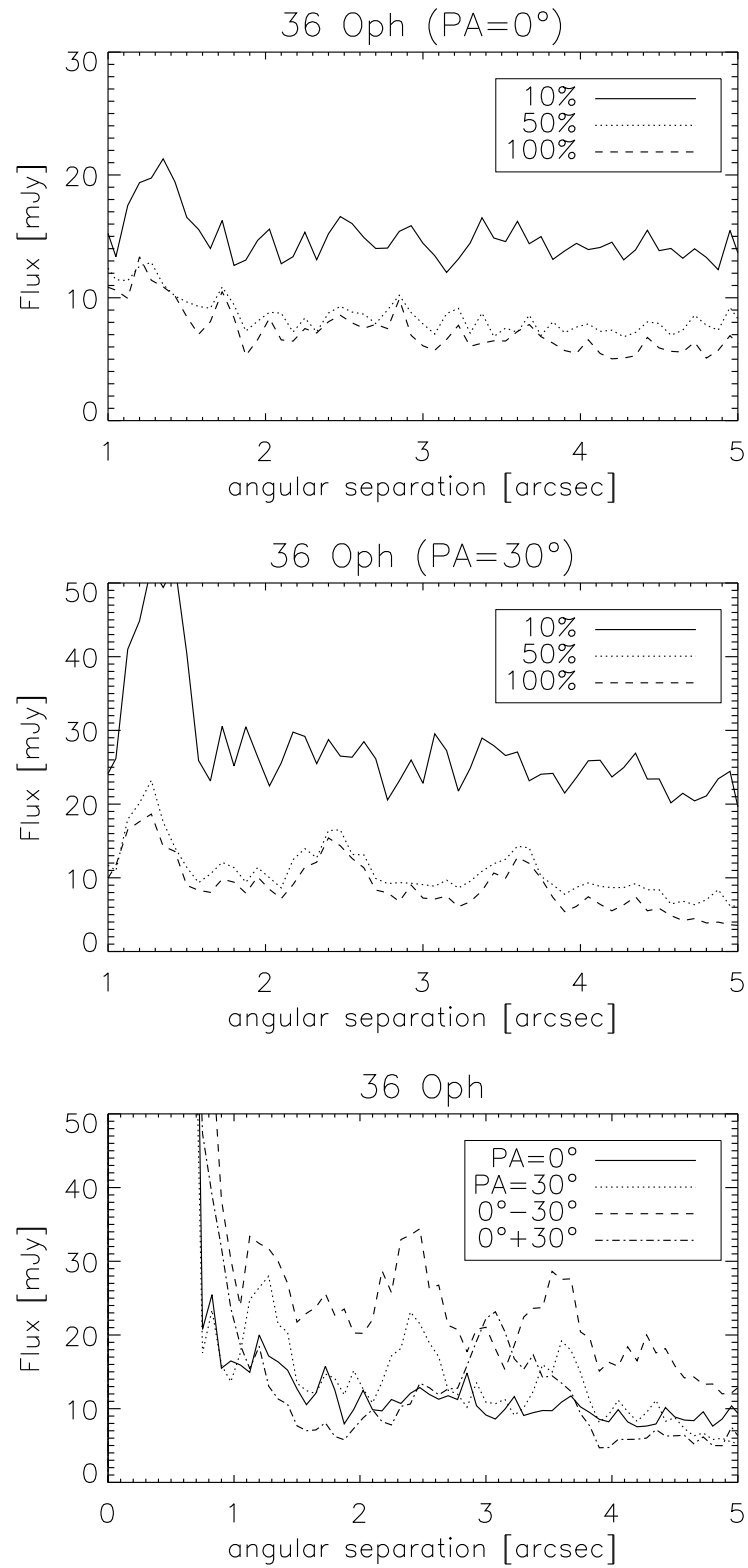
Figure A.6: 5σ sensitivity limit from the observations of 36 Oph.

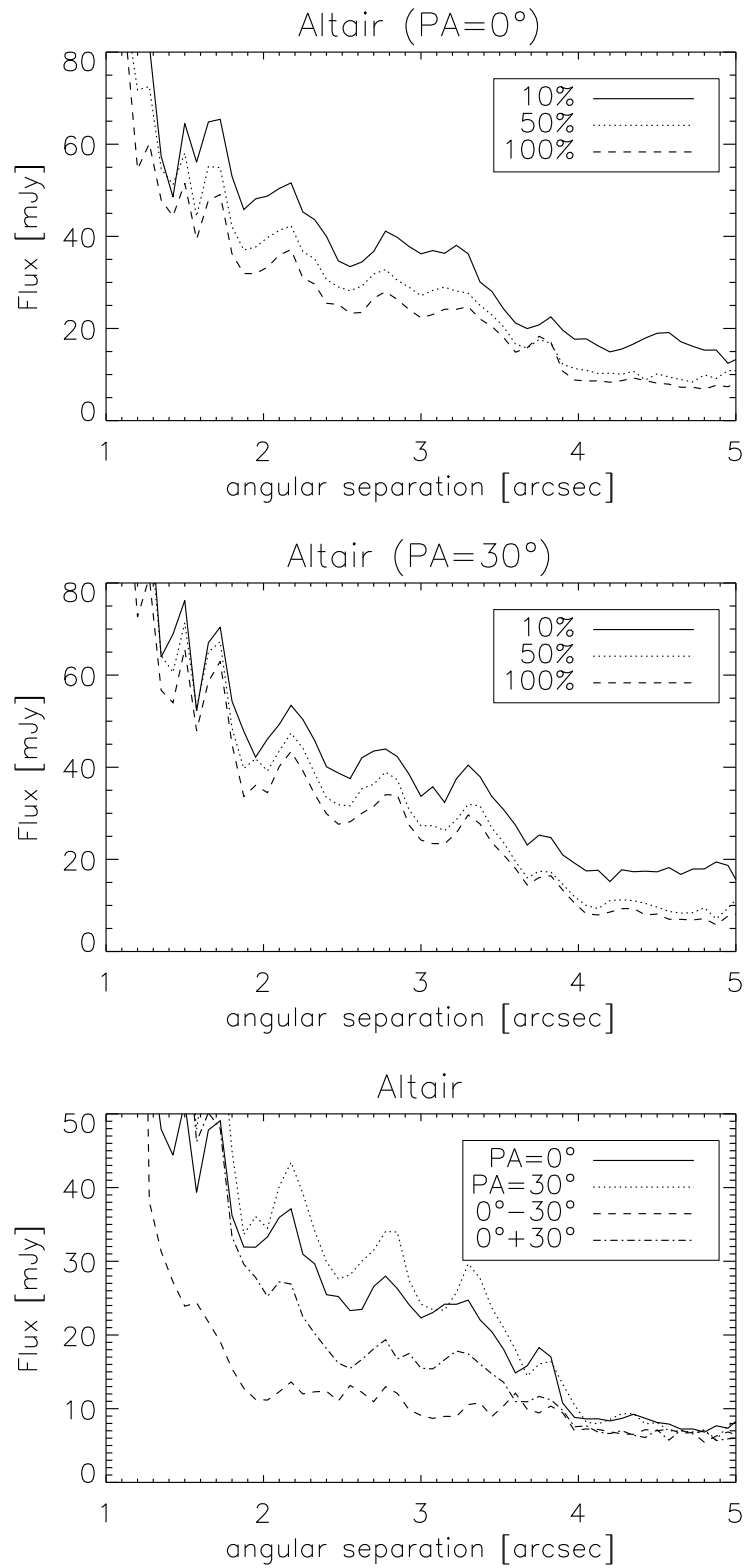
Figure A.7: 5σ sensitivity limit from the observations of Altair.

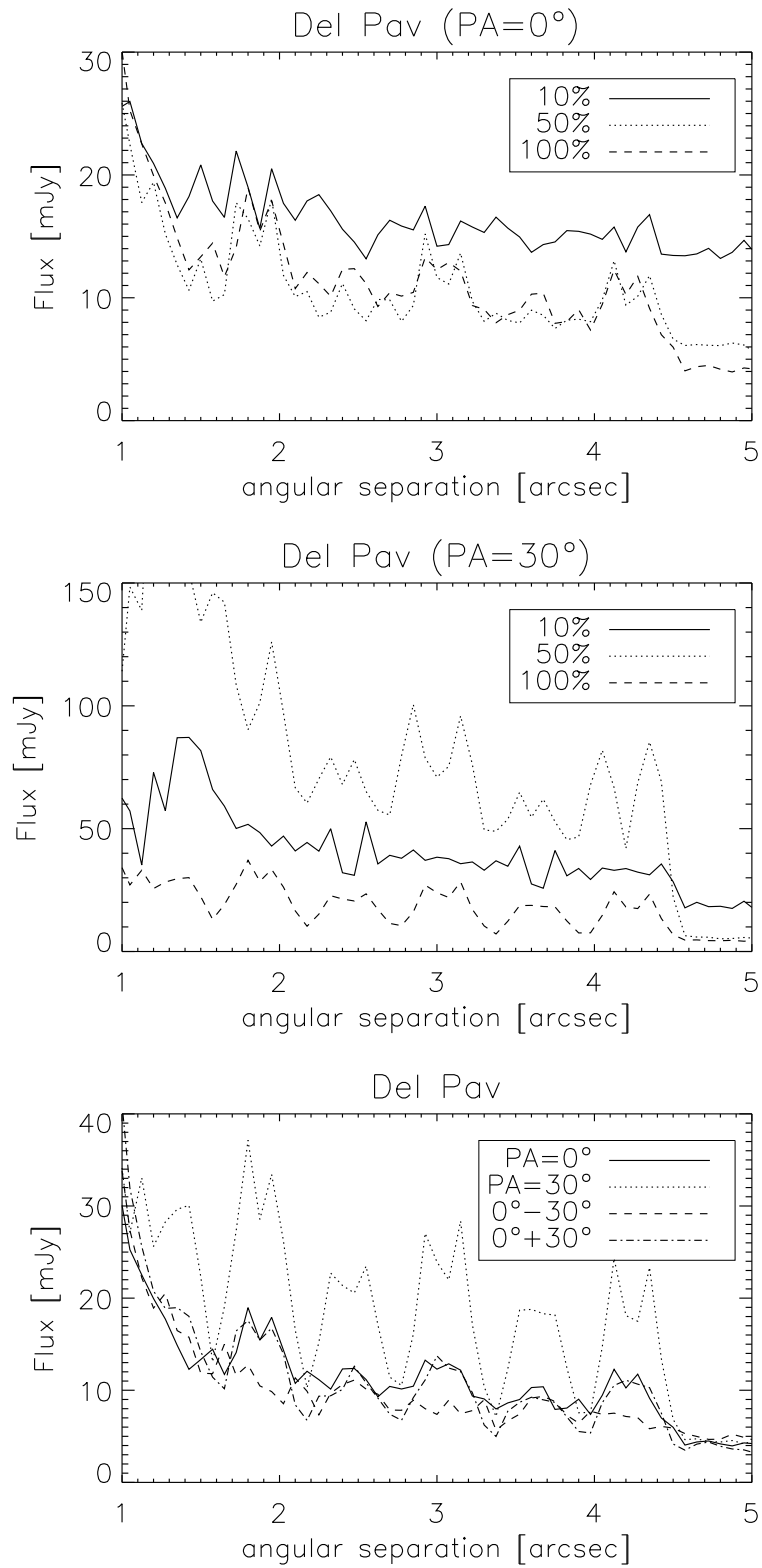
Figure A.8: 5σ sensitivity limit from the observations of Del Pav.

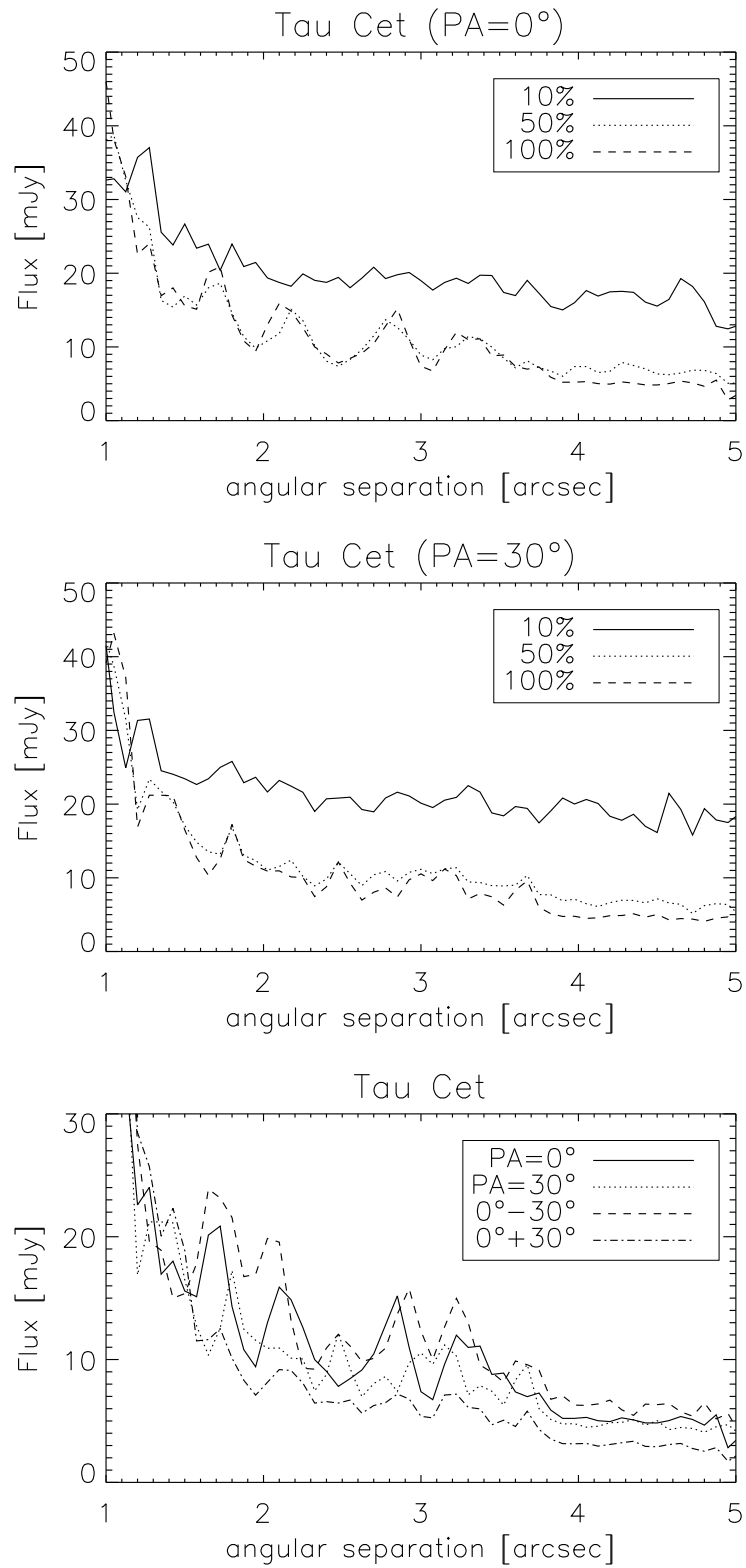
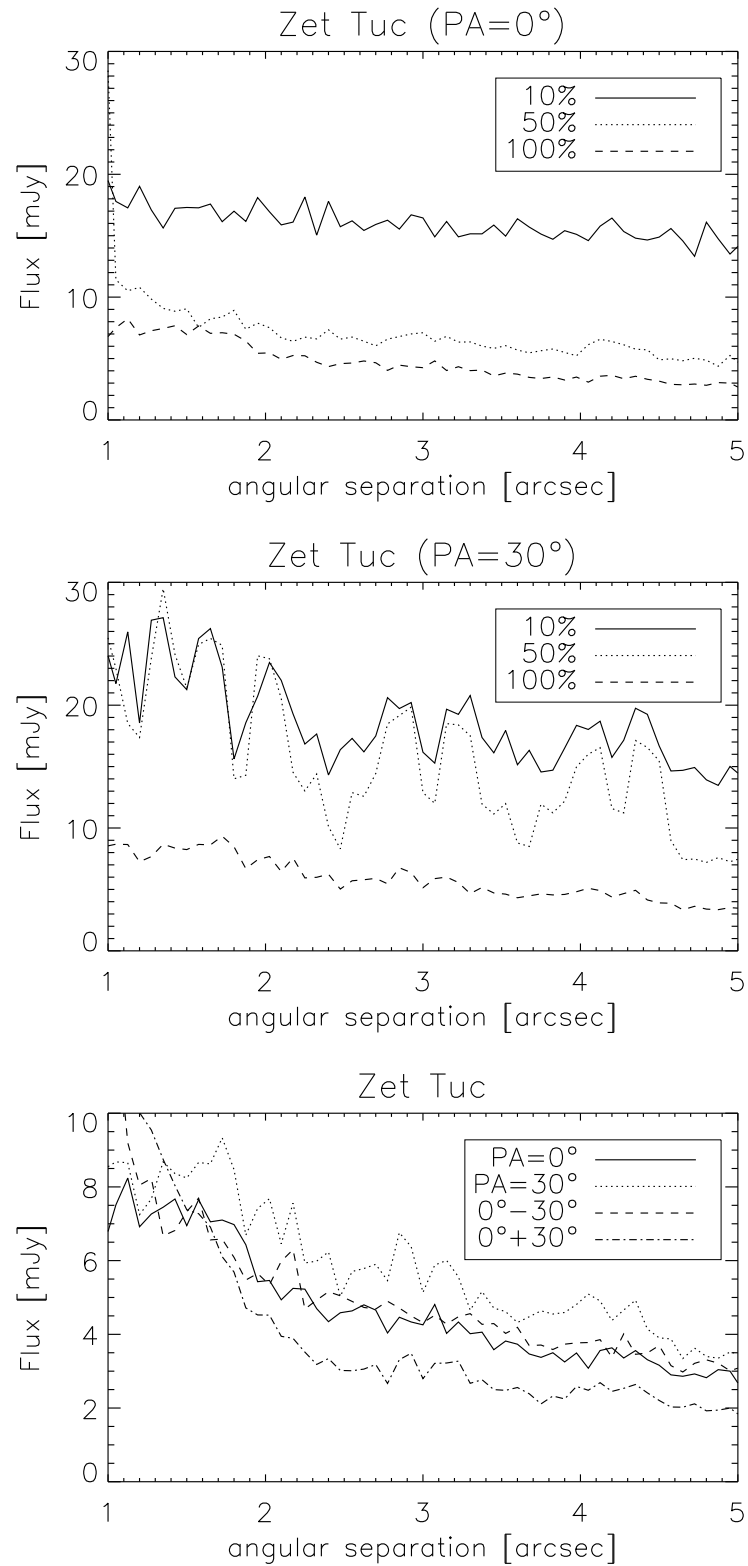
Figure A.9: 5σ sensitivity limit from the observations of τ Cet.

Figure A.10: 5σ sensitivity limit from the observations of ζ Tuc.

Bibliography

- Acke, B. & van den Ancker, M. E. 2004, *A&A*, 426, 151
- Acke, B. & van den Ancker, M. E. 2006, *A&A*, 449, 267
- Allard, F., Hauschildt, P. H., Alexander, D. R., Tamanai, A., & Schweitzer, A. 2001, *ApJ*, 556, 357
- Allard, F., Hauschildt, P. H., Baraffe, I., & Chabrier, G. 1996, *ApJL*, 465, L123+
- Andre, P. & Montmerle, T. 1994, *ApJ*, 420, 837
- Andre, P., Ward-Thompson, D., & Barsony, M. 1993, *ApJ*, 406, 122
- Andrews, S. M. & Williams, J. P. 2005, *ApJ*, 631, 1134
- Apai, D., Pascucci, I., Brandner, W., et al. 2004, *A&A*, 415, 671
- Ardila, D. R., Golimowski, D. A., Krist, J. E., et al. 2007, *ApJ*, 665, 512
- Augereau, J. C., Lagrange, A. M., Mouillet, D., & Ménard, F. 2001, *A&A*, 365, 78
- Bailer-Jones, C. A. L. & Mundt, R. 1999, *A&A*, 348, 800
- Baraffe, I., Chabrier, G., Barman, T. S., Allard, F., & Hauschildt, P. H. 2003, *A&A*, 402, 701
- Barrado y Navascués, D., Mohanty, S., & Jayawardhana, R. 2004, *ApJ*, 604, 284
- Bastien, P. & Menard, F. 1990, *ApJ*, 364, 232
- Beckford, A. F., Lucas, P. W., Chrysostomou, A. C., & Gledhill, T. M. 2008, *MNRAS*, 384, 907
- Benedict, G. F., McArthur, B. E., Gatewood, G., et al. 2006, *AJ*, 132, 2206
- Biller, B. A., Close, L. M., Masciadri, E., et al. 2007, *ApJS*, 173, 143
- Bontemps, S., André, P., Kaas, A. A., et al. 2001, *A&A*, 372, 173
- Bouvier, J. & Appenzeller, I. 1992, *A&AS*, 92, 481
- Bouwman, J., de Koter, A., Dominik, C., & Waters, L. B. F. M. 2003, *A&A*, 401, 577
- Burgasser, A. J., Kirkpatrick, J. D., Brown, M. E., et al. 1999, *ApJL*, 522, L65

- Burrows, A., Hubbard, W. B., Lunine, J. I., & Liebert, J. 2001, *Reviews of Modern Physics*, 73, 719
- Burrows, A., Marley, M., Hubbard, W. B., et al. 1997, *ApJ*, 491, 856
- Burrows, A., Sudarsky, D., & Hubeny, I. 2006, *ApJ*, 640, 1063
- Cardoso, C. V., McCaughrean, M. J., King, R. R., et al. 2008, *ArXiv e-prints*
- Chabrier, G., Baraffe, I., Allard, F., & Hauschildt, P. H. 2005, *ArXiv Astrophysics e-prints*
- Chauvin, G., Lagrange, A.-M., Udry, S., et al. 2006, *A&A*, 456, 1165
- Cieza, L., Padgett, D. L., Stapelfeldt, K. R., et al. 2007, *ApJ*, 667, 308
- Cochran, W. D. & Hatzes, A. P. 1993, in *Astronomical Society of the Pacific Conference Series*, Vol. 36, *Planets Around Pulsars*, ed. J. A. Phillips, S. E. Thorsett, & S. R. Kulkarni, 267–273
- Cohen, M., Walker, R. G., Carter, B., et al. 1999, *AJ*, 117, 1864
- Creech-Eakman, M. J., Orton, G. S., Serabyn, E., & Hayward, T. L. 2004, *ApJL*, 602, L129
- Cumming, A., Marcy, G. W., & Butler, R. P. 1999, *ApJ*, 526, 890
- Cushing, M. C., Rayner, J. T., & Vacca, W. D. 2005, *ApJ*, 623, 1115
- Cushing, M. C., Roellig, T. L., Marley, M. S., et al. 2006, *ApJ*, 648, 614
- Cutri, R. M., Skrutskie, M. F., van Dyk, S., et al. 2003, *2MASS All Sky Catalog of point sources*. (The IRSA 2MASS All-Sky Point Source Catalog, NASA/IPAC Infrared Science Archive. <http://irsa.ipac.caltech.edu/applications/Gator/>)
- Debes, J. H., Weinberger, A. J., & Schneider, G. 2008, *ApJL*, 673, L191
- Delfosse, X., Tinney, C. G., Forveille, T., et al. 1997, *A&A*, 327, L25
- Deller, A. T. & Maddison, S. T. 2005, *ApJ*, 625, 398
- Di Folco, E., Thévenin, F., Kervella, P., et al. 2004, *A&A*, 426, 601
- Doucet, C., Habart, E., Pantin, E., et al. 2007, *A&A*, 470, 625
- Endl, M., Kürster, M., Els, S., et al. 2002, *A&A*, 392, 671
- Enoch, M. L., Brown, M. E., & Burgasser, A. J. 2003, *AJ*, 126, 1006
- Epchtein, N., de Batz, B., Capoani, L., et al. 1997, *The Messenger*, 87, 27
- Fazio, G. G., Hora, J. L., Allen, L. E., et al. 2004, *ApJS*, 154, 10
- Fischer, O., Henning, T., & Yorke, H. W. 1996, *A&A*, 308, 863
- Fuhrmann, K. 2004, *Astronomische Nachrichten*, 325, 3

- Gaidos, E. J. 1998, *PASP*, 110, 1259
- Gaidos, E. J., Henry, G. W., & Henry, S. M. 2000, *AJ*, 120, 1006
- Geißler, K., Kellner, S., Brandner, W., et al. 2007, *A&A*, 461, 665
- Gledhill, T. M. 2005, *MNRAS*, 356, 883
- Goldman, B., Cushing, M. C., Marley, M. S., et al. 2008, *A&A*, 487, 277
- Golimowski, D. A., Burrows, C. J., Kulkarni, S. R., Oppenheimer, B. R., & Brukardt, R. A. 1998, *AJ*, 115, 2579
- Golimowski, D. A., Leggett, S. K., Marley, M. S., et al. 2004, *AJ*, 127, 3516
- Goto, M., Kobayashi, N., Terada, H., et al. 2002, *ApJL*, 567, L59
- Grady, C. A., Polomski, E. F., Henning, T., et al. 2001, *AJ*, 122, 3396
- Grady, C. A., Woodgate, B., Heap, S. R., et al. 2005, *ApJ*, 620, 470
- Greaves, J. S., Holland, W. S., Moriarty-Schieven, G., et al. 1998, *ApJL*, 506, L133
- Greaves, J. S., Holland, W. S., Wyatt, M. C., et al. 2005, *ApJL*, 619, L187
- Guenther, E. W., Neuhäuser, R., Huélamo, N., Brandner, W., & Alves, J. 2001, *A&A*, 365, 514
- Hales, A. S., Gledhill, T. M., Barlow, M. J., & Lowe, K. T. E. 2006, *MNRAS*, 365, 1348
- Hartigan, P., Edwards, S., & Ghandour, L. 1995, *ApJ*, 452, 736
- Hatzes, A. P., Cochran, W. D., McArthur, B., et al. 2000, *ApJL*, 544, L145
- Heinze, A., Hinz, P., Sivanandam, S., Apai, D., & Meyer, M. 2006, in Presented at the Society of Photo-Optical Instrumentation Engineers (SPIE) Conference, Vol. 6272, *Advances in Adaptive Optics II*. Edited by Ellerbroek, Brent L.; Bonaccini Calia, Domenico. Proceedings of the SPIE, Volume 6272, pp. 62723S (2006).
- Henry, T. J., Soderblom, D. R., Donahue, R. A., & Baliunas, S. L. 1996, *AJ*, 111, 439
- Holmberg, J., Nordström, B., & Andersen, J. 2007, *A&A*, 475, 519
- Jayawardhana, R., Fisher, S., Hartmann, L., et al. 1998, *ApJL*, 503, L79+
- Jayawardhana, R., Mohanty, S., & Basri, G. 2003, *ApJ*, 592, 282
- Jura, M. 1991, *ApJL*, 383, L79+
- Kalas, P., Liu, M. C., & Matthews, B. C. 2004, *Science*, 303, 1990
- Kasper, M., Apai, D., Janson, M., & Brandner, W. 2007, *A&A*, 472, 321
- Kirkpatrick, J. D., Reid, I. N., Liebert, J., et al. 1999, *ApJ*, 519, 802

- Koerner, D. W., Ressler, M. E., Werner, M. W., & Backman, D. E. 1998, *ApJL*, 503, L83+
- Kóspál, Á., Ábrahám, P., Apai, D., et al. 2008, *MNRAS*, 383, 1015
- Krist, J. E., Stapelfeldt, K. R., Ménard, F., Padgett, D. L., & Burrows, C. J. 2000, *ApJ*, 538, 793
- Kumar, S. S. 1963, *ApJ*, 137, 1121
- Lachaume, R., Dominik, C., Lanz, T., & Habing, H. J. 1999, *A&A*, 348, 897
- Lada, C. J. 1987, in *IAU Symposium, Vol. 115, Star Forming Regions*, ed. M. Peimbert & J. Jugaku, 1–17
- Lagage, P.-O., Doucet, C., Pantin, E., et al. 2006, *Science*, 314, 621
- Lagage, P. O., Pel, J. W., Authier, M., et al. 2004, *The Messenger*, 117, 12
- Leggett, S. K., Golimowski, D. A., Fan, X., et al. 2002a, *ApJ*, 564, 452
- Leggett, S. K., Hauschildt, P. H., Allard, F., Geballe, T. R., & Baron, E. 2002b, *MNRAS*, 332, 78
- Leggett, S. K., Toomey, D. W., Geballe, T. R., & Brown, R. H. 1999, *ApJL*, 517, L139
- Liebert, J., Young, P. A., Arnett, D., Holberg, J. B., & Williams, K. A. 2005, *ApJL*, 630, L69
- Liu, M. C., Fischer, D. A., Graham, J. R., et al. 2002, *ApJ*, 571, 519
- Liu, M. C. & Leggett, S. K. 2005, *ApJ*, 634, 616
- Liu, W. M., Hinz, P. M., Meyer, M. R., et al. 2003, *ApJL*, 598, L111
- Lowrance, P. J., Schneider, G., Kirkpatrick, J. D., et al. 2000, *ApJ*, 541, 390
- Lucas, P. W. & Roche, P. F. 1998, *MNRAS*, 299, 699
- Luhman, K. L. 2008, *ArXiv e-prints*
- Luhman, K. L., D’Alessio, P., Calvet, N., et al. 2005a, *ApJL*, 620, L51
- Luhman, K. L., Lada, C. J., Hartmann, L., et al. 2005b, *ApJL*, 631, L69
- Luhman, K. L., Patten, B. M., Marengo, M., et al. 2007, *ApJ*, 654, 570
- Malfait, K., Waelkens, C., Waters, L. B. F. M., et al. 1998, *A&A*, 332, L25
- Marengo, M., Megeath, S. T., Fazio, G. G., et al. 2006, *ApJ*, 647, 1437
- Marley, M. S., Saumon, D., Guillot, T., et al. 1996, *Science*, 272, 1919
- Martin, E. L., Basri, G., Delfosse, X., & Forveille, T. 1997, *A&A*, 327, L29
- Martin, E. L., Montmerle, T., Gregorio-Hetem, J., & Casanova, S. 1998, *MNRAS*, 300, 733
- Martin-Zaïdi, C., Lagage, P.-O., Pantin, E., & Habart, E. 2007, *ApJL*, 666, L117

- Masciadri, E., Mundt, R., Henning, T., Alvarez, C., & Barrado y Navascués, D. 2005, *ApJ*, 625, 1004
- Matthews, K., Nakajima, T., Kulkarni, S. R., & Oppenheimer, B. R. 1996, *AJ*, 112, 1678
- McCaughrean, M. J., Close, L. M., Scholz, R.-D., et al. 2004, *A&A*, 413, 1029
- Meeus, G., Waters, L. B. F. M., Bouwman, J., et al. 2001, *A&A*, 365, 476
- Metchev, S. A. & Hillenbrand, L. A. 2004, *ApJ*, 617, 1330
- Mohanty, S., Basri, G., & Jayawardhana, R. 2005, *Astronomische Nachrichten*, 326, 891
- Morales-Calderón, M., Stauffer, J. R., Kirkpatrick, J. D., et al. 2006, *ApJ*, 653, 1454
- Muench, A. A., Alves, J., Lada, C. J., & Lada, E. A. 2001, *ApJL*, 558, L51
- Nakajima, T., Oppenheimer, B. R., Kulkarni, S. R., et al. 1995, *Natur*, 378, 463
- Neuhäuser, R., Mugrauer, M., & Guenther, E. 2006, *The Messenger*, 123, 25
- Noll, K. S., Geballe, T. R., Leggett, S. K., & Marley, M. S. 2000, *ApJL*, 541, L75
- Noll, K. S., Geballe, T. R., & Marley, M. S. 1997, *ApJL*, 489, L87+
- Oppenheimer, B. R., Kulkarni, S. R., Matthews, K., & van Kerkwijk, M. H. 1998, *ApJ*, 502, 932
- Padgett, D. L., Cieza, L., Stapelfeldt, K. R., et al. 2006, *ApJ*, 645, 1283
- Pantin, E., Vanzi, L., & Weilenman, U. 2007, to appear in the proceedings of the ESO Instrument Calibration Workshop 2007
- Pantin, E., Waelkens, C., & Lagage, P. O. 2000, *A&A*, 361, L9
- Patten, B. M., Stauffer, J. R., Burrows, A., et al. 2006, *ApJ*, 651, 502
- Porto de Mello, G. F., Lyra, W., & Keller, G. R. 2008, *A&A*, 488, 653
- Potter, D., Martín, E. L., Cushing, M. C., et al. 2002, *ApJL*, 567, L133
- Rieke, G. H., Su, K. Y. L., Stansberry, J. A., et al. 2005, *ApJ*, 620, 1010
- Rieke, G. H., Young, E. T., Engelbracht, C. W., et al. 2004, *ApJS*, 154, 25
- Roche, P. F. 2004, *Advances in Space Research*, 34, 583
- Roellig, T. L., Houck, J. R., Van Cleve, J. E., et al. 1998, in Presented at the Society of Photo-Optical Instrumentation Engineers (SPIE) Conference, Vol. 3354, Proc. SPIE Vol. 3354, p. 1192-1203, *Infrared Astronomical Instrumentation*, Albert M. Fowler; Ed., ed. A. M. Fowler, 1192–1203
- Roellig, T. L., Van Cleve, J. E., Sloan, G. C., et al. 2004, *ApJS*, 154, 418
- Saffe, C., Gómez, M., & Chavero, C. 2005, *A&A*, 443, 609

- Saumon, D., Geballe, T. R., Leggett, S. K., et al. 2000, *ApJ*, 541, 374
- Saumon, D., Marley, M. S., & Lodders, K. 2003a, *ArXiv Astrophysics e-prints*
- Saumon, D., Marley, M. S., Lodders, K., & Freedman, R. S. 2003b, in *IAU Symposium*, Vol. 211, *Brown Dwarfs*, ed. E. Martín, 345–+
- Schneider, G., Silverstone, M. D., Hines, D. C., et al. 2006, *ApJ*, 650, 414
- Schneider, G., Smith, B. A., Becklin, E. E., et al. 1999, *ApJL*, 513, L127
- Schneider, G., Weinberger, A. J., Becklin, E. E., Debes, J. H., & Smith, B. A. 2009, *AJ*, 137, 53
- Scholz, R.-D., McCaughrean, M. J., Lodieu, N., & Kuhlbrodt, B. 2003, *A&A*, 398, L29
- Siebenmorgen, R., Prusti, T., Natta, A., & Müller, T. G. 2000, *A&A*, 361, 258
- Silverstone, M. D., Meyer, M. R., Mamajek, E. E., et al. 2006, *ApJ*, 639, 1138
- Smith, V. V., Tsuji, T., Hinkle, K. H., et al. 2003, *ApJL*, 599, L107
- Song, I., Caillault, J.-P., Barrado y Navascués, D., Stauffer, J. R., & Randich, S. 2000, *ApJL*, 533, L41
- Stauffer, J. R., Hartmann, L. W., & Barrado y Navascues, D. 1995, *ApJ*, 454, 910
- Sterzik, M. F., Pantin, E., Hartung, M., et al. 2005, *A&A*, 436, L39
- Stoughton, C., Lupton, R. H., Bernardi, M., et al. 2002, *AJ*, 123, 485
- Strom, K. M., Strom, S. E., Edwards, S., Cabrit, S., & Skrutskie, M. F. 1989, *AJ*, 97, 1451
- Tarter, J. & Silk, J. 1974, *QJRAS*, 15, 122
- Telesco, C. M., Fisher, R. S., Piña, R. K., et al. 2000, *ApJ*, 530, 329
- Valenti, J. A. & Fischer, D. A. 2005, *ApJS*, 159, 141
- van Boekel, R., Min, M., Waters, L. B. F. M., et al. 2005, *A&A*, 437, 189
- van Buren, D., Brundage, M., Ressler, M., & Terebey, S. 1998, *AJ*, 116, 1992
- van den Ancker, M. E., de Winter, D., & Tjin A Djie, H. R. E. 1998, *A&A*, 330, 145
- Van Kerckhoven, C., Tielens, A. G. G. M., & Waelkens, C. 2002, *A&A*, 384, 568
- van Leeuwen, F. 2007, *A&A*, 474, 653
- Volk, K., Blum, R., Walker, G., & Puxley, P. 2003, *IAU Circ.*, 8188, 2
- Walker, G. A. H., Walker, A. R., Irwin, A. W., et al. 1995, *Icarus*, 116, 359
- Werner, M. W., Roellig, T. L., Low, F. J., et al. 2004, *ApJS*, 154, 1
- Whelan, E. T., Ray, T. P., Bacciotti, F., et al. 2005, *Natur*, 435, 652

- Whitney, B. A. & Hartmann, L. 1993, *ApJ*, 402, 605
- Whitney, B. A., Kenyon, S. J., & Gomez, M. 1997, *ApJ*, 485, 703
- Whittet, D. C. B., Prusti, T., Franco, G. A. P., et al. 1997, *A&A*, 327, 1194
- Wilking, B., Gagne, M., & Allen, L. 2008, ArXiv e-prints
- Wilking, B. A., Meyer, M. R., Robinson, J. G., & Greene, T. P. 2005, *AJ*, 130, 1733
- Wolf, S., Henning, T., & Stecklum, B. 2003, in Presented at the Society of Photo-Optical Instrumentation Engineers (SPIE) Conference, Vol. 4843, Society of Photo-Optical Instrumentation Engineers (SPIE) Conference Series, ed. S. Fineschi, 524–532
- Wright, J. T., Marcy, G. W., Butler, R. P., & Vogt, S. S. 2004, *ApJS*, 152, 261
- Zuckerman, B., Song, I., Bessell, M. S., & Webb, R. A. 2001, *ApJL*, 562, L87

Acknowledgments

I want to thank Prof. Dr Thomas Henning, Dr. Wolfgang Brandner and Dr. Michael F. Sterzik for the opportunity to conduct my PhD thesis under their supervision at the Max-Planck-Institute for Astronomy in Heidelberg and at ESO Vitacura in Santiago de Chile. I am grateful for their advice, time and patience.

To my family for their support during those three years, for always encouraging me to do what i want and for not asking to many questions about my work.

To my friends at ESO, here in Heidelberg and where ever they may be living now. Special thanks to those who are no astronomers for talking with me about 'normal' stuff.